

**Mountain Scale Strength Properties,
Deep-Seated Landsliding, and Relief Limits**

BY

Kevin Michael Schmidt



December 9, 1994

Mountain Scale Strength Properties,
Deep-Seated Landsliding, and Relief Limits

by

Kevin Michael Schmidt


A thesis submitted in partial fulfillment
of the requirements for the degree of

Master of Science

University of Washington

1994

Approved by


(Chairperson of Supervisory Committee)


Thomas Dunna

Program Authorized
to Offer Degree Department of Geological Sciences

Date December 9, 1994

In presenting this thesis in **partial** fulfillment of the requirements for a Master's degree at the University of Washington, I agree that the Library shall make its copies freely available for inspection. I further agree that extensive copying of this thesis is allowable only for scholarly purposes, consistent with "fair use" as prescribed in the U.S. Copyright Law. Any other reproduction for any purposes or by any means shall not be allowed without my written permission.

Signature Kevin M. Schmidt

Date Dec 12, 1994

TABLE OF CONTENTS

	<i>Page</i>
LIST OF FIGURES..	v
LIST OF TABLES	xi
LIST OF SYMBOLS..	xii
CHAPTER 1. MOTIVATION, BACKGROUND, AND OBJECTIVES	1
Statement of Purpose..	1
Intact Rock Strength and the Importance of Discontinuities..	2
Relief Limits..	3
Historic Deep-Seated Landslides..	6
Objectives and Methods of Study..	8
Study Areas	9
CHAPTER 2. STABILITY ANALYSIS: THEORY AND BACK- CALCULATED STRENGTH PARAMETERS	18
Rankine Stress State..	19
Planar Failure Surface..	20
Culmann Model..	21
Previous Studies of Slope/Height Relationships..	22
Hoek and Bray Plane Failure Model..	24
Regional Strength Parameters..	26
Stability Analysis Including Seismic Accelerations..	28
CHAPTER 3. BACK-CALCULATED MATERIAL PROPERTIES..	35
Northwest Cascades Study Area..	35
Quaternary Glacial Sediments..	37
Material Description..	37
Failure Character and Location..	38
Method of Analysis..	38
Back-Calculated Strength Properties..	39

Predicted Tension Depth and Observed Maximum Height of Vertical Channel Bank..	41
Channel Bank Incision and Evolution..	41
Effect of Timber Harvesting..	41
Chuckanut Formation..	42
Material Description..	42
Failure Character and Location..	43
Method of Analysis	45
Back-Calculated Strength Properties..	45
Buttressing from Glacial Deposits	46
Darrington Phyllite..	47
Material Description..	47
Failure Character and Location..	47
Method of Analysis..	48
Relief Development..	48
Effect of Weathering..	48
Santa Cruz Mountains Study Area..	49
Material Description	49
Failure Character and Location..	49
Method of Analysis	50
Back-Calculated Strength Properties	51
Back-Calculated and Laboratory-Derived Strength Properties..	52
CHAPTER 4. ROCK MASS STRENGTH ASSESSMENT..	74
Previous Studies..	74
Discontinuities and their Influence on Rock Mass Strength..	75
Selby's RMS Scheme and Modifications for Application to Deep-Seated Landsliding..	75
Application to Chuckanut Formation..	78
Importance of Discontinuity and Hillslope Orientation..	80
Landscape Profiles, RMS, and Geologic Structure..	81
Conclusion..	82

CHAPTER 5. EARTHQUAKES AND THE LIMIT TO TOPOGRAPHIC DEVELOPMENT..	9 4
Horizontal and Vertical Accelerations in Modified Culmann Model.....	9 4
Application to Santa Cruz Mountains Study Area..	9 6
Application to Pacific Northwest Study Area..	9 8
Glacial Deposits..	9 9
Chuckanut Formation..	100
Conclusion..	101
 CHAPTER 6. SPATIAL AND TEMPORAL CONTROLS ON ROCK MASS STRENGTH AND LANDSCAPE DEVELOPMENT	110
Spatial Influence..	110
Sample Size..	110
Geologic Structure..	112
Temporal Influence..	113
Stress Rate..	113
Weathering..	114
Earthquakes..	115
Glacial Buttresses..	117
Landscape Evolution..	117
 CHAPTER 7. SUMMARY..	126
Landscape Evolution and Material Properties..	126
Back-Calculated Material Properties..	127
Glacial Sediments..	127
Chuckanut Formation..	127
Darrington Phyllite..	127
Santa Cruz Mountains Sedimentary Units..	128
Back-Calculated vs. Laboratory Derived Parameters..	128
Spatial Influence	128
Temporal Influence..	129
Rock Mass Strength..	129
Earthquake-Induced Strong Ground Motions..	130

REFERENCES	132
APPENDIX A. Rankine Theory and Depth of Tension in a Vertical Face.....	146
APPENDIX B. Culmann Model	149
APPENDIX C. Hoek and Bray Model	155
APPENDIX D. Modified Culmann Model Including Horizontal Seismic Accelerations	158
APPENDIX E. Modified Culmann Model Including Vertical Seismic Accelerations .	163

LIST OF FIGURES

Number		<i>Page</i>
1-1	Rock Strength and Relief in a Threshold Landscape .	12
1-2	Landscape Dissection with Isostatic Compensation	13
1-3	Slope/Relief Distribution of Major Mountain Ranges .	14
1-4	Site Map of Pacific Northwest Study Area	15
1-5	Site Map of Santa Cruz Mountains, CA Study Area .	16
2-1	Mohr Stress Circle .	29
2-2	Stress State in Vertical Face Predicted by Rankine Theory.....	30
2-3	Wedge-Shaped Landslide and Corresponding Hillslope Stress State Considered in Culmann Model	31
2-4	Graphical Representation of Hoek and Bray Model Input Parameters	32
2-5	Landscape Attaining Relief Limit with Deep-Seated Landsliding	33
2-6	Limit to Topographic Development with Respect to Slope and Relief	34
3-1	Schematic Cross-Section of Inner-Gorge and Mountain-Front Landslides	54

3-2	Site Map of Landslides in Portion of Field Area	5 5
3-3	Active Inner-Gorge Glacial Deposit Landslides	5 6
3-4	Exposed Channel Bank along Middle Fork of Nooksack River	5 7
3-5	Back-Rotated Slump in Glacial Deposits along Clearwater Creek	5 8
3-6	Topographic Development of Glacial Deposits a. Slope/Relief Distribution b. Base Length/Relief Distribution	5 9
3-7	Spatial Distribution of Hillslope Processes in Glacial Sediments with Respect to Slope and Relief	6 0
3-8	Map of landslides within Chuckanut Formation	6 1
3-9	Frontal View of Deep-Seated Rockslide in Chuckanut Formation	6 2
3-10	Lateral View of Deep-Seated Rockslides in Chuckanut Formation	6 3
3-11	Slope/Relief Distribution of all Chuckanut Formation Transects	6 4
3-12	Slope/Relief Distribution of the Chuckanut Formation a. Anti-Dip Slope Transects b. Dip Slope Transects	6 5

3-13	Base Length/Relief Distribution of the Chuckanut Formation a. Anti-Dip Slope Transects b. Dip Slope Transects	6.6
3-14	Inner-Gorge Landslide within Darrington Phyllite 67
3-15	Topographic Development of Darrington Phyllite a. Slope/Relief Distribution b. Base Length/Relief Distribution	68
3-16	Rockslide in the Santa Cruz Mountains Initiated during the Loma Prieta Earthquake	69
3-17	Topographic Development of Marine Sediments Comprising the Santa Cruz Mountains a. Slope/Relief Distribution b. Base Length/Relief Distribution	70
3-18	Graphical Representation of Coulomb Equation for Back-Calculated Material Strength Properties	71
4-1	a. Schematic of Uniaxial Stress State and Relation between Hillslope Gradient and Bedding Plane Dip b. Mohr Diagram for Uniaxial Stress State	83
4-2	Bedding RMS Values for Stable and Landslide Sites in the Chuckanut Formation with Respect to Slope and Relief	84
4-3	Bedding RMS Values in the Chuckanut Formation a. RMS vs. Relief b. RMS vs. Slope	85

4-4	Jointing RMS Values in the Chuckanut Formation	
	a. RMS vs. Relief	
	b. RMS vs. Slope	86
4-5	Frequency of Sites with Respect to Angular Divergence Between Bedding and Hillslope Orientation	
	a. Stable Sites	
	b. Landslide Sites	87
4-6	Frequency of Sites with Respect to Angular Divergence Between Primary Joint Set and Hillslope Orientation	
	a. Stable Sites	
	b. Landslide Sites	88
4-7	Distribution of Strike and Apparent Dip Divergence	
	a. Bedding Planes	
	b. Joint Sets	89
4-8	a, b, & c. Topographic Profiles expressed by Chuckanut Formation	90
5-1	Force Balance During Seismic Conditions Assuming a Horizontal Equivalent Static Force	103
5-2	Force Balance During Seismic Conditions Assuming a Downward Vertical Equivalent Static Force	104
5-3	Force Balance During Seismic Conditions Assuming an Upward Vertical Equivalent Static Force	105

5-4	LTD for Santa Cruz Mountains a. Horizontal Seismic Accelerations Assuming Aseismic Failure Surface Generation b. Downward Vertical Seismic Accelerations	106
5-5	LTD for Santa Cruz Mountains under Horizontal Seismic Accelerations Assuming Coseismic Failure Surface Generation	107
5-6	LTD for Glacial Deposits under Horizontal Seismic Accelerations	108
5-7	LTD for Chuckanut Formation under Horizontal Seismic Accelerations a. Anti-dip Slopes b. Dip Slopes	109
6-1	Spatial Distribution of Discontinuities	121
6-2	Rock Mass Strength Frequency Distribution	122
6-3	Topographic Development as a Function of Time	123
6-4	Topographic Development as a Function of Time a. LTD Greater Than Actual Topographic Development b. LTD Coinciding with Actual Topographic Development	124

6-5	Topographic Development as a Function of Tie	
	a. LTD for Two Different Weathering Regimes	
	b. LTD for Two Different Tectonic Regimes	125
App-1	Graphical Representation of Culmann Model	
	Input P a r a m e t e r s	154

LIST OF TABLES

Number		<i>Page</i>
1-1	Topographic Properties of 24 Major Mountain Ranges of the World.....	17
3-1	Strength Properties for Consolidated Materials Obtained through Back-Calculation, Field Measurements, and Laboratory Experiments	72
3-2	Strength Properties for Unconsolidated Materials Obtained through Back-Calculation, Field Measurements, and Laboratory Experiments.....	73
4-1	Rock Mass Strength Parameters and Rating D e s c r i p t i o n s	91
4-2	Intact Rock Strength Assessment	92
4-3	Discontinuity Orientation Assessment	93

LIST OF SYMBOLS

A	strip of unit width on failure surface over which cohesion acts
α	failure surface angle measured with respect to horizontal
a_{lim}	limiting logarithmic slope
β	hillslope angle measured with respect to horizontal or major principal plane
c	cohesion
c_d	developed cohesion
E	Young's modulus
F	factor of safety
F_e	force related to seismic acceleration
F_r	resultant force
ϕ	internal friction angle
g	gravitational acceleration
γ	unit weight of earth material
γ_w	unit weight of water
H	height, or local relief, of hillslope
H_c	critical stable relief of hillslope

H_{lim}	maximum possible relief of landscape
K	seismic coefficient, expressed as a fraction of the gravitational acceleration
l	hillslope length
L_{lim}	base length of hillslope associated with maximum possible relief (H_{lim})
p	thickness of failure block
ρ	density of earth material
q_u	unconfined compressive strength of rock
RMS	rock mass strength
R	rock mass strength parameter rating
S	shear strength of earth material
σ	normal stress
τ	shear stress
U	uplift force due to water pressure on the failure surface
V	cleft pressure, uplift force due to water pressure in tension crack
W	weight of failure block
Z	vertical depth from ground surface
Z_w	depth of water in tension crack

Z_c maximum depth of tension predicted by Rankine Theory

ACKNOWLEDGMENTS

Special thanks are extended to my advisors, David Montgomery and Thomas Dunne. Tom gently nudged me in the direction of the “big picture” and taught me about “ching-ching” rock. Dave ably guided me through the many obstacles of graduate research and provided an enthusiastic sounding board for ideas.

Yann Merrand, Victoria Langenheim, Jonathan Stock, and Matthew Coglou provided the **field** assistance necessary to work efficiently in the lush forests of western Washington state.

Special thanks go to Peter Reiners, Juliet Crider, John **Buffington**, and Victoria Langenheim for mental support and general guidance through life.

Support for this study was provided by grants from Washington State Timber, Fish, and Wildlife (TFW) **FY92-010** and **FY94-004** in addition to a gift from the Washington Forest Protection Association (**WFPA**).

“Observation, not old age, brings wisdom.”

- Plubilius Sententiae

CHAPTER 1. MOTIVATION, BACKGROUND, AND OBJECTIVES

STATEMENT OF PURPOSE

Controls on the size of mountains and the stability of bedrock slopes are only poorly constrained, but provide potentially important limits to the development of topographic relief, where relief is defined as the elevation difference between the highest and lowest points in a predetermined reference area. Although no theory exists for predicting the limit to topographic development of a mountain or hillslope, regions of considerable relief and steep gradients, such as active tectonic areas with rapidly uplifting mountain ranges, typically display widespread landsliding. (The term “topographic development” here refers to the relief and gradient of a hillslope.) The maximum topographic development attainable is controlled by erosional processes, uplift rates, base level changes, and material strength over long time scales. I hypothesize that in the absence of transient stresses caused by earthquakes, as valleys deepen and steepen through erosion, gravitational stresses within hillslopes increase until shear stresses (τ) surpass shear resistances (S) and slope failure occurs. This hypothesis implies that there is a limit to topographic development where the full material strength is engaged and the material composing a hillslope is no longer capable **of supporting** further increases in relief (Figure 1- 1). Additionally, transient stresses arising from earthquake-induced strong ground motions may prematurely destabilize those hillslopes approaching their maximum attainable relief and gradient defined by rock strength. In this manner, deep-seated, bedrock landsliding provides a feedback mechanism for limiting topographic development.

Slope stability is generally a function of local relief, gradient, degree of saturation, and material strength. Natural slopes, however, rarely express relief close to the maximum stable cliff height predicted by intact rock strengths. This discrepancy may arise because incision of natural landscapes is limited by the boundary conditions of base level and mountain range size, which may constrain relief to the “erosion limited” field of Figure 1 * 1. Alternatively, threshold strength values attributable to a landscape may be lower than those obtained through classic laboratory experiments and small-scale field tests. I believe the

presence of widespread bedrock landsliding in landscapes with relief below that predicted for instability supports the latter explanation. Pervasive material discontinuities such as faults, joints, and bedding planes dramatically decrease the relative strength of a rock mass. Cohesive bonds within intact rock are quite strong, but across a discontinuity the cohesive strength is reduced to zero. In addition, the present topographic expression of a landscape reflects the history of slope formation, including weathering and all extreme events such as elevated pore pressures and earthquake-induced strong ground motions. For example, cumulative piecemeal degradation of rock strength over long time scales may drive an erosion limited landscape to a strength limited one where maximum relief is limited by the material strength. (Figure 1-1). The boundary, though, between the erosion limited and strength limited fields is **not** a finite threshold. Rather, the factors of material property spatial heterogeneity and failure probability dictate a transitional zone between the two fields. While laboratory analysis can provide strength properties for intact rock centimeters in size, determining representative strength properties of a mountain or hillslope is difficult because such properties integrate both material and structural discontinuities, and may also be time dependent.

I hypothesize that such integrated rock strength properties limit topographic development and effectively bound the size of stable hillslopes for mountain drainage basins in a given lithologic, climatic, and tectonic regime. This hypothesis is investigated using theory and field examples in the northern Cascades of Washington state and in the Santa Cruz Mountains of California. *In situ*, large-scale strength properties are **back-**calculated from observed topography. In addition, the influence of rock mass discontinuities and seismic accelerations on landslide susceptibility and topographic development are investigated.

INTACT ROCK STRENGTH AND THE IMPORTANCE OF DISCONTINUITIES

There are often large discrepancies between rock strength measured in the laboratory and representative field properties. The term rock strength is here used to describe the ability of material to resist deformation by tensile, shear, or compressive stresses. Intact rock possesses great unconfined compressive strength due to cohesion associated with crystalline bonds. Material discontinuities, however, may dominate rock strength. Laboratory-derived properties of intact rock, for example, greatly overestimate

the predicted maximum stable cliff height. Teaaghi (1962) describes the critical height of a vertical slope in unweathered mechanically intact rock as:

$$H_c = \frac{q_u}{\gamma} \quad (1-1)$$

where H_c is the maximum stable relief, q_u is the unconfined compressive strength, and γ is the unit weight of rock. In equation 1-1 the unconfined compressive strength, as a stress, is simply the weight of rock per unit area of the base ($H_c \gamma$). Using average values for intact sandstone from Selby (1982), $q_u = 100 \text{ MN/m}^2$ and $\gamma = 20 \text{ kN/m}^3$, equation 1-1 predicts a monumental vertical slope height of 5,000 m. Furthermore, these strength values represent comparatively weak rock; harder rocks such as granite could theoretically stand at much greater heights. In natural landscapes vertical cliffs do not develop such relief and hillslopes of smaller heights and shallower gradients produce landslides because rock strength is substantially weakened by mechanical defects.

The size, spacing, pervasiveness, and orientation of discontinuities within a **hillslope** control hillslope-scale rock strength. As the density of discontinuities within a rock mass increases, rock strength decreases. In addition, the texture and structure of discontinuity surfaces alters strength. Discontinuity orientation with respect to topography also must be considered. These and other considerations are discussed in greater detail in Chapter 4. The combined influences of discontinuities decreases bulk rock strength and substantially lowers the limiting stable relief.

RELIEF LIMITS

The principal source of energy for gravitational stresses within a hillslope stems from surface uplift and subsequent incision of a landscape. As relief builds, the shear stress on a potential failure surface increases as more weight is progressively acting on the potential failure surface. Slope-forming materials are transported downslope under the influence of gravity, but do not exhibit continuous flow behavior similar to water because earth materials possess a finite shear strength. Downslope transport is exaggerated when either external or internal changes occur. Undercutting by channel incision or glacial scour are external alterations which increase relief and possibly the overall slope gradient as well,

enhancing the gravity-induced shear stress within a rock mass without affecting the shear resistance. Seismic accelerations also temporarily increase the **downslope** component of weight acting on a potential shear surface. Internal changes, in contrast, alter the shearing resistance of the materials without affecting the shear stress. That is, declining shear strength over time due to weathering or shear softening will lower the shear resistance but not the shear stress.

England and Molnar (1990) distinguish surface uplift, uplift of rocks, and exhumation. They define “surface uplift” as the displacement of the Earth’s surface with respect to the geoid, “uplift of rocks” as the displacement of rocks with respect to the geoid, and “exhumation” or erosion as the displacement of rocks with respect to Earth’s surface. The three displacements are related by:

$$\text{surface uplift} = \text{uplift of rock} - \text{exhumation} \quad (1-2)$$

In addition, England and Molnar discuss the isostatic balance between exhumation and uplift of rocks. As exhumation reduces **crustal** thickness, the surface moves downward with respect to the geoid, while rocks remaining on or below the surface move upward with respect to the geoid. Molnar and England (1990) discuss how incision of a landscape increases relief and may lead to higher peak elevations, but a lower mean elevation through isostatic compensation (Figure 1-2). There is a limit, however, to relief development provided by deep-seated landsliding that depends on the magnitude of mountain-scale shear strength.

In the previous example using equation 1-1, stronger rocks are capable of producing greater relief, but how is “strong” accurately quantified for rock masses over great spatial and temporal scales? Rahn (1971) presented a qualitative approach to this problem in his discussion of a correlation between the relative weathering of tombstones and their relation to topography. Based on the observation that tombstone lithologies with the smallest degree of weathering correlated with highest average elevations, **Rahn** concluded that topography of New England is the result of differential weathering. The strongest rock, granite, exhibited the highest average elevation and the greatest relief development.

Ahnert (1984) reviews the factors controlling local relief limits of mountain ranges. He concludes that a landscape is the morphological expression of the dynamic equilibrium between **maximum geophysically** possible rates of long-term uplift and the denudational response. Table 1-1 lists the location and geometric properties of relief and base length for 24 mountain ranges. Ahnert estimated that maximum possible relief above the foreland (H_{lim}) is related to the horizontal distance or base length from hillslope crest to the foreland (L_{lim}) such that:

$$a_{lim} = \frac{\log H_{lim}}{\log L_{lim}} \quad (1-3)$$

where a_{lim} , the limiting logarithmic slope lies between 0.775 and 0.8. The ratio of equation 1-3 is nearly a constant, indicating that regions with great relief are broad. Alternatively, narrow mountain ranges have less relief than wider ones. Furthermore, Ahnert suggests that the limiting value implies that the interaction of uplift, material properties, and denudation has a tendency toward establishing a dynamic equilibrium between the uplift rate and the denudation rate.

Examining the relationship between relief and slope. for the mountains listed in Table 1-1, reveals a stratification with respect to relative tectonic activity. Figure 1-3 demonstrates that those localities with the highest rates of uplift (i.e., the Himalayas, Andes, and Alaska) are concentrated together at the highest observed relief development. Similarly, the tectonically quiescent regions of the Black Forest, Wales, Pennines, and the Harz Mtns. represent landscapes of relatively low relief. Regions of moderate tectonic activity such as the Alps, Rocky Mtns., and the Sierra Nevada subsequently plot between these extremes. In addition, locations with the highest slope for a given relief (Mt. Whitney, **Ruwenzori**, and Mt. St. **Elias**) are all composed of hard, coherent rock such as granite, migmatite, or other high grade metamorphic rocks. The east face of the **block-faulted** granitic batholith of the Sierra Nevada at Mt. Whitney plots with the steepest slope. It should be noted that the mountain ranges of Figure 1-3 with the highest reliefs and slopes also coincide with the highest incidence of landsliding (Voight and Pariseau, 1978).

HISTORIC DEEP-SEATED LANDSLIDES

Dismantling of mountain ranges by large, deep-seated landslides is evident in high relief landscapes where landslides increase the degree of landscape dissection, transport large volumes of rock into valley floors, and locally decrease the hillslope gradient. Areas of widespread deep-seated landsliding occur in tectonically and seismically active mountain ranges at the boundaries of major **crustal** plates, particularly around the rim of the Pacific Ocean and along the Alpine and Himalayan chains.

Voight and Pariseau (1978) state that, "...**the** larger the mass movement (usually) the further back in time the event occurred and consequently the more descriptive and less quantitative is our knowledge of the specifics of the event." Modern analogs to large, mountain-scale landslides, however, do exist: Turtle **Mtn**, Frank Alberta, Canada (1903), Gros **Ventre**, Wyoming, (1925); Vaiont, Italy (1963); and Hope, British Columbia, Canada (1965). All these examples occurred in mountainous, high-relief terrain of the circum-Pacific Cordilleran ranges. They are largely the result of active tectonics producing great belts of well-jointed, folded and faulted sedimentary and crystalline rocks exposed on walls of deep valleys. Factors contributing to instability include bedding planes, joints, seismic accelerations, groundwater pressure fluctuations, erosional undercutting, and long-term weathering. In particular, seismic accelerations have been thought to be the trigger of numerous landslides. For example, the Prince William Sound earthquake of 1964 produced 2036 landslides with 5 1 rock avalanche deposits greater than 0.5 km² (McSaveney, 1978).

The 1903 rockslide that destroyed the mining town of Frank in Alberta, Canada, claimed 70 lives, as 36.5 million m³ of limestone flowed 4 km across an alluvial valley (Cruden and Krahn, 1978). The rockslide originated on Turtle Mtn. and may have been initiated in response to mining of a coal seam in the shales below Turtle Mtn. It is believed that failure occurred on the eastern flank of an anticline where the slip surface **first** followed joints perpendicular to bedding, then **paralleled** a bedding plane, and finally traveled along a minor thrust fault to daylight at the ground surface. Approximate relief is 1,000 m with a ground surface sloping at 50°.

The largest (40 million m^3) deep-seated rockslide on historical record in the United States occurred at Gros Ventre, Wyoming, in 1925 (Voight, 1978). Loss of life and property was minimal because, of the sparse population in the area. Although conditions leading to failure were complex, some of the factors include: a highly leached and weathered rock mass; heavy precipitation and warm weather inducing **snowmelt** preceding the event; location within a seismically active zone with an earthquake of magnitude no greater than 3.5 occurring the night before the slide: 640 m of relief, carved approximately parallel to the strike of the beds dipping valley-ward at about **20°**; and an eroded toe

The Vaiont rockslide, located in the Dolomite Region of the Italian Alps, failed catastrophically in 1963 **sending** 270 million m^3 of limestone into a two-thuds full reservoir. The resulting flood destroyed six villages claiming 2,043 lives and has been considered to be one of the greatest flooding disasters in history (**Hendron** and Patton, 1985). No direct witness of the event survived. Despite the fact that this rockslide was being continuously monitored, nobody had predicted the impending cataclysm. Triggered by a combination of precipitation infiltration and rising reservoir levels, the slide mass moved at velocities of 25 m/s. In the upper sections, the hillslope surface and bedding were parallel and in the valley floor, a deep gorge had eroded through stratification. The area has an approximate relief of 900 m with an average slope of 17° (**Müller**, 1964).

The Hope rockslides of British Columbia, Canada, occurring in 1965, resulted in four deaths with no surviving eyewitnesses. The association of seismic and landslide activity in both time and space suggest a seismic triggering mechanism (**Matthews** and **McTaggart**, 1978). Located adjacent to a prehistoric slide, strength was apparently ‘weakened by schistosity aligned parallel to the hillslope surface in the greenstone bedrock.

Other notable historic examples include the 1974 Mayunmarca rockslide and debris flow in the Peruvian Andes. The initial failure occurred as a bedding-plane controlled landslide but transformed into a debris flow traveling at an estimated 130 **km/hr** claiming 45 1 lives (Kojan and Hutchinson, 1978). Similar historic sites in the western United States include: the Madison Canyon rockslide, Montana, the Bonneville landslide of the Columbia River gorge on the Washington-Oregon border, and Little Tahoma Peak rockfalls on Mount Rainier, Washington. Prehistoric analogies span from the Blackhawk landslide in California to the Dakota Group rockslides in the northern Front Range of Colorado.

The most recent example of a large rock failure initiating in a high relief landscape is the rock avalanche emanating from Mt. Cook, New Zealand. On 14 December 1991 a rock and ice avalanche occurred with no obvious external triggering mechanism on the East Face of Mt. Cook, the highest mountain in New Zealand, traveling about 7 km laterally with a vertical fall of 2720 m (Hancox et al., 1991). It is believed that Mt. Cook's morphology has been shaped by this type of process over many hundreds of thousands of years during and since Pleistocene **glaciations**. The rocks in this portion of the Southern New Zealand Alps are composed of Mesozoic indurated, and interbedded greywacke and **argillite** that has been intensely faulted, sheared, and complexly folded. The volume of rock included in the initial avalanche is estimated to be 3 million m³, with a total volume of avalanche debris estimated to be 10 to 15 million m³. The rock failure area, high on the mountain face, is situated such that 10 to 20 m of the summit elevation may have been removed in the event (Hancox et al., 1991). This event provides an example of the active limits to topographic development in a tectonically active mountain range.

OBJECTIVES AND METHODS OF STUDY

This study had three primary objectives: 1) to examine the influence of material properties (cohesion, friction angle, and unit weight) over large spatial scales on landscape form (relief and gradient) and susceptibility to deep-seated landsliding; 2) to characterize rock mass strength at the outcrop scale and its relation to deep-seated landsliding; and 3) to develop a simple model to predict the role of seismic accelerations on slope stability and topographic development.

The approach assumed here uses observed relief and gradient of topography to back-calculate material properties over the scale of a formation for different lithologies, given a relatively uniform climate. This objective required identification of landslide sites within a landscape and characterization of topography. Landslide sites were identified through stereoscopic analysis of aerial photographs while land surface characteristics related to topographic development were obtained from topographic maps and field surveys. Methods used to characterize **the** varying degrees of topographic development for individual lithologies are discussed in Chapter 3.

Rock mass strengths were measured in the field using a modified version of Selby's (1980) classification scheme (Chapter 4). The study of 61 hillslopes, including 17 landslides, in northwestern Washington investigates the relative importance of discontinuities on slope form development and landslide susceptibility. Strength estimates were obtained with respect to bedding planes and joints for hillslopes identified as stable or landslide sites. Parameters were measured primarily on roadcuts with the aid of a metric tape, rock pick, and transit compass.

Chapter 5 examines the influence of earthquakes on slope stability and topographic limits with a simple two-dimensional, limit-equilibrium slope stability model modified to include seismic accelerations. In this simple form, seismic accelerations are considered as equivalent static forces. The model was applied to landslides initiated during the 17 October 1989 **Loma Prieta** earthquake in central California.

Landscape evolution and the two leading categorical influences on material strength, space and time, are discussed in Chapter 6.

STUDY AREAS

The primary field area extends along the United States-Canada border from the San Juan Islands (longitude 123°) to the western flank of Mt. Baker (longitude 122°) (Figures 1-4 and 3-8). Relief increases from the San Juan Islands to the western foothills of the Cascades. Rocky cliffs are prominently exposed in the extreme eastern portion of the study area where relief is greatest. The mountains of the north Cascades are typically heavily wooded with summits that have been subdued by erosion from continental glaciers. The landscape within the study area rises to a maximum elevation of 1525 m near Canyon Lake. Thirteen kilometers east of the eastern study area boundary the local topography reaches a maximum at Mt. Baker at an elevation of 3285 m. Forests are composed of Douglas fir, western hemlock, and western red cedar while the dense undergrowth typically consists of alder, willow, salmonberry, blackberry, ferns, and devil's club. The westerly to southwesterly prevailing winds travel from the Pacific Ocean bringing heavy precipitation to the area. The average annual precipitation amounts up to 300 cm on the higher mountains (Miller et al., 1973). Most precipitation falls as rain but snow is common at

elevations above 760 m (2,500 ft) during the months of November through April (Moen, 1962). Access was obtained primarily by an extensive network of logging roads and trails.

This study focuses on three lithologies characteristic of the North Cascades: the Chuckanut Formation, Quaternary glacial sediments, and Darrington Phyllite. Large-scale, deep-seated slope instability is widespread in each unit, although topographic development is variable. The Eocene Chuckanut Formation consists of alternating intervals of **coarse-grained** and fine-grained alluvial strata. The name Chuckanut is believed to stem from “Tchuckanuts” meaning **beautiful** or bright clear water in the Chinook Indian language (Johnson, 1982). The dominant coarse-grained strata, generally less than one meter thick, is sandstone with some conglomerate and conglomeratic sandstone. The fine-grained strata, usually tens of centimeters thick, are dominated by massive or laminated siltstone and mudstone. Widespread landsliding also occurs within glacial deposits occupying valley floors and inner gorges. These unconsolidated **surficial** materials, composed of lacustrine clays, **outwash**, and glacial till, are commonplace throughout the valleys draining the west flank of the Cascades. Deposits examined in this study were located predominately in the Middle Fork of the **Nooksack** River drainage basin. The name **Nooksack** is thought to be **derived from** an Indian term meaning “fern eating people.” Both mountain-scale, deep-seated rockslides and smaller inner gorge landslides were recognized in the Darrington Phyllite. The rock is a black, graphitic, quartzose phyllite, derived from a siliceous **mudstone** (Brown et al., 1987) that is strongly foliated, and commonly folded and lineated.

The second study area is located in the Mediterranean climate of the Santa **Cruz** Mountains, central California (Figure 1-5). The Santa **Cruz** Mountains are a 120 km long, 20 km wide mountain range that separates the San Francisco Bay and Santa Clara Valley from the Pacific Ocean. The range reaches its maximum elevation in its southern portion at **Loma Prieta** (1155 m). just north of the 17 October 1989 earthquake epicenter (U.S. Geological Survey Staff, 1990). Trending northwest, parallel to the San **Andreas** Fault, the structure and relief of the Santa **Cruz** Mountains reflect both movement and deformation associated with the San **Andreas** Fault System (Anderson, 1990; Anderson and **Menking**, 1994) and compression normal to the San **Andreas** Fault (Aydin and Page, 1984; Wagner, 1990; Montgomery, 1993). The complex geomorphology of the area results from the interaction of rapid erosion and mass wasting with active tectonic surface uplift (Bradley

and **Griggs**, 1976; Nagel and **Mullins**, 1983; Spittler et al., 1990). Channels have incised deeply into the relatively weak marine sedimentary rocks that underlie the range, forming steep, narrow valleys. Landsliding is commonplace and much of the range is covered by thick unstable landslide deposits (Cooper-Clark and Associates, 1975). The area receives moderate to heavy rainfall almost entirely limited to the winter months with an average annual rainfall total of 60 to 150 cm (Rantz, 1971).

Although landslides triggered during the **Loma Prieta** earthquake occurred throughout an area of nearly 14,000 km², the highest concentration were located in the **epicentral** region (**Plafker** and Galloway, 1989). In this area, the **M_s7.1** earthquake caused strong ground motions with peak accelerations of up to 0.47 g vertically and 0.64 g horizontally only 7 km from the epicenter (Spittler et al., 1990). Thus the earthquake and related landslides provide a unique opportunity to investigate the influence of seismic accelerations on slope stability.

Using these areas as examples, the following study builds on the understanding of deep-seated **hillslope** failures as well as the long-term development and piecemeal dismantling of mountain ranges.

Figure 1-1. Rock strength and relief in a threshold landscape. Maximum material strength is mobilized in the strength limited field where relief is greatest.

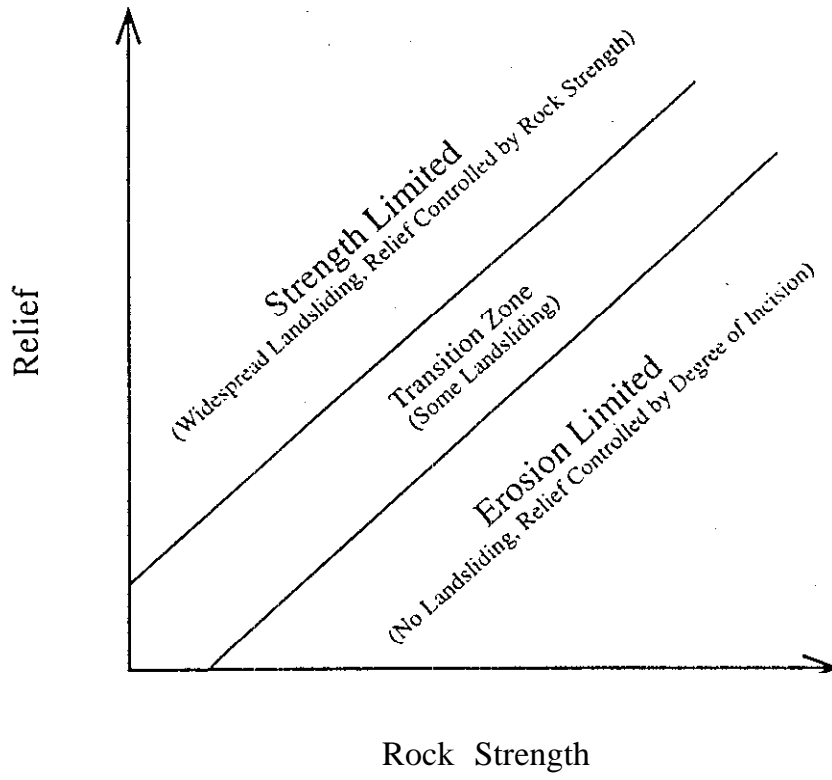


Figure 1-2. Simplified crustal section showing valley incision of a flat highland into a high relief terrain, *after* : Molnar and England (1990). Removal of crust by erosion increases relief and isostatic compensation leads to a corresponding decrease in mean elevation to $\frac{5}{6}h$ and an increase in peak elevation to $1.8 h$.

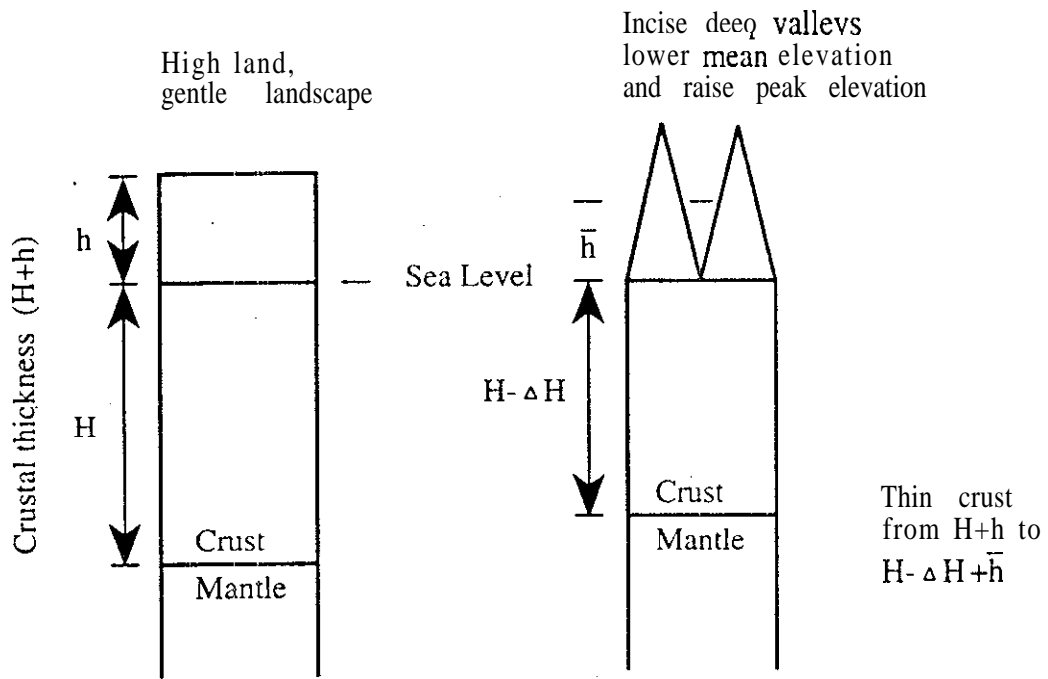


Figure 1-3. Distribution of 24 major mountain ranges of the world in the context of relief and average slope from crest to foreland. See Table 1-1 for explanation of location abbreviations.

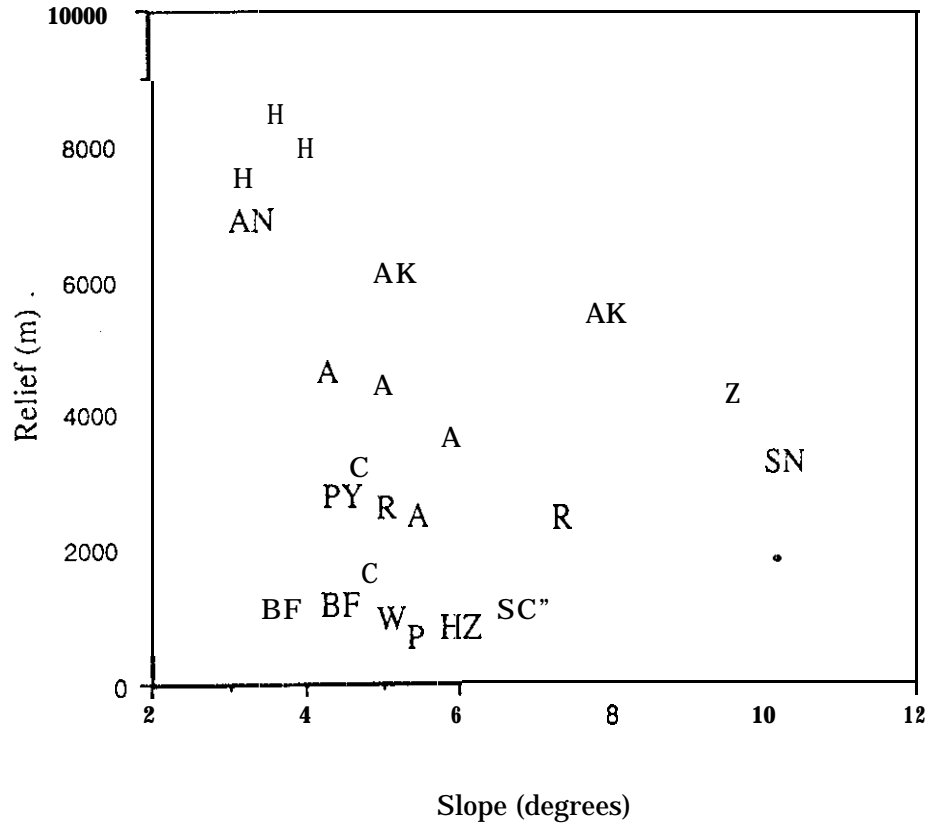


Figure 1-3. Map showing location of Chuckanut Formation and surrounding pre-Tertiary rock, including the Darrington Phyllite, *after*: Johnson (1982). Upper half of figure is a schematic geologic map of the rectangular shaded area in the lower portion. B is Bellingham; G is Glacier; S is Seattle; Vi is Victoria; NFN, MFN, SFN are the North, Middle, and South Forks of the Nooksack River.

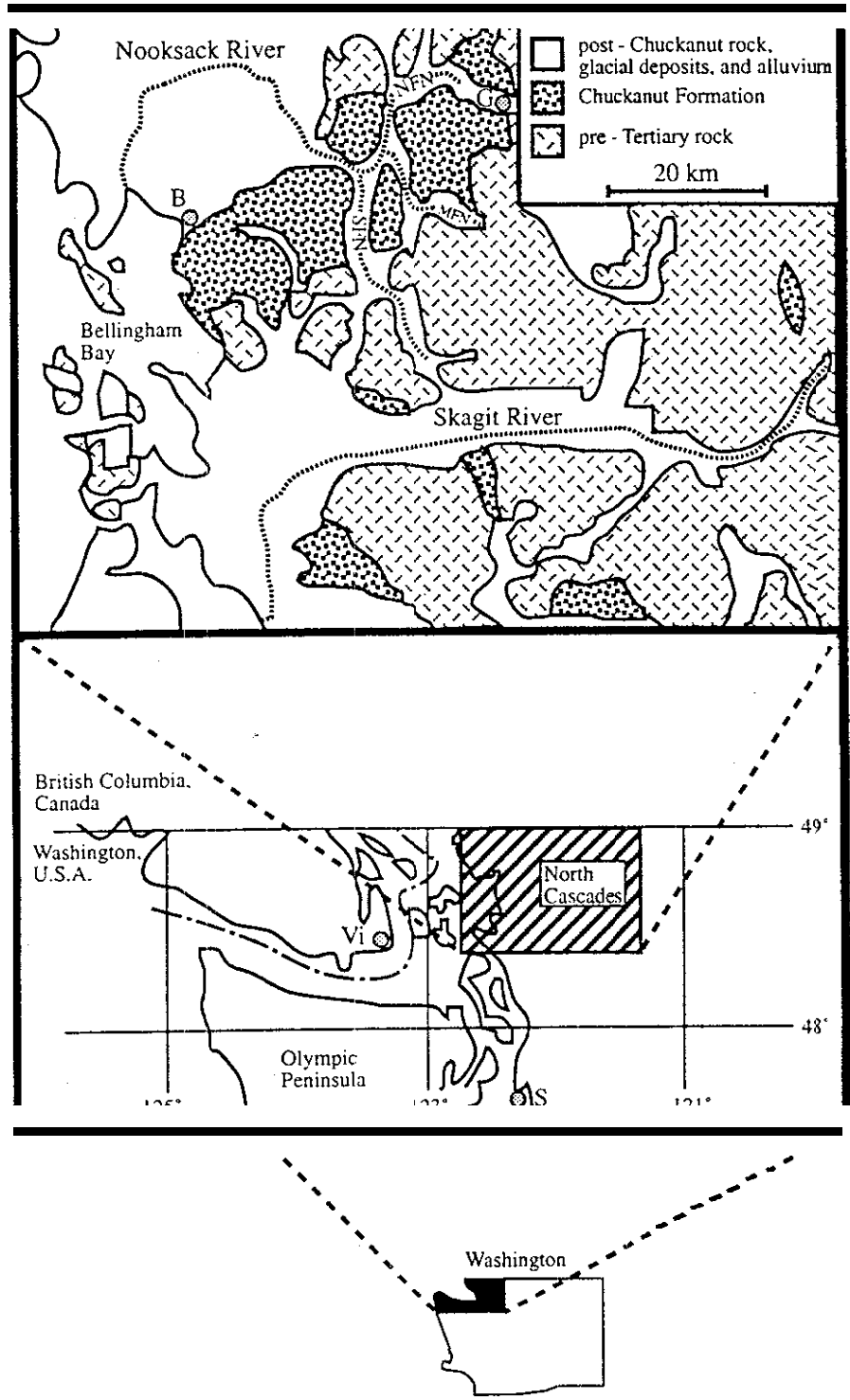


Figure 1-5. Map of California and study area in Santa Cruz Mountains. Area enclosed by dashed polygon denotes approximate boundaries of epicentral region study area. O is Oakland, SF is San Francisco, LG is Los Gatos, SCM is Santa Cruz Mtns., SC is Santa Cruz, and * represents location of epicenter of October 17, 1989 Loma Prieta earthquake.

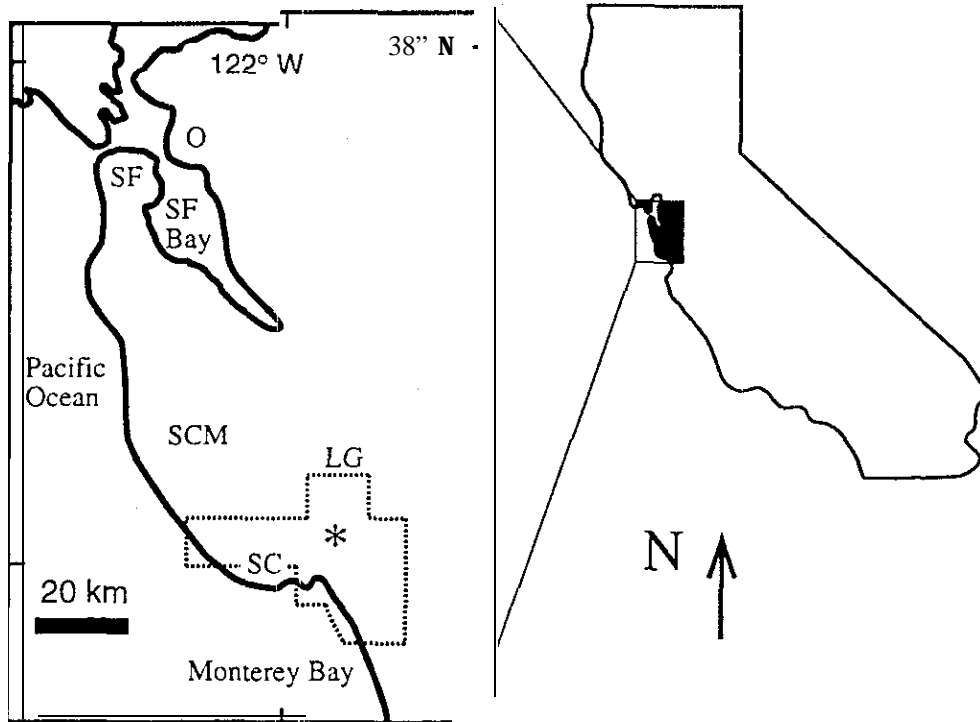


Table 1-1 Topographic attributes of 24 major mountains over the world, *after* : Ahnert (1984). Abbreviations listed after site locations refer to those used in Figure 1-3.

Location	Relief above foreland H (m)	Distance from crest to margin L (m)	Slope $\arctan(H/L)$ (degrees)
Cross Fell (Pennines-P)	770	8500,	5.18
Brocken (Harz-HZ)	900	9000	5.71
Snowdon (Wales-W)	1000	11500	4.97
Loma Prieta (Santa Cruz-SC)	1035	8750	6.70
Gd. Ballon (Vosges-V)	1160	9600	6.89
Belchen (Black Forest-BF)	1160	15500	4.28
Feldberg (Black Forest-BF)	1200	18500	3.71
Canyon Lake (Cascades-C)	1475	18600	4.50
Pike's Peak (Rocky Mtns.-R)	2350	20000	6.70
Zugspitze (Alps-A)	2350	25000	5.37
Long's Peak (Rocky Mtns.-R)	2520	29000	4.97
Pic de Neouvielle (Pyrenees-PY)	2700	35000	4.41
Mt. Baker (Cascades-C)	3135	39000	4.60
Mt Whitney (Sierra Nevada-SN)	3200	18000	10.08
Gran Paradiso (Alps-A)	3650	35000	5.95
Ruwenzori (Zaire/Uganda-Z)	4200	25000	9.54
Monte Rosa (Alps-A)	4330	50000	4.95
Mt. Blanc (Alps-A)	4400	60000	4.19
Mt. St. Elias (Alaska-AK)	5488	40000	7.81
Mt. McKinley (Alaska-AK)	6050	70000	4.94
Aconcagua (Andes-AN)	6958	120000	3.32
Nanda Devi (Himalaya-H)	7360	135000	3.12
Dhaulagiri (Himalaya-H)	7880	110000	4.10
Mt. Everest (Himalaya-H)	8400	130000	3.70

"Discoveries and inventions arise from observations of little things. "

- Thomas Edison

CHAPTER 2. STABILITY ANALYSIS: THEORY AND BACK-CALCULATED STRENGTH PARAMETERS

Characterization of hillslope stability over large regions requires an approach that is neither site-specific nor data intensive. A two-dimensional, limit-equilibrium model based solely on the attributes of material strength and topographic form satisfies these requirements. Once the topographic development and relative stability of a landscape is defined, the model analysis defined here serves as a tool to back-calculate strength properties characteristic of the lithology investigated. The following chapter discusses states of stress within a hillslope, empirical landslide morphology, and the theory of material behavior.

The methodology adopted was kept simple to examine the influence of material properties on landscape form. Thus in order to back-calculate strength parameters from observed topography, input parameters must be limited solely to those describing topographic attributes. In addition, the model must be applicable throughout landscapes with different degrees of topographic development in order to sample a range of **gravity-**induced stress regimes and define unique values of cohesion and friction angle. The failure geometry of the stability model must also be consistent with the typical observed landslide morphology as well as the predicted material behavior.

The procedure uses empirical observations of topographic development and the presence of landsliding in conjunction with a two-dimensional, theoretical stability model to arrive at back-calculated material properties. The procedure followed can be formulated as:

$$\mathbf{observation} + \text{theory} = \text{back-calculated material properties} \quad (2-1)$$

Although this usage is sound, back-analysis cannot be used to validate theory or used to develop new concepts since their conclusions directly reflect the initial assumptions (Leroueil and Tavenas, 1981).

RANKINE STRESS STATE

To investigate the effects of local relief on hillslope stability, consider the simple case of a vertical face bounding a level ground surface. These conditions are satisfied, for example, where wave action induces sea-cliff retreat or during the lateral migration of a channel against its outer bank.

The stress state within a vertical face is determined by the weight of the overlying material. The principal stress σ_1 is oriented vertically downward and is ρgH in magnitude; where ρ is the density of overlying material, g is the gravitational acceleration, H is the relief of the vertical face, and γ is the unit weight of the overlying material. Furthermore, consider an imaginary vertical wall within the ground. If the wall moves laterally, it will compress the ground on one side (increasing σ_2) and relax it on the other (decreasing σ_2). Initially the material will respond elastically to the changes in σ_2 , but when the shear strength of the material is reached, failure occurs by permanent (plastic) deformation (Scheidegger, 1961). In the case of lateral channel migration, the channel bank will expand elastically outward, slightly, relieving a portion of the horizontal stress σ_2 . Deformation will continue until a condition of equilibrium is re-established. The equilibrium stress distribution has been termed an active Rankine state.

In a passive Rankine state, compressional stresses occur at the ground surface. In contrast, the stress distribution producing tensional stresses at the ground surface is termed an active Rankine state. **Landslide** movements can be considered in the context of an active Rankine state because **downslope** deformation relaxes the confining pressure in regions of positive relief. Appendix A considers slope forming materials in the context of the **Navier-Coulomb** criterion to derive equations relating material properties and the depth of tension in a vertical face. As the confining pressure σ_2 is relaxed, for a given σ_1 , the stress condition can be represented on a **Mohr** diagram by a circle of stress with an increasing radius. The stress circle, pinned at σ_1 , increases in radius with decreasing σ_2 until failure (Figure 2-1). That is, at failure the shear stress attains the strength envelope defined by the cohesion and friction angle of the slope-forming material. The example of Figure 2-1, however, is unique to only one depth within the vertical face. The Rankine stress state for the entire height of the hypothetical face is depicted in Figure 2-2 by a dashed, diagonal

line. Rankine theory then predicts that material will be in a state of tension from the ground surface down to a critical depth Z_c , whose magnitude depends on the cohesion (c), friction angle (ϕ), and unit weight (γ) of the material.

$$Z_c = \frac{2c}{\gamma} \tan\left(45^\circ + \frac{\phi}{2}\right) \quad (2-2)$$

Tension may be expressed as one single tension crack or a zone of cracks. For more in depth discussions and derivations of equations describing Rankine stress states: see appendix A; (Rankine, 1857; Terzaghi, 1943; Terzaghi and Peck, ~1948; Scott, 1963; Wu, 1966; Carson and Kirkby, 1972).

PLANAR FAILURE SURFACE

The degree of failure-surface curvature depends on two factors: A) material properties and B) orientation of the principal stresses (or the hillslope profile responsible for the gravity-induced stress regime). Cohesion-dominated materials typically form arcuate failure surfaces, producing rotational-type landslides (Carson and Kirkby, 1972). These rotational landslides usually have depths that are a significant fraction of their length and the arcuate surfaces are well approximated by a circle. In contrast, friction-dominated materials produce planar failure surfaces leading to translational-type landslides that are shallow relative to their length. As an endmember, a cohesionless mass **cannot** stand vertically and the limiting angle of stability is equal to the friction angle. For intact rock, strength arises predominately from cohesion. When rock fractures in response to concentrated shear stresses and weathering, it transforms into a densely-packed cohesionless aggregate of angular blocks (Terzaghi, 1962). At a different scale, the remaining intact blocks of rock are approximately equivalent to grains of sand in a homogenous deposit of sand. Therefore, upon weathering, intact rock alters from a cohesion-dominated material to a relatively cohesionless, friction-dominated rock mass that would form a relatively planar failure surface. Chemical weathering may generate clays which provide cohesive strength but the relative cohesion offered through clays is essentially zero relative to the cohesion of intact rock.

Field observations reveal that landslides involving steep high relief slopes form planar failure surfaces while lower-gradient slopes tend to fail along a circular arc or logarithmic spiral (Taylor, 1948). If stresses in a rock mass are such that the principal axes lie in the same directions at all points throughout the mass, then the failure surface is planar, inclined at $\alpha = 45^\circ + \frac{\phi}{2}$ to the major principal plane (Carson and Kirkby, 1972). If on the other hand, the direction of the principal axes changes from point to point throughout the mass, the resulting failure surface is curved. For shallow failures in homogeneously inclined slopes, the major principal axis at the ground surface σ_1 is oriented parallel to the ground surface and the potential failure plane is oriented at $\alpha = \frac{1}{2}(\beta + \phi)$ to the horizontal, where β is the hillslope angle measured with respect to horizontal (Equation B-7, Appendix B). If the landslide depth is a small fraction of its length, then the failed portion of the hillslope is constrained within the near-surface region where the principal stress σ_1 is parallel to the ground surface. Therefore, the failure surface will be planar, intersecting the zone of tension cracks predicted by Rankine theory and forming a wedge-shaped block (Figure 2-3). Ranging up to 1100 m in relief, the mountain-front landslides in the Chuckanut Formation fulfill this requirement. Field observations of the landslides indicate that they are quite long compared to their depths so the principal stress orientations at the depth of the failure are presumably sub-parallel to the ground surface, validating the assumption of a planar failure surface. Similarly, empirical observations of landslide morphologies within glacial sediments warrant modeling with a planar failure surface.

CULMANN MODEL

Simple force balances in a two-dimensional, limit-equilibrium stability model can be applied to back-calculate **geotechnical** properties implied by topographic development. The sliding-wedge method of slope stability analysis (Culmann, 1875) predicts a limiting relation between hillslope gradient and relief by approximating a failure block as a wedge with a planar failure surface (Figure 2-3). The maximum stressed surface, the one with the lowest factor of safety, is a plane passing through the toe of the slope (Spangler, 1960). The force balance of shear stress and shear resistance for this geometric configuration produces the following expression for maximum slope height (H_C) :

$$H_c = \frac{4c \sin \beta \cos \phi}{\gamma [1 - \cos(\beta - \phi)]} \quad (2-3)$$

(see Appendix B for derivation). The limiting relation of equation 2-3 depends on the attributes of topography (gradient and **relief**) and material properties (cohesion, friction angle, and unit weight).

In reality, however, failure surfaces are neither strictly planar nor circular but some union of the two. The influence of selecting a planar failure surface, rather than a circular one, on relative stability has been reviewed by Taylor (1937; 1948). Using a spectrum of slope gradients and friction angles, the relative critical heights predicted by these two methods can be compared through the stability number: $\frac{C}{F W H}$ where F is the factor of safety and W is the weight of the block. A comparison of the planar failure surface Culmann method with the Jaky f-circle method (Taylor, 1937) that approximates the failure surface as a circle reveals that for hillslopes between 45° and 90°, the Culmann method predicts a 16% lower stability number. If all other variables are held constant, a lower stability number reflects a larger critical height. For hillslopes with shallower gradients of 15° to 45°, the discrepancy between these two methods rises to 56% with the Culmann method predicting stability for greater heights. Thus, strength parameters back-calculated using the Culmann method will be greater than those obtained from an arcuate failure surface method. However, as previously mentioned, field observations indicate that the landslides studied exhibit planar, translational failure surfaces and thus are appropriately represented by a wedge-shaped failure.

PREVIOUS STUDIES OF SLOPE/HEIGHT RELATIONSHIPS

Prior research using the Culmann model is limited to soils or soft rocks forming vertical or steep slopes. For example, it has been applied to friable **loess** deposits in Iowa by Lohnes and Handy (1968). to coastal bluffs composed of glacial deposits by **McGreal** (1979). and to **loess-derived** alluvium in Tennessee by Simon (1989) and Simon and Hupp (1992) but not in larger-scale bedrock landscapes. Other studies recognizing a slope/height limit to stable slopes include that of Skempton (1953) for clay strata in England and the work of Grant-Taylor (1964) on weathered greywacke in New Zealand.

The research on slope angles in friable loess by Lohnes and Handy (1968) is the most rigorous study located using the Culmann model. Strength properties back-calculated using the Culmann approach for high gradient slopes up to 60 m in relief composed of friable loess in Iowa and Tennessee were compared with strength properties obtained through in situ **borehole** shear tests. Strong correlation was found between parameters back-calculated from the observed topography and those obtained from **borehole direct-shear** tests. In addition, it was noted that observed modal frequencies of slope angles indicate a sequence of progressively gentler gradients generated by continued landsliding. This observation is in agreement with the sliding-wedge analyses of the Culmann model which predicts a failure plane oriented at $\alpha = \frac{1}{2}(\beta + \phi)$ to the horizontal. Thus, removal of landslide debris above the failure plane through numerous landsliding events results in progressively gentler gradient hillslopes over time.

McGreal (1979) applied the Culmann model to retreating coastal bluffs composed entirely of glacial sediments in N. Ireland. The bluffs ranged between 5 and 15 m in relief with gradients between 60° to 90°. Because of the rapid rate of cliff retreat triggered by basal marine erosion, it was thought that the cliff morphologies represent a response to the “current” climatic, groundwater, and marine conditions.

Stream channel response to disturbances such as dredging and straightening in loess-derived alluvium has been studied by Simon (1989) and Simon and Hupp (1992). It was observed that mass wasting of channel banks in West Tennessee is commonplace after channel modifications. The channel bank shear strength determines bank stability and long-term channel morphology. Slope/height relationships are used to define comparative hazard categories of “unstable”, “at risk”, and “stable” for channel banks of different topographic morphologies.

Related research noting a **slope/height** relationship in the relative stability of a landscape includes the pioneering work of Skempton (1953). Introducing the concept of the “activity” of clays, this classic soil mechanics study investigated rotational slumps in boulder clay driven by valley deepening and undercutting of channel banks. Skempton determined that “deep slips” occur in regions of high relief and steep slopes, in contrast to stable slopes which typically have gentle slopes and lower relief. It was suggested that the

processes of downcutting, undercutting, and landsliding caused valley deepening shallower hillslope gradients. Gradients decrease for the same reason modal slope frequencies were identified in Lohnes and Handy (1968): progressive landsliding relaxes the hillslope gradient as the slope approaches the angle of repose.

In the study of intensely jointed greywacke in New Zealand. Grant-Taylor (1964) suggested that two slope/height thresholds exist for the one lithology studied. One threshold was recognized for relatively intact rock and one for intensely sheared rock near a fault zone. It was also concluded that the effectiveness of rock strength decreases rapidly with increases in relief.

Engineering projects such as quarry excavations and earth dam dimensions have also used slope/height relationships in design (Lane, 1961; Ross-Brown, 1973; Hoek and Bray, 1977).

HOEK AND BRAY PLANE FAILURE MODEL

Expanding on the simple relationship of the Culmann model, a more rigorous approach including the effects of groundwater conditions, cleft and uplift pressures, is presented in Appendix C; Figure 2-4; and Hoek and Bray (1977). In addition, the modifications in the Hoek and Bray approach allow for headscarp locations in the upper slope surface as well as in the slope face. The following assumptions are made in this analysis:

- 1) Both sliding surface and tension crack strike parallel to hillslope surface.
- 2) The failure plane must daylight in the slope face, i.e. $\beta > a$.
- 3) The failure plane dip must be greater than the friction angle, i.e. $\alpha > \phi$
- 4) The tension crack is vertical and may be **filled** with water to a maximum depth of Z_w .

5) The pore pressure distribution in the tension crack and failure surface is illustrated in Figure 2-4. Atmospheric equilibrium occurs where the failure surface daylights on the hillslope face and at the top of the water column in the tension crack.

6) The weight of the sliding block, W , the uplift force due to positive pore pressure, U , and the force due to water pressure in the tension crack, V , all act on the centroid of the sliding mass. Failure is by sliding, translational movement only.

7) The shear strength of the sliding surface S is defined by cohesion, c and friction angle, ϕ which are related by $S = c + \sigma \tan \phi$.

8) The model considers a slice of unit width and it is assumed that there is no resistance to sliding at the lateral boundaries of the failure block.

With these assumptions the factor of safety, F , is:

$$F = \frac{cA + (W \cos \alpha - U - V \sin \alpha) \tan \phi}{W \sin \alpha + V \cos \alpha} \quad (2-4)$$

where from Figure 2-4, the strip of unit width over which cohesion acts:

$$A = (H - Z) \operatorname{cosec} \alpha \quad (2-5)$$

the uplift force due to water pressure on sliding surface:

$$U = \frac{1}{2} \gamma_w Z_w (H - Z) \operatorname{cosec} \alpha \quad (2-6)$$

where γ_w is the unit weight of water and Z_w is the depth of water in the tension crack.

The cleft pressure, uplift force due to water pressure in tension crack is:

$$V = \frac{1}{2} \gamma_w Z_w^2 \quad (2-7)$$

For the tension crack in the upper slope surface the weight of the sliding block is:

$$W = \frac{1}{2} \gamma H^2 \left\{ \left[1 - \left(\frac{Z}{H} \right)^2 \right] \cot \alpha - \cot \beta \right\} \quad (2-8)$$

and for the tension crack in the slope face the weight of the sliding block is:

$$W = \frac{1}{2} \gamma H^2 \left[\left(1 - \frac{Z}{H} \right)^2 \cot \alpha (\cot \alpha \tan \beta - 1) \right] \quad (2-9)$$

In order to simplify calculations, equation 2-4 is expressed in dimensionless form. For derivations and further details see Appendix C.

This more detailed procedure is used in the analysis of Chapter 3 to back-calculate strength parameters from observed topographic development for the Chuckanut Formation, Quaternary glacial sediments, and marine sedimentary units of the Santa Cruz Mountains.

While the influence of discontinuities in soils can be adequately represented by modified bulk parameters, discontinuities in rock each have their own individual effect, This creates a significant problem in the application of continuum analysis, stress/strain relationships, and hydrologic analysis” However, limit-equilibrium analyses, such as the stability analysis adopted in this study, are not influenced by this issue.

REGIONAL STRENGTH PARAMETERS

Development of topography is controlled by erosional processes, uplift rates, base level changes, and material strength over long time scales. The erosional activity of rivers, landslides, and glaciers incise into a landscape, increasing both the local and range-wide relief. It is postulated, however, that a limit to relief development exists where the full material strength is engaged. Figure 2-5 represents a simplified landscape increasing in relief over time. Gravitational stresses within the hillslope increase to a point where the shear stresses arising from the gravitational weight of the mountain surpass the shear resistance of the rock and failure begins.

Topographic development is the expression of the competing forces of shear stress and shear resistance. It is thought that strength parameters back-calculated from the distribution of topographic development reflect the *in situ* strength of geologic formations over spatial scales of tens to hundreds of square kilometers. Unless landsliding is prevalent, this natural test of available material strength will only yield minimum values. It is assumed that the strength of existing hillslopes is at least that required to maintain their present topographic equilibrium. Those portions of the landscape with wide-ranging instability, such as expressed in the Chuckanut Formation and inner gorges composed of glacial sediments, represent areas where the full material strength has been engaged. Therefore, strength parameters back-calculated from these widely unstable lithologies represent the maximum strength attributable to the unit.

Terzaghi (1962) presents a clear discussion of why intact rock strength is practically irrelevant to the problem of slope stability, and how the character of the mechanical defects, the discontinuities, determine the relative stability. Back-calculated *in situ* strength parameters, however, include the local weaknesses and reinforcements that are manifest in the overall slope morphology, gradient, and relief. These strength parameters mirror a hillslope's geologic past: through its present geomorphic expression. Back-calculated values reflect the history of slope formation, recording all extreme events such as elevated pore pressures and seismic accelerations. Strength measurements determined by direct field or laboratory testing methods, over the scale of a **hillslope**, are difficult to ascertain. Furthermore, they do not reflect time-integrated properties modified by extreme geologic events attainable through back-calculation.

Because strength parameters are defined by a range of stress conditions, a series of hillslopes with different geometries and sizes must be analyzed to cover a range of **gravity**-induced effective stress conditions. Topographic development, defined from map evidence and field surveys, in conjunction with Hoek and Bray's modified Culmann method provide the tools necessary to analyze regional strength parameters. Given the distribution of topographic development and its relative stability, unique values of cohesion and friction angle can be back-calculated. Material parameters are obtained by fitting a curve to the threshold above which there is no observed topography for a given lithology (Figure 2-6). This threshold has been termed the limit to topographic development, or LTD, and is a simple function of hillslope gradient and relief or alternatively friction angle and cohesion.

Landscapes with high limits to topographic development are composed of strong rock, can support deeply incised valleys, and have a high resistance to landsliding. Alternatively, landscapes with low limits to topographic development are composed of relatively weak material, can express only moderate relief and gentle gradients, and are highly susceptible to widespread landsliding. Choosing a representative unit weight, combinations of cohesion and friction angle are interpolated to locate the strength curve best suiting the observed limit of relief development for a given lithology. The slope gradient asymptote (abscissa) of the LTD in Figure 2-6 is determined by the cohesive strength. Similarly, the relief asymptote (ordinate) is defined the frictional resistance.

STABILITY ANALYSIS INCLUDING SEISMIC ACCELERATIONS

Recent research has identified a history of active tectonics in the Puget Sound region (Schedlock and Weaver, 1991; Atwater and Moore, 1992; Bucknam et al., 1992). In addition, earthquakes are commonly recognized as the triggering mechanism for numerous landslides in a broad expanse surrounding an earthquake epicenter (Keefer, 1984; Wilson and Keefer, 1985). Other studies in the Puget Sound region circumstantially linking landslides with earthquakes include those of Schuster (1992), Jacoby (1992), and Keefer (1983).

To evaluate this aspect of extreme geologic events capable of producing widespread instability, the original Culmann model was modified to include the effects of seismic accelerations. The influence of earthquakes on relative stability was examined by considering seismic accelerations as equivalent static forces. Appendix D details the equation derivations for horizontal accelerations while Appendix E describes those related to vertical accelerations.

Figure 2-1. Stress state represented by Mohr stress circle. Stress circles of increasing radius are defined by the invariant overburden, σ_1 , and a decreasing σ_2 . Failure occurs when the stress circle reaches the strength envelope defined by $\tau = c + \sigma \tan \phi$.

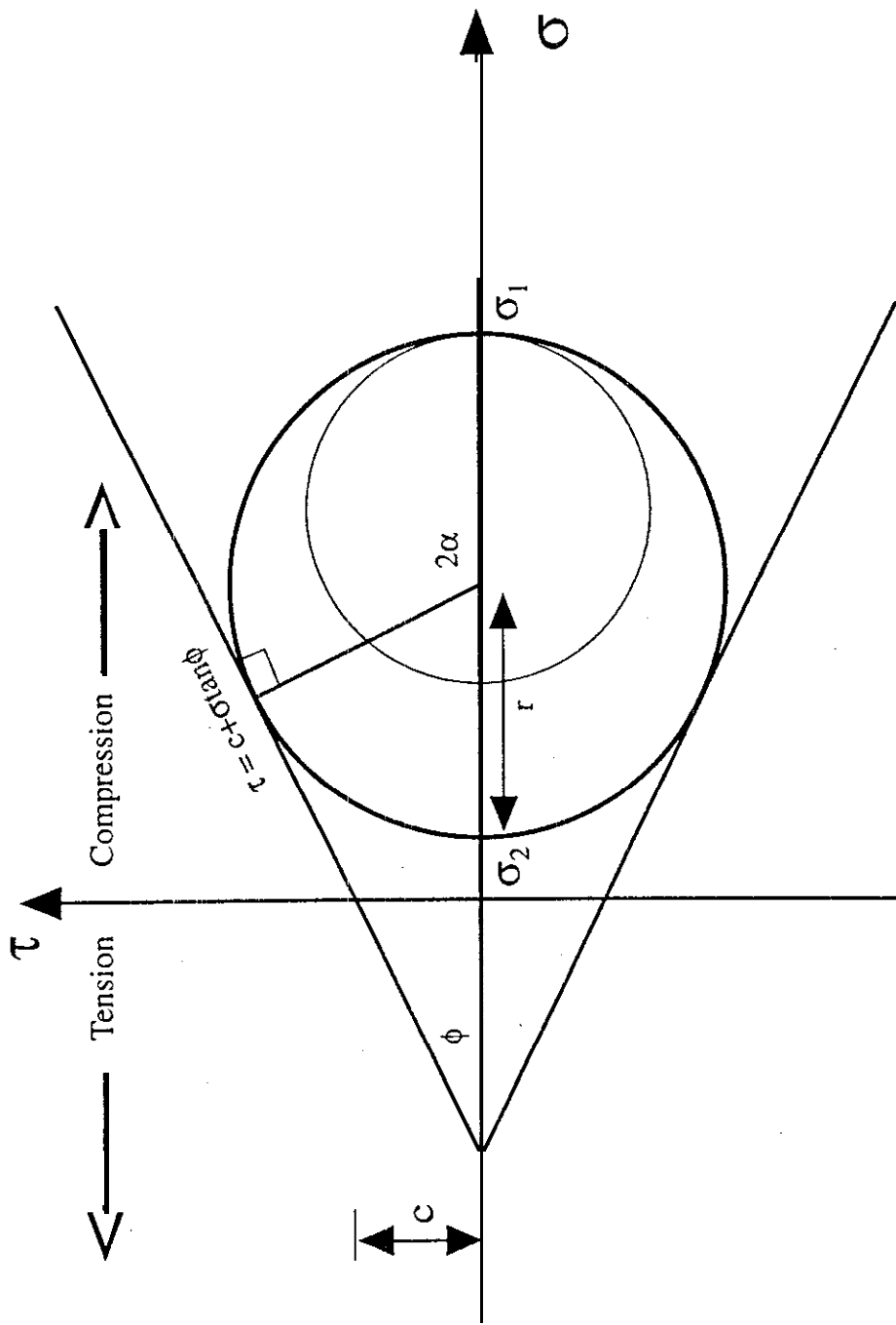


Figure 2-2. Stress state in vertical face bounding a horizontal surface. Dashed line depicts relative increase of σ_2 with overburden weight σ_1 predicted by Rankine theory. From the ground surface down to a maximum depth of Z_c the mass is in a state of tension.

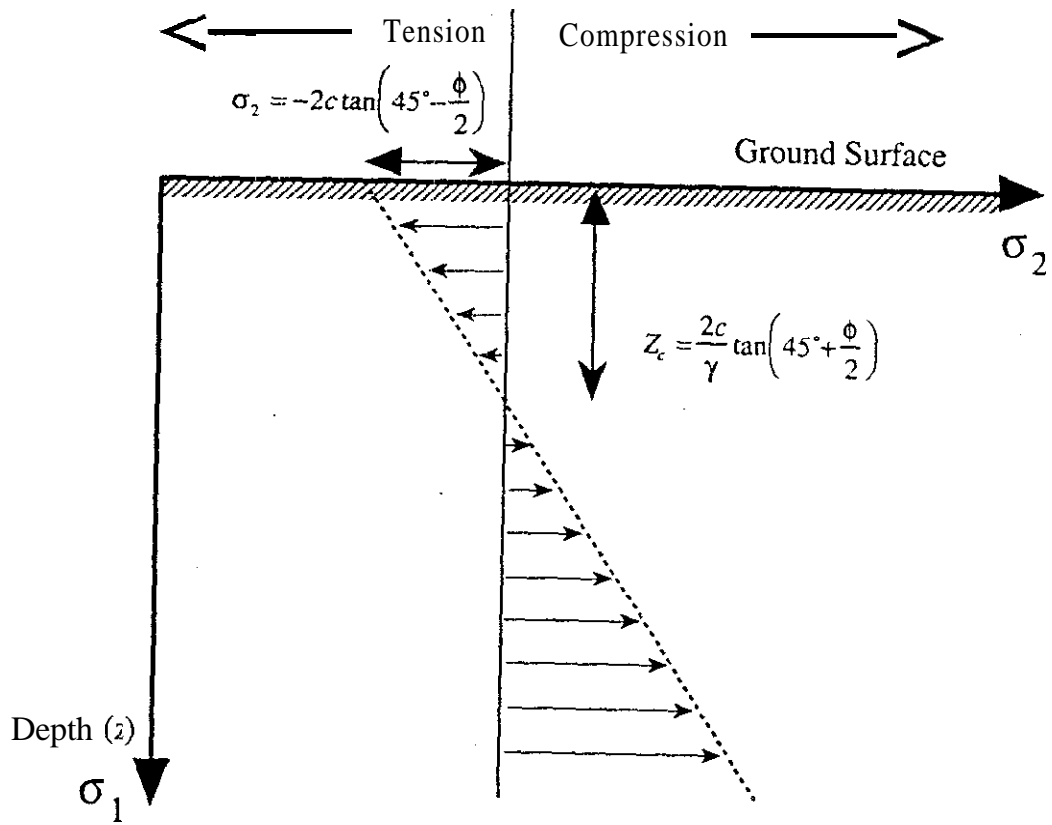
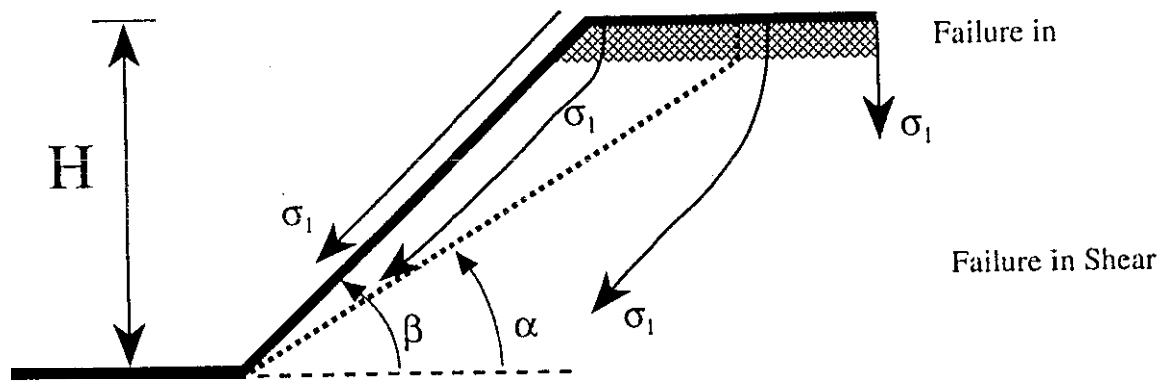


Figure 2-3. Wedge-shaped landslide block defined by planar failure surface (dashed line) intersecting zone of tension determined by Rankine theory. From the surface to shallow depths the gravity-induced principal stresses σ_1 is oriented approximately parallel to hillslope of unvarying inclination, β , and the failure surface is inclined at $\alpha = \frac{1}{2}(\beta + \phi)$ to the horizontal. Failure represents conditions satisfying the Culmann model.



where $\alpha = \frac{1}{2}(\beta + \phi)$

Figure 2-4. Graphical representation of input parameters in plane failure stability model adapted from Hock and Bray (1977). Because the geometry and thus the weight of the potential failure block depends on the vertical tension crack position, two versions are presented: A) headscarp in upper slope surface characteristic of failures in glacial sediments, and B) headscarp in slope face characteristic of bedrock failures in the Chuckanut Formation. Variables are explained in text and Appendix C.

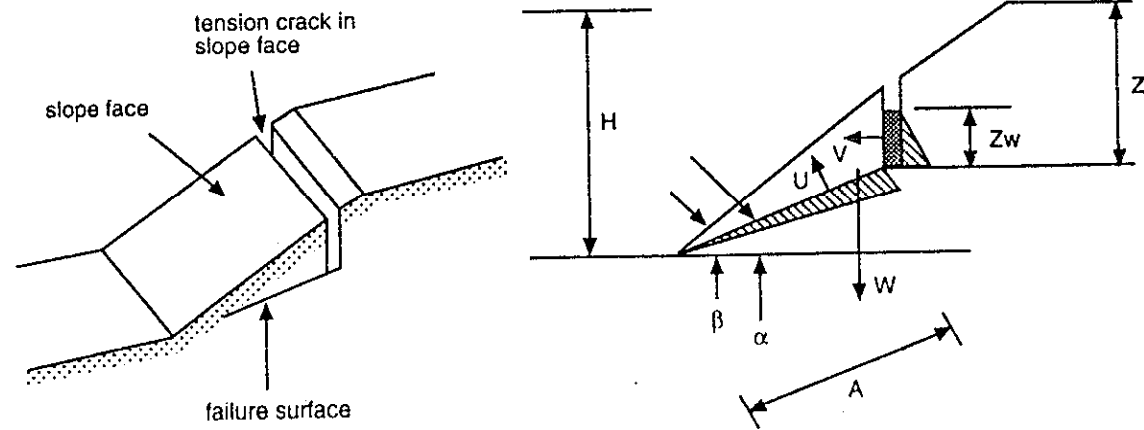
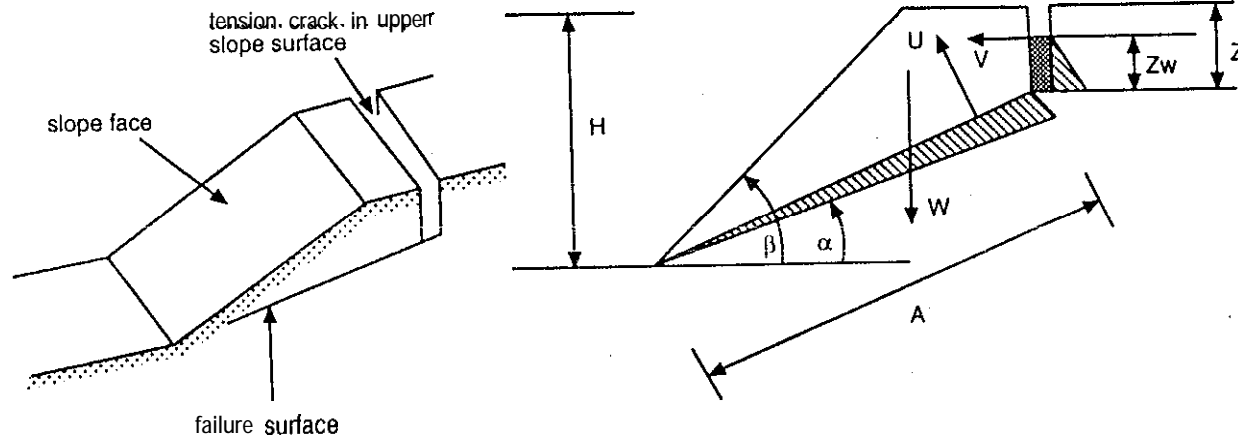
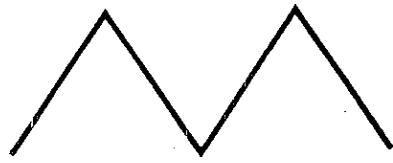
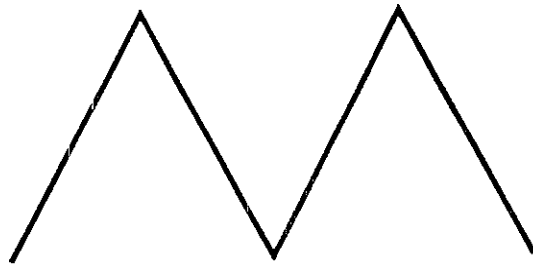


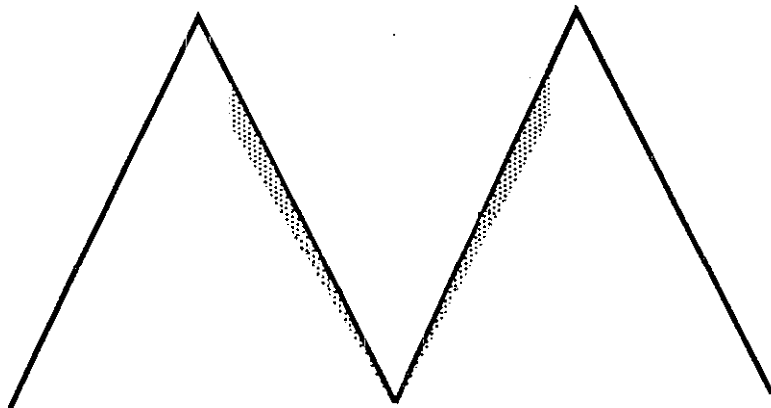
Figure 2-5. Hypothetical topography increasing in relief H over time t . Relief increases until onset of landsliding (depicted as stippled pattern). Bedrock landsliding then serve as a feedback mechanism limiting further relief development from channel incision.



H_1, t_1

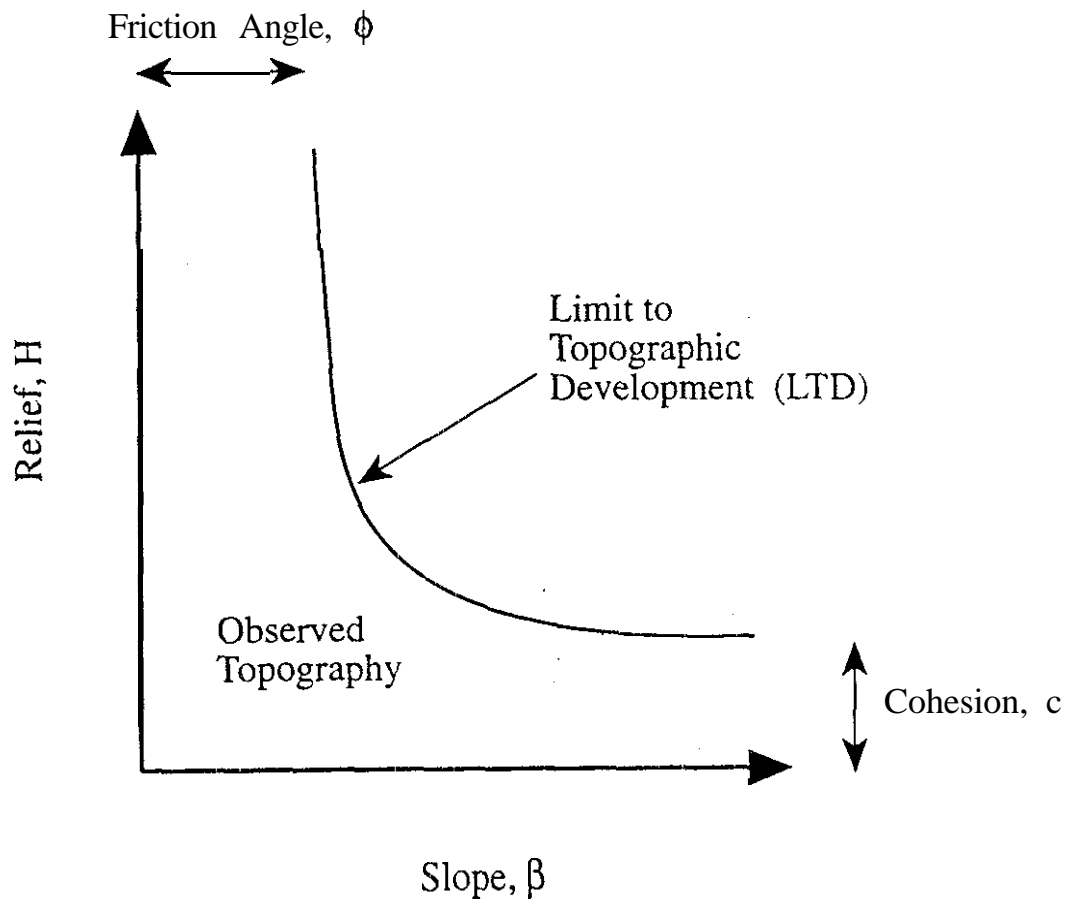


H_2, t_2



H_3, t_3

Figure 2-6. Limit to topographic development (LTD) defined by features of observed topography (hillslope gradient and relief). The LTD relief asymptote is determined by the friction angle while the slope asymptote is controlled by cohesion.



*"The essence **of** knowledge is, having acquired it, to apply it."*

- Confucius (450 B.C.)

CHAPTER 3. BACK-CALCULATED MATERIAL PROPERTIES

The following chapter applies the theory developed in Chapter 2 and Appendices A, B, and C to determine regional strength properties from topographic development of Quaternary glacio-fluvial deposits, the Chuckanut Formation, the Darrington Phyllite, and sedimentary units of the Santa Cruz Mountains.

NORTHWEST CASCADES STUDY AREA

The rugged topography of the Cascade Range reflects the influences of uplift, fluvial erosion, Quaternary volcanism, and repeated glaciation (both alpine and continental). Extending roughly parallel to the Pacific Coast from northern California into southern British Columbia, this major mountain chain induces significant orographic precipitation from marine air flowing eastward off the Pacific Ocean. The western flank of the northern Cascades are consequently covered by dense evergreen forests and a host of lakes and streams.

During the Fraser (Late Wisconsin) Glaciation, the Cordilleran ice sheet advanced southward from source areas in British Columbia (Crandell, 1965). In the study area of northwestern Washington, alpine glaciers reached maximum positions between 22,000 and 18,000 yr. B.P. and had largely diminished before the Cordilleran ice sheet entered the Puget lowland between 17,000 and 13,000 yr. B.P. (Waitt and Thorson, 1983). During its maximum stand, the Cordilleran ice sheet buried much of the northern Cascade Range (Waitt and Thorson, 1983), including the entire study area. At its maximum extent ice covered most of this high-relief landscape, overriding divides and inundating major drainage basins; only peaks greater than 1830 m (6,000 ft) were left as nunataks. The generalized isopach map of Thorson (1981) indicates ice thickness of at least 1300 m in the study area.

Thorson (1981) infers that the area just south of the United States-Canada border experienced at least 140 m of vertical post-glacial uplift in less than 13,000 years. It is

assumed that the bulk of this deformation results from isostatic compensation driven by the removal of the Cordilleran ice sheet. If the 140 m estimate is adjusted for the maximum error expected in **representing the** height of **eustatic** sea level (20 m), and adjusted for an additional 10 m of post-glacial deformation unrelated to glacial isostasy, the minimum magnitude of the original post-glacial isostatic anomaly is about 110 m (Thorson, 1981). Using the 110 m isostatic anomaly estimate and assuming a constant uplift rate, minimum mean uplift rates in the study area would be 8.5 mm/yr averaged over the 13,000 years since deglaciation.

Supporting evidence for large vertical displacements of the landscape may be inferred from the presence of inner gorges. Along valley side-slopes, steep hillslope gradients adjacent to the channel are separated from lower-gradient slopes further **upslope** by clearly defined breaks-in-slope (Figure 3-1). Formation of inner gorges are thought to reflect downcutting in response to base level lowering (Kelsey, 1988). The common occurrence of inner gorges in the northwest Cascades implies that the area experienced either significant surface uplift or persistent base level lowering. Downcutting also increases the probability of landslide initiation by steepening hillslope gradients. Another control on inner gorge formation includes valley glacier rebound. A study by Matheson and Thomson (1973) suggests that valley bottom deformation may induce gouge zones at the base of the valley. The presence of such gouge zones would have great bearing on landslide susceptibility.

Geometric properties of hillslopes underlain by: 1) Quaternary glacio-fluvial deposits forming channel banks in river valleys, 2) the strongly bedded Eocene Chuckanut Formation, and 3) the Darrington Phyllite are used to evaluate regional, in *situ* material strength properties. The north Cascades region was chosen because of numerous recognized bedrock landslides up to 1100 m in relief as well as pronounced mass wasting along incised channel banks. The schematic cross section of Figure 3-1 shows the relative positions of mountain-front and inner-gorge landslides.

The density of transects used to characterize topographic development of the following lithologies does not represent a random sampling. Rather, transects were generated for sites of deep-seated landsliding identified either in the field or from aerial photographs. Transects for stable locations, however, were selected without conscious

bias. All transects were oriented perpendicular to the long axis of topography and surface topographic contours following the maximum downslope gradient. Horizontal and vertical measurements extend from ridgecrest to the break in slope at the valley floor to represent relief and horizontal base length. The basal break in slope usually corresponded with the location of the channel in the valley bottom. Average hillslope-scale slopes were calculated. Strength properties for Quaternary glacial sediments and the Chuckanut Formation were back-calculated using the Hoek and Bray failure model presented in Appendix C.

QUATERNARY GLACIAL SEDIMENTS

Material Description

The advance of the Cordilleran ice sheet southward into the Puget lowland during the Fraser Glaciation dammed northward and westward flowing rivers. In the valleys west of the Cascade crest, lakes were **ponded** between thick ice in the Puget lowland and Cascade mountain glaciers (Porter et al., 1983). The resulting ice-margin lakes accumulated silt and clay. Meltwater streams issuing from the advancing ice deposited **outwash** sands that were subsequently overtopped by ice and covered with till (Easterbrook, 1979).

From the perspective of regional channel bank stability analysis, glacial sediments are considered as a single unit even though they are composed of varied sequences of stiff, laminated lacustrine clay overlain by **outwash** sands and gravels that was subsequently capped by a boulder till. Deeply-incised glacial deposits are ubiquitous along the mountain fronts and throughout the valleys draining the west flank of the Cascades. These unconsolidated **surficial** materials appear mostly as low-gradient terraces (Fiksdal and Brunengo, 1981). To portray topographic development within the glacial deposits and their **fluvial** reworkings, channel bank and terrace edge geometries were field surveyed in the drainage basins of the Middle Fork of the **Nooksack** River (199 km^2 drainage area), Clearwater Creek (59 km^2 drainage area), Rocky Creek, and Boulder River. In the Middle Fork of the **Nooksack** River valley, glacial sediments form flat-topped benches up to 150 m thick. Channels incised into these sediments are predominately floored with glacial sediments and thus lack base level control provided by coherent bedrock.

Failure Character and Location

The numerous landslides within glacial deposits of the valley floors slide directly into adjacent channels (Figures 3-1 and 3-2). Stability decreases as material is removed through vertical incision into the channel bed or lateral migration undercutting the channel bank. Both processes lead to an apparent increase in channel bank relief and/or gradient. Although the resulting failures are usually small in volume relative to the mountain-front landslides, they represent a large sediment source entering adjacent channels (e.g., Kelsey, 1988).

Field observations suggest that topples become critical early in the downcutting phase followed by activation of larger slumps. For example, only those oversteepened reaches in the apex of meander bends produce well-developed slumps (Figure 3-3). Topple failures are commonly located at the upstream and downstream ends of meander bends while slumps are found at the apex of the bend, the location of maximum present undercutting and removal of material. Apparently, the full material strength is engaged only in high sinuosity reaches.

Method of Analysis

A total of 178 transects were **field** surveyed along four channels incised into Quaternary **glacio-fluvial** deposits: the Middle Fork of the **Nooksack** River, Clearwater Creek, Rocky Creek, and Boulder River. Topographic profiles extending from upper terrace surface to the approximate level of **bankfull** discharge were generated with tape, stadia rod, hand level, and transit compass. Measurements include channel banks in reaches with floodplain banks and terrace margins that rise above the **bankfull** channel. Additionally, sites were classified into three groups according to relative stability: 1) stable banks, 2) topples, and 3) slumps. Stable sites were defined by the presence of a regolith and mature vegetation, i.e. moss, ferns, and conifers. Exposed cliffs lacking soil development, vegetation or an organic detritus layer, an arcuate headscarp or scalloped appearance, and a defined landslide block were classified as inferred topples (Figure 3-4). Topple failures were also distinguished by a sharp break in slope between the steep,

exposed channel bank face and the upper bench surface. Although topples were often distinguished by failed debris at the base of the channel bank, many sites displayed no failure mass, as it was presumably removed by **fluvial** erosion. Even so, they were classified as inferred topples because of their scarred, exposed appearance. Landslides were classified as slumps only if the landslide block, often with back-rotated trees, was still recognizable (Figure 3-5).

Downslope material transport from landsliding alters **hillslope** morphology such that only the present, post-failure topographic profiles of slumps could be directly measured. Pre-failure profiles, though, were estimated in cases where conditions required for reconstruction were met. To reconstruct pre-failure topography, the terrace surface must have a homogenous slope and the limit of horizontal extension toward the channel must be constrained by stable channel banks adjacent to the failure. Ideally, pre-failure topography would be obtained for all sites but reconstruction was typically not possible. The **upslope** extent of topples and slumps characteristically extend into the upper terrace surface (Figure 3-1) and are subsequently modeled with the equations in Appendix C corresponding to a tension crack in the upper slope surface.

In *situ* strength estimates of **outwash** sands were obtained with a variably loaded cup sheargraph. Till and clay horizons could not be characterized by this method because of their high densities and subsequent inability to properly seat the instrument cup.

Back-Calculated Strength Properties

The topographic characteristics of stable channel banks, topples, and well developed slumps (both pre- and post-failure) is displayed in Figure 3-6. It should be noted that there is a stratification with respect to stability. Stable sites cluster at base of Figure 3-6a at low to moderate slopes and low relief. Topples plot at moderate to high slopes and low to high relief while slumps occur on moderate gradient taller banks. Where reconstruction was possible, pre- and post-failure slump morphologies are linked by **tie-**lines for a particular profile. For the purposes of defining the **LTD**, reconstructed **pre-**failure morphologies carry more validity than post-failure slump morphologies because they represent the maximum topographic development. Figure 3-6b, displaying the same sites as Figure 3-6a, reveals a roughly linear relationship between relief and base length.

This linear distribution demonstrates that in a regional approach to stability, the glacial deposits can be evaluated as a single homogenous unit with a relatively similar strength even though stratigraphic sequences vary throughout the study area.

The distribution of topples along with the reconstructed pre-failure slump morphologies were used to fit the limit to topographic development threshold of Figures 3-6a & b. The back-calculated threshold envelope yields strength values of $\phi=29^\circ$ and $c=20$ kPa with $\gamma=20$ kN/m³ for the stratigraphic package treated as a single, dry unit. For comparison, *in situ* values obtained in the field using a variably loaded sheargraph in a sand/silt **outwash** deposit produced average values of $\phi = 36 \pm 11^\circ$ and $c = 12 \pm 9$ kPa determined by 23 measurements at 3 representative sites.

Pore pressure distributions were approximated by the extreme conditions of dry hillslopes (no positive pore pressure) and complete saturation. The field of instability defined by the saturated threshold for back-calculated strength values is supported by the spatial distribution of post-failure and reconstructed pre-failure slump morphologies (Figure 3-6). All pre-failure geometry reconstructions plot above or adjacent to the strength threshold at saturated conditions. Post-failure geometries express a lower gradient and are thus farther removed from the strength threshold at saturation. Because the model assumes hydrostatic conditions at saturation, the remaining failure sites positioned below the threshold for saturated conditions may result from excess pore pressures or seepage forces. Figure 3-7 represents process domains defined in the context of topographic development and **hillslope** stability. Arrows on the LTD at saturation represent the apparent decrease in stability in response to forces not considered in the model analysis such as pore pressures greater than hydrostatic, seepage forces, and seismic accelerations. The stratigraphic package of lacustrine clay, **outwash** sands, and boulder till provides a sequence of high conductivity sands sandwiched between two low conductivity layers. Groundwater may become trapped between the clay and impermeable till raising pore pressures above hydrostatic conditions within the sandy **outwash** layer. In addition, seepage forces, which represent a body force proportional to the hydraulic potential gradient are often responsible for destabilizing hillslopes. In the horizontally bedded glacial sediments it is most probable that seepage vectors are oriented horizontal, parallel to bedding. Seepage vectors directed horizontally out of a free face, **such** as a channel bank, represent the condition of minimal slope stability (Iverson and Major, 1986).

Predicted Tension Depth and Observed Maximum Height of Vertical Channel Bank

The critical depth of tension predicted by the Rankine stress state, Z_c , was used to evaluate the maximum stable height of channel banks in glacial sediments of Nooksack River drainage basin. The state of tension adjacent to a free face such as a channel bank extends down to a critical depth depending on the cohesion, friction angle, and unit weight of the material predicted by the relation of equation A-6. Using the strength parameters back-calculated from the threshold curve of Figure 3-6, the maximum depth of tension predicted by Rankine theory is 3.4 m, in eminent agreement with the measured maximum height of 3.5 m for a vertical channel bank.

Channel Bank Incision and Evolution

Because failure plane inclinations are shallower than the pre-failure hillslope gradients, removal of failure debris from large slumps serves to decrease channel bank gradients and widen valley floors. With progressive downcutting and repeated channel bank landsliding, successively lower-angled slopes emerge in accordance with equation B-7: $a = \frac{1}{2}(\beta + \phi)$. In contrast, the smaller volume topples do little to reduce channel bank gradients or increase valley width. The presence of the relatively larger deep-seated slumps along a reach should be indicative of the most unstable, rapidly widening section that has previously experienced a slower widening phase by topples. Furthermore, the frequency of landsliding may be accelerated by changes within the drainage basin.

Effect of Timber Harvesting

Unstable, deeply incised reaches have a high potential for impacting channels through rapid introduction of large volumes of sediment from channel bank landsliding (Kelsey, 19888). Recent rain-on-snow studies (Megahan, 1983; **Harr**, 1986; Berris and **Harr**, 1987) suggest that timber removal in the transient snow zone can significantly alter the hydrologic response of a basin. Vegetation cover controls the amount of water reaching the soil and the amount held as stored water through a combination of interception and evapotranspiration. In a comparison between forested and clear-cut plots Berris and **Harr** (1987) discovered that in the largest rain-on-snow event measured, water output from the

clear-cut plot was 21% greater than from the forested plot. This output increase would more than double the apparent size of the return interval for a given rainfall event. Higher peak flows indicate a higher rate of delivery to soils which in turn suggests increased potential for both hillslope and channel erosion through increased frequency and magnitude of saturation.

Most of the sites along the Middle Fork of the Nooksack River are located at elevations or downstream of areas susceptible to rain-on-snow events. Those sites situated above the saturated threshold in Figure 3-6 may be considered potentially susceptible to failure resulting from changes in the hydrologic response of a basin. Failure susceptibility is increased because the probability of attaining fully saturated conditions is heightened by vegetation removal.

The destabilizing effect of post-logging strength reduction due to the loss of tree root cohesion on slope stability is thought to be minimal because the landslide surfaces are located below the depth of root penetration.

In summary, the highest degree of instability within valley floor glacial sediments is found in the apex of meander bends where banks are oversteepened and failed material is actively removed by fluvial erosion. The predicted depth of tension in a vertical bank from Rankine Theory, 3.4 m, is in excellent agreement with the value of 3.5 m measured in the field on the Middle Fork of the Nooksack River. In a predictive sense, those sites situated above the saturated threshold would be most susceptible to changes in the hydrologic response of a watershed induced by land management activities.

CHUCKANUT FORMATION

Material Description

The Eocene Chuckanut Formation, a 6000 m thick package of subaerially deposited sediments, is well suited for this study because of its regional extent and propensity towards large-scale landsliding (Figures 3-2 and 3-8). Classified as one of the thickest fluvial sequences in North America (Johnson, 1982; Johnson, 1984), this interbedded, well-cemented sandstone, extends from the low-relief topography of the San Juan Islands and

Bellingham, Washington east to the high-relief mountains just west of Mt. Baker in the Cascade Range.

This study focused on a portion of the largest outcrop belt (60 km x 20 km) extending from the San Juan Islands into the foothills of the northern Cascades. Representing the remnants of an extensive **fluvial** system in western Washington, the Chuckanut Formation consists chiefly of alternating intervals of coarse-grained and **fine-grained** alluvial strata. The dominant coarse-grained lithology is sandstone with some conglomerate and conglomeratic sandstone. Sandstones are predominately arkosic, **cross-bedded** or laminated, and occur as beds generally less than 1m thick. The fine-grained intervals are dominated by massive or laminated siltstone and mudstone. Coal and black shale are also common, forming thin lenticular beds typically 5 to 50 cm thick. These terrigenous sediments were deposited unconformably upon pre-Tertiary rocks, such as the Darrington Phyllite, and across thrust faults. Subsequent Tertiary deformation compressed the sequence into broad, northwest-plunging folds, producing high-angle faults such as the Straight Creek Fault (Brown et al., 1987). As a **result**, the dip of the rock is highly variable. Glaciation and steep slopes has resulted in only a thin regolith on most slopes.

Failure Character and Location

The spatial density and size of deep-seated rockslides within the Chuckanut Formation increases eastward with relative relief toward the Cascade crest. No large **deep-seated** landslides were identified in the San Juan Islands, presumably because of insignificant topographic development. The bulk of the landslides are located in the higher relief terrain east of 122° 15' latitude (Figure 3-8). Translational rockslides are the characteristic type of landslide, the largest of which is located on the west side of Van Zandt Dike covering over 9 km² in surface area. The failed mass extends farther than 2 km from the mountain front across the **valley** floor and the **hummocky** deposit is punctuated by numerous swamps and **small** lakes (Figure 3-8). The largest rockslide on Slide Mountain, in the northeastern portion of the study area, covers about 3 km². The toe of this slide appears to have crossed the North Fork of the **Nooksack** River because large sandstone blocks are found across and down river from the slide (Moen, 1962).

The rockslide with the youngest appearance, termed Big Slump Mtn., is located at the confluence of Clearwater Creek with the Middle Fork of the **Nooksack** River (Figures 3-2, 3-9, and 3-10). The exact ages of landslides in this area is unknown but are constrained by the timing of glacial retreat. Ages greater than 13,000 yr B.P. are excluded because loose, easily transported landslide debris would presumably have been removed by the continental ice sheet. Studies of rockslides in Norway by **Bjerrum** and **Jørstad** (1968) have indicated that deep-seated failures in rock occurred, "... a short time after the end of the last glacial period, when the glaciers had withdrawn and the sides of the valleys and fjords were deprived of most of their lateral support" It is thought that steeper rock slopes not experiencing failure immediately after glacial retreat may undergo a gradual degradation of strength over time becoming susceptible to failure at a later date.

Mountain-front rockslides express common morphologic signatures. The resulting scars in the landscape are typically bowl-shaped, resembling a broad inverted "U" (Figure 3- 10). Topography in the source region high on the hillslope exhibits a concave form, At the base of the hillslope the translational movement of material produces a convex lobe protruding from the mountain front. Other features include streams along the landslide margins, neatly defining lateral boundaries and discontinuous irregular **fluvial** networks on the landslide body. In contrast, **fluvial** land sculpting typically produces a dendritic network constrained within a tear-drop shaped catchment.

Within landslide bodies, bedding orientations tend to be random. Coherent blocks up to 100's of meters in volume float in a sea of churned matrix, ostensibly the result of violent downslope transport. The chaotic nature of many landslide masses in conjunction with their long distance **runouts** (> 2 km) are thought to indicate high velocity, catastrophic movement. Furthermore, failure may have occurred in rapid surges because deposits often reveal a series of concentric ridges along the longitudinal axis of the rockslide.

The vast majority of deep-seated rockslides occur on hillslopes inclined at 15° to 35°. Steep gradient topography typically lacks deep-seated slides. Slopes greater than 35° usually generate shallow, fast moving landslides such as debris flows and rock fails. Much of the landscape, however, is composed of topography with shallow to moderate gradients rather than the steeper debris flow realm.

Method of Analysis

Similar to the glacial sediments, the Chuckanut Formation is composed of alternate strata with different strengths. It is particularly well suited to a regional analysis because the weaker layers, commonly the cause of instability, are unsuitable for rigorous laboratory testing. In addition, the influence of bedding planes and jointing cannot be readily estimated from laboratory tests.

Previous landslide identification by Fiksdal and Brunengo (1981) was supplemented with stereoscopic mapping of deep-seated landslides from color infrared aerial photographs onto 1:24,000 scale topographic maps. Aerial photograph mapping was completed for 585 km² of Chuckanut Formation outcrop bodies over a total area of almost 800 km², including alluvial lowlands and Quaternary glacial deposits. Included in this area are the outcrop bodies covered in Figure 3-8 as well as the San Juan Islands of Patos, Sucia, Matia, and Lummi. A total of 34 deep-seated rockslides were identified, averaging about one deep-seated landslide per 17 km² of exposed Chuckanut Formation.

Reliefs and horizontal base lengths from ridgecrest to the break-in-slope at the valley floor were measured from U.S. Geological Survey 7.5 minute quadrangle maps. When measuring profiles of landslide sites, the approximate mountain front location was projected into the failed mass to account for the pre-failure location of the break in slope. Rockslides of the Chuckanut Formation characteristically initiate within the hillslope face (Figure 3-1 and 3-10) and are subsequently modeled with the equations of Appendix C corresponding to a tension crack in the slope face. Structural geologic data used to classify hillslope orientation with respect to geologic structure was obtained from Vonheeder (1975), Johnson (1982), and personal field measurements.

Back-Calculated Strength Properties

Of the 204 measured profiles extending from ridgecrest to valley floor in areas underlain by the Chuckanut Formation, 34 represent deep-seated rockslides. A plot of slope vs. relief for these transects reveals an arcuate upper bound (Figure 3-11). This limit to topographic development, assumed to be the maximum attainable based on the widespread instability of the area, constrains back-calculated strength parameters.

Geotechnical properties implied by fitting a threshold curve to the upper limit of the observed data ($\phi=21^\circ$, $c=150$ kPa with $\gamma=25$ kN/m³) are interpreted to represent long-term effective values for the entire Chuckanut Formation in a dry state. For comparison, in *situ* sheargraph measurements of weak, fine-grained strata of siltstone and shale at a site near Bellingham produced strength values of $\phi=27^\circ$ and $c=26$ kPa.

Pore pressure distributions were approximated by the extreme conditions of dry hillslopes and complete saturation. Even under the assumption of fully saturated conditions, many landslide sites lie below the predicted threshold of instability (Figure 3-11). This conundrum reflects treatment of the **entire** formation as one entity without considering the destabilizing effects of geologic structure. Separation of transects into three structural categories of anti-dip slopes, dip slopes, and slopes striking parallel to fold axes results in a segregation of the data. Figure 3-12a, depicting only those transects along anti-dip slopes, reveals that anti-dip slopes control the maximum topographic development attained by the formation as a whole with threshold strength values of $\phi = 21^\circ$, $c = 150$ kPa. In contrast, the subset of transects along dip slopes define lower threshold strength values of $\phi=17^\circ$, $c=120$ kPa (Figure 3-12b). The remaining sites, representing slopes striking parallel to fold axes, are farther depressed from the dip slope topographic development limit, reflecting even lower strength values (not shown). Plots of base length vs. relief for anti-dip and dip slopes reveal a positive correlation between the width and relative relief of mountains (Figure 3-13). As discussed by Ahnert (1984), high relief mountain ranges also **have** great widths. Furthermore, the distribution of sites within Figure 3-13 implies that the larger, higher-relief slopes have lower strengths. This is inferred by the fact that with increasing hillslope size the location of sites fall progressively farther from the threshold envelope. In addition, all measured dip slopes greater than 700 m of relief have failed (Figure 3-13b).

Buttressing from Glacial Deposits

The present stability of select hillslopes in Figure 3-11 greater than 750 m in relief is partially explained by the buttressing of lower valley **walls** with **glacio-fluvial** deposits. In the high-relief **Nooksack** River basin, much of the valley floor and lower portions of the adjacent hillslopes are covered with glacial deposits up to 150 m thick. This added mass decreases the overall **hillslope** gradient and provides a downward directed force on the

lower portion of the bedrock hillslope, thus increasing the relative stability of the underlying rock. While only 37% of the recognized landslide sites above 750 m are buttressed with glacial sediments, 80% of the currently stable sites have thick benches of glacial sediments buttressing their lower slopes. In addition, modeling carried out with the method-of-slices computer program "XSTABL" version 3.22 (1990) suggests that the presence of glacial valley fills increases the relative factor of safety by about 30%. Therefore, the presence of glacial sediment buttresses may allow higher ridges to be stable than would otherwise be possible.

In summary, structural control greatly influences local topographic development and the degree of instability within the Chuckanut Formation. Dip slopes lie significantly below the threshold of maximum topographic development deformed by anti-dip slopes. Furthermore, buttressing of mountain fronts by glacial benches may increase the relative factor of safety of higher ridges by as much as 30%.

DARRINGTON PHYLLITE

Material Description

The **Cretaceous** Danington Phyllite lies unconformably below the Eocene Chuckanut Formation. Resulting from regional metamorphism, this rock is predominantly a black, graphitic, chiefly **quartzose** to carbonaceous phyllite derived from a siliceous **mudstone** (Brown et al., 1987). It is very finely crystalline, strongly foliated, and commonly folded and **lineated**.

Failure Character and Location

Deep-seated landslides within the Dartington Phyllite appear as both mountain-front and inner-gorge landslides, which are by far the more numerous variety. Inner-gorge channel banks of the Middle Fork of the **Nooksack** River, primarily downstream of the diversion dam (Figure 3-2), express widespread instability. Figure 3-14 shows a typical inner-gorge failure located adjacent to the channel.

Method of Analysis

Mountain-scale, deep-seated rockslides were mapped from stereoscopic aerial photograph and 7.5 minute quadrangle analysis. Inner-gorge landslides were identified through both field observations and aerial photograph analysis. Relief and gradient of the inner gorges were field surveyed with tape, stadia rod, and transit compass. Because field observations indicated that the degree of weathering strongly influences strength, relatively unweathered rock comprising high relief mountain fronts was distinguished from moderate to highly weathered rock of the inner gorges.

Relief Development

Figure 3-15 depicts the topographic development of weathered phyllite in the inner gorge of the Middle Fork of the **Nooksack** River near the diversion dam and relatively unweathered rock **upslope** from the inner gorge. Because of the relatively small, restricted data set (15 unweathered rock and 29 weathered rock sites) and great differences in rock strength due to weathering, material properties were not back-calculated.

Effect of Weathering

The Danington Phyllite exhibits varying degrees of strength depending on its extent of weathering. Whereas analysis of the strongly bedded Chuckanut Formation revealed that stability is highly dependent on geologic structure, examination of slopes underlain by **Darrington** Phyllite suggests that the degree of weathering dramatically alters material strength. Rock exposed in the inner gorge is subjected to enhanced fracture intensity through mechanical weathering induced by the local topographic stress field (Miller, 1993). Greater fracture density allows for increased hydraulic permeability and intensified chemical weathering. In addition, rock within valley floors such as an inner gorge are subject to focusing of groundwater flow (Freeze and **Cherry**, 1979). Consequently, rock comprising the inner gorge fails at much lower heights, for a given hillslope gradient, than the same unweathered rock (Figure 3-15a) above the groundwater flow field. Thus, rock strength predictably differs through the landscape with inner gorges identified as sites possessing weathered, weak rock. In *situ* sheargraph measurements of an outcrop of weathered Danington Phyllite produced strength values of $\phi=39^\circ$ and $c=7$ kPa.

In summary, the extent of weathering influences local topographic development and slope stability within the Danington Phyllite. Certain predictable locations of the landscape, such as inner gorges, experience heightened strength degradation due to heightened chemical weathering, ground water focusing, and mechanical weathering arising from topographic stresses.

SANTA CRUZ MOUNTAINS STUDY AREA

Material Description

The Santa Cruz Mountains study area of central California (Figure 1-5) is comprised solely of relatively weak marine sandstones, mudstones, and shales. A sequence of seven lithologic units (the Butano Sandstone, San Lorenzo Formation, Santa Cruz Mudstone, Vaqueros Sandstone, Santa Margarita Sandstone, Monterey Formation, and Purisima Formation) ranging in age from Eocene to Pliocene (McLaughlin et al., 1988; Clark et al., 1989; Wagner et al., 1990; McLaughlin et al., 1991) was examined. Lithologies exposed in the mountainous area near the epicenter of the Loma Prieta earthquake (primarily Butano Sandstone, Vaqueros Sandstone, and Purisima Formation) are arkosic sandstones with interbeds of shale and mudstone. Lithologies exposed in coastal bluffs along Monterey Bay (primarily Santa Cruz Mudstone, Monterey Formation, and Purisima Formation) include: flat-lying, thickly bedded to massive, tuffaceous mudstone, siliceous organic mudstone, siltstone, and sandstone. The Purisima Formation is extensively jointed and susceptible to both topples and slumps (Sydnor et al., 1990).

Failure Character and Location

Widespread landsliding resulted from the $M_s 7.1$, 17 October 1989 Loma Prieta earthquake. The vast majority of the seismically induced failures were shallow translational slides, falls, and avalanches triggered by seismic accelerations. Landslides and other coseismic fissures destroyed or damaged hundreds of residential structures, a major state highway, and county and private roads (Spittler et al., 1990). Four strong-motion instrument stations located throughout the epicentral region recorded shaking intensity. The recorded range of free-field peak horizontal accelerations for both the mountainous

epicentral region and coastal bluffs is 0.47 g to 0.64 g (Boore et al., 1989; Shakal et al., 1990; Sydnor et al., 1990). The range of vertical ground motion was about 0.40 g to 0.66 g, with significant shaking lasting for 17 to 23 seconds (Sydnor et al., 1990).

Earthquake-induced landslides were most abundant adjacent to the surface trend of the San **Andreas** Fault northwest of the epicenter. Figure 3- 16 shows a deep-seated rockslide in this area along State Highway 17. Typically, though, only portions of individual landslide masses moved during the earthquake, with few catastrophic failures recognized. Extensional features such as headscarps were common with cracks exhibiting up to a meter of vertical displacement and 1.2 meters of horizontal extension (Griggs et al., 1991). Expression of compressional features such as bulging landslide toes were rare. In addition, many of the deep-seated landslides were **reactivations** of portions of ancient, large landslide complexes as mapped by Cooper-Clark and Associates (1975).

The modern **seacliff** forming the eastern boundary of Monterey Bay is but the latest of a series of Pleistocene seacliffs represented by a well-preserved flight of marine terraces (Bradley and Griggs, 1976). Modern seacliffs are the expression of a dynamic balance between surf erosion that steepens cliffs and landslides that reduce the gradient of cliffs. Along Monterey Bay, uplifted marine terraces of wave-cut bedrock platforms are overlain by 3 to 7 m of terrace deposits. The densest concentration of coastal bluff landslides resulting from the earthquake was located 9 to 20 km from the epicenter (Sydnor et al., 1990). Translational landslides on the coast were typically shallower than several meters in thickness and smaller than 30 m in width.

Method of Analysis

Landscape form and the location of earthquake-induced landslides were examined in the mountainous epicentral region as well as along coastal seacliffs adjacent to Monterey Bay. In the mountainous epicentral region landslides were identified by Weber and Nolan (1989), Spittler and Harp (1990), Spittler (1990), Griggs (1991), McLaughlin (1991), and Manson et al. (1992). The location of coastal failures are identified by the studies of Plant and Griggs (1990), Sydnor (1990), and Sitar (1991).

Measurements extending from ridgecrest to the break-in-slope at the valley floor, representing the relief and horizontal base length of hillslopes, were obtained from seven U.S. Geological Survey 7.5 minute quadrangles covering the epicentral area. A total of 82 landslide transects were identified from the above mentioned studies of landslides initiating in response to the Loma Prieta earthquake.

All earthquake-induced landslides were modeled with equations assuming that the upslope extent of landsliding is constrained within the hillslope face. This is not the case with seacliff failures where headscarps extend into the upper slope surface. These sites, however, compose only 25% of the total data set so all sites are considered in unison as failures initiating on the hillslope face. In addition, the difference in back-calculated properties originating from the assumption of headscarp location is relatively small.

Back-Calculated Strength Properties

Topographic development of the 82 landslide sites initiating in response to the Loma Prieta earthquake is depicted in Figure 3-17. The back-calculated threshold envelope yields strength values of $\phi=20^\circ$ and $c=60$ kPa with $\gamma=20$ kN/m³. Seacliff landslides plot above 35° in slope with less than 50 m of relief. Landsliding in mountainous areas typically have lower slopes, between 10° and 35°, with relief up to 300 m. Pore pressure distributions were approximated by the extreme conditions of dry hillslopes and complete saturation.

For comparison, triaxial and direct shear tests discussed in Keefer (1991) on the highly fractured, variably weathered, interbedded, and sheared sandstone, siltstone, and shale identified in failure planes of large, deep-seated landslides provide strength estimates for the material controlling failure. Samples of intact, unfractured, unshaped, and unweathered rock were not tested because it was thought that their strength did not control slope stability. Averaging the strength parameters reported on p. 365 of Keefer (1991) for fractured shale, the most common material in the samples, triaxial and direct shear tests produce mean values of $\phi = 20 \pm 6^\circ$, $c = 69 \pm 32$ kPa, with a range of dry unit weights of $\gamma=20$ to 23 kN/m³. Averaging strength values for all lithologies (shale, siltstone, sandstone, and clay) tested by Keefer (1991) (Table 5 p. 365) provides mean values of $\phi = 30 \pm 14^\circ$, $c = 69 \pm 32$ kPa, with a range of dry unit weights of $\gamma= 19$ to 26 kN/m³. It

is believed that back-calculated ($\phi=20^\circ$, $c=60$ kPa) and laboratory derived strength parameters for the most common material, shale, ($\phi=20^\circ$, $c=69$ kPa) are in such close agreement because both approaches characterize the nature of the weak portions of hillslopes controlling rock mass strength.

BACK-CALCULATED AND LABORATORY-DERIVED STRENGTH PROPERTIES

Tables 3-1 and 3-2 list strength parameters back-calculated from methods adopted in this study, values derived from *in situ* sheargraph measurements, and laboratory experiments. Consolidated material strengths are reported in Table 3- 1. Back-calculated parameters for the Santa Cruz Mountains are quite similar to triaxial and direct shear tests reported by Keefer (1991). This correlation independently confirms the validity of the back-calculation approach adopted in this study. Unconsolidated material strengths are reported in Table 3-2. Back-calculated strength values for glacial sediments are in close agreement with values measured on *in situ* outwash sands with a sheargraph. Thus, strength parameters back-calculated from a process geomorphology approach on the limits to topographic development match those obtained from experiments on discontinuous, *in situ* material. Strength values obtained through back-calculation, though, are lower than those generated by typical laboratory experiments on intact rock. It is believed that this apparent decrease in strength, especially for cohesion, stems from strength characterization integrating great spatial and temporal scales. Further discussion of the influences decreasing regional strength parameters is presented in Chapter 6.

Failure envelopes, representing the relationship between the shear stress required to cause failure and the normal stress acting on a potential failure plane, are plotted in Figure 3-18. Failure envelopes for the Chuckanut Formation (both anti-dip and dip slopes), glacial deposits, and lithologies of the Santa Cruz Mountains were defined by the Coulomb equation:

$$\tau = c + \sigma \tan \phi \quad (3-2)$$

Back-calculated material properties used to define the failure envelopes are reported in Tables 3- 1 and 3-2.

In summary, the approach adopted here predicts a limit to topographic development defined by the topographic attributes of stable and post-failure sites throughout a landscape. In general, back-calculated strength values obtained by this method are lower than traditional laboratory analysis. It is believed that the influences of structure, bedding, and weathering all decrease predicted instability. Examination of Figures 3-6, 3-11, 3-12, 3-13, 3-15, and 3-17 reveals that most landslides plot below the LTD. Alternatively, stable sites often plot adjacent to the LTD at the greatest topographic development. This apparent discrepancy is thought to arise, at least partially, from spatial variations in rock mass strength. Variations in rock mass strength focus landsliding where strengths are lower than adjacent areas where material strength is sufficient to support its degree of topographic development. Chapter 4 defines rock mass strength, causes for its spatial variation, and its influence on deep-seated landsliding.

Figure 3-1. Schematic cross section of landscape with flat-topped glacial deposits draped over bedrock. Inner gorge in valley bottom shows characteristic break-in-slope of valley wall profile. Two scales of deep-seated landslides are recognized: bedrock mountain-front landslides and smaller inner-gorge landslides in weathered bedrock and Quaternary glacial sediments.

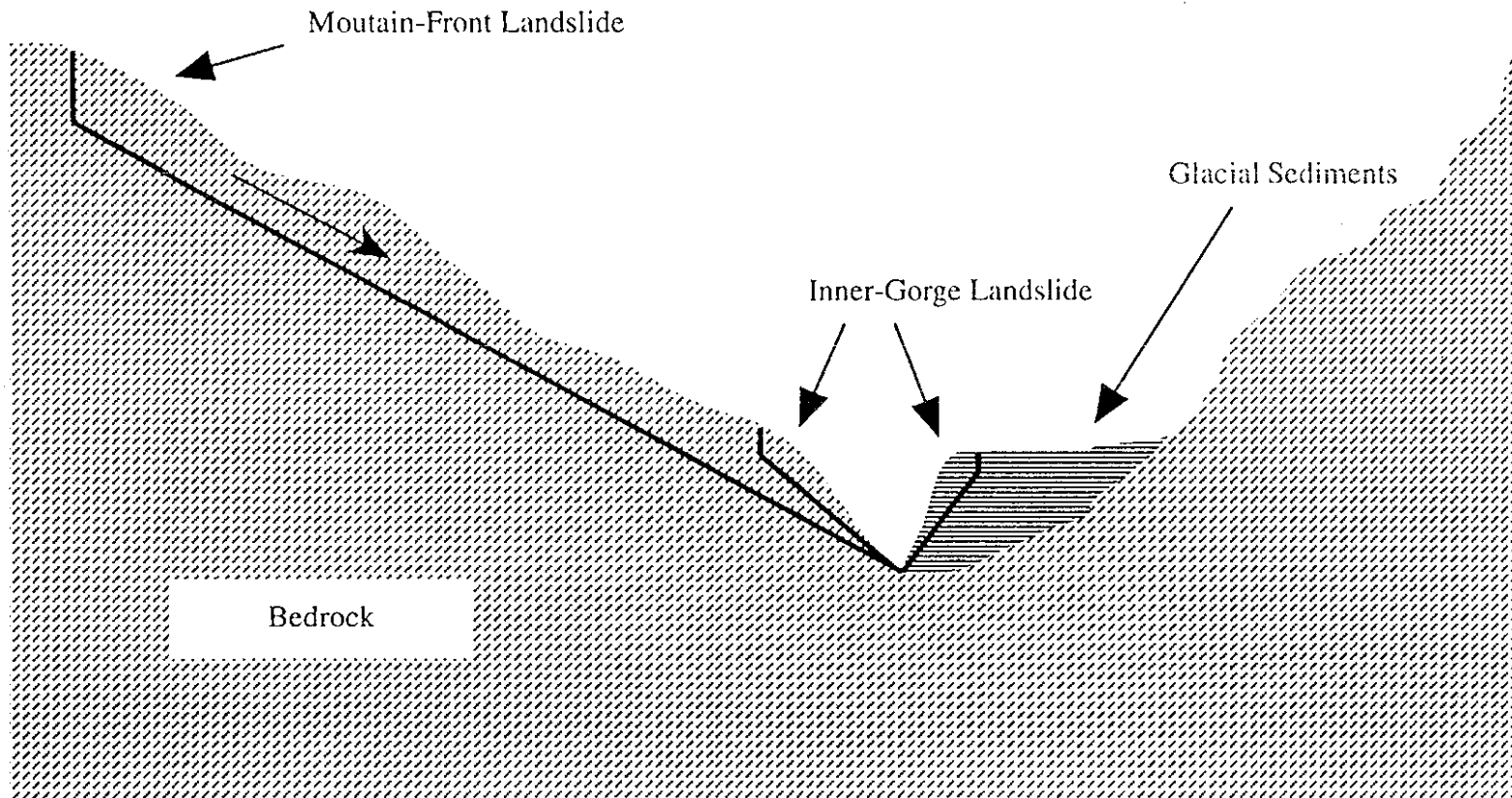


Figure 3-2. Excerpt from U.S. Geological Survey Canyon Lake 7.5 minute quadrangle showing locations of the Nooksack River and Clearwater Creek as well as mountain-front landslides in Chuckanut Formation (outlined in black with white fill). Inner-gorge landslides are depicted by a stippled pattern for the Darrington Phyllite and by diagonal lines for Quaternary glacial sediments.

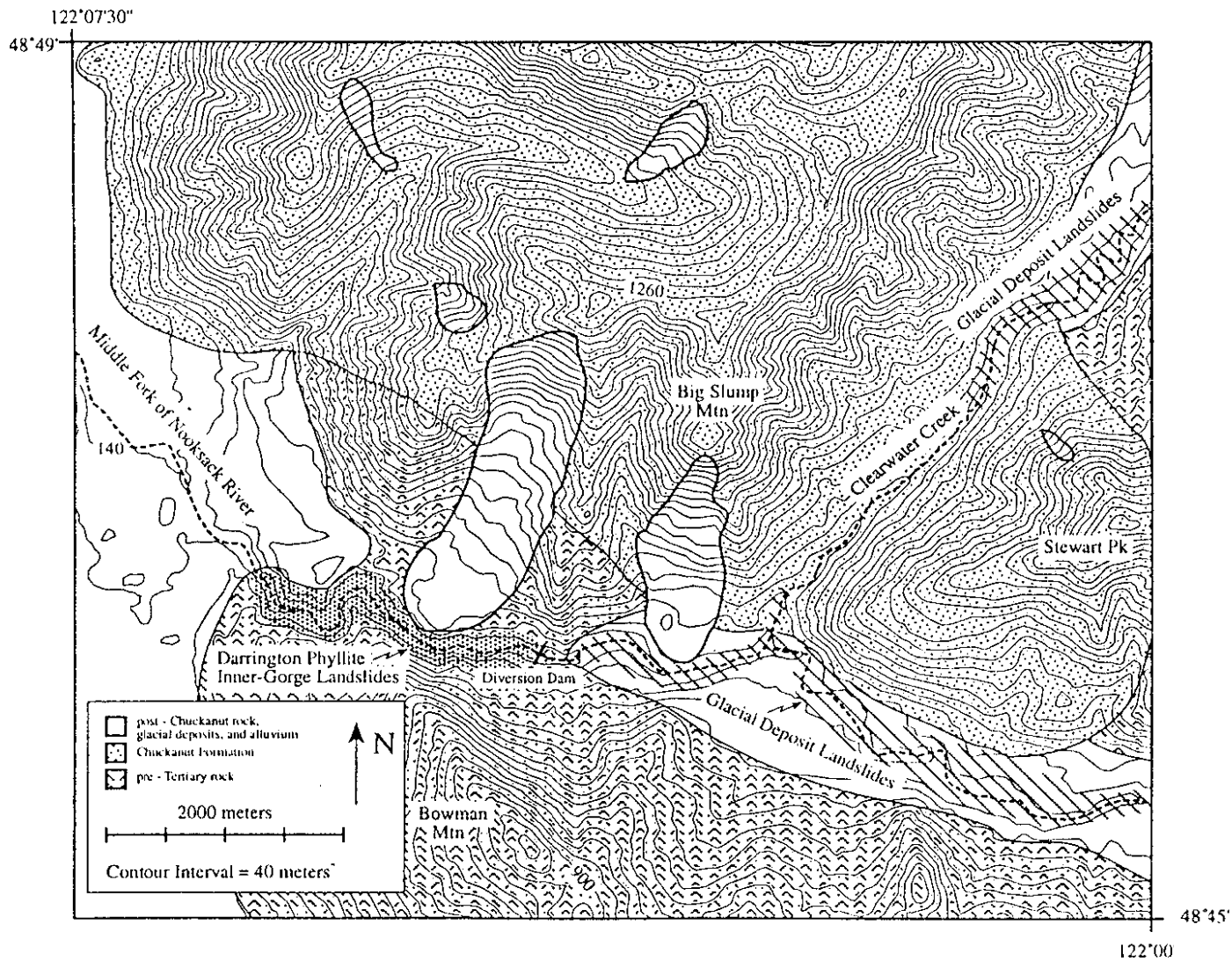


Figure 3-3. Photograph of two active slump failures located in the apex of meander bends on Clearwater Creek. View is to southeast.

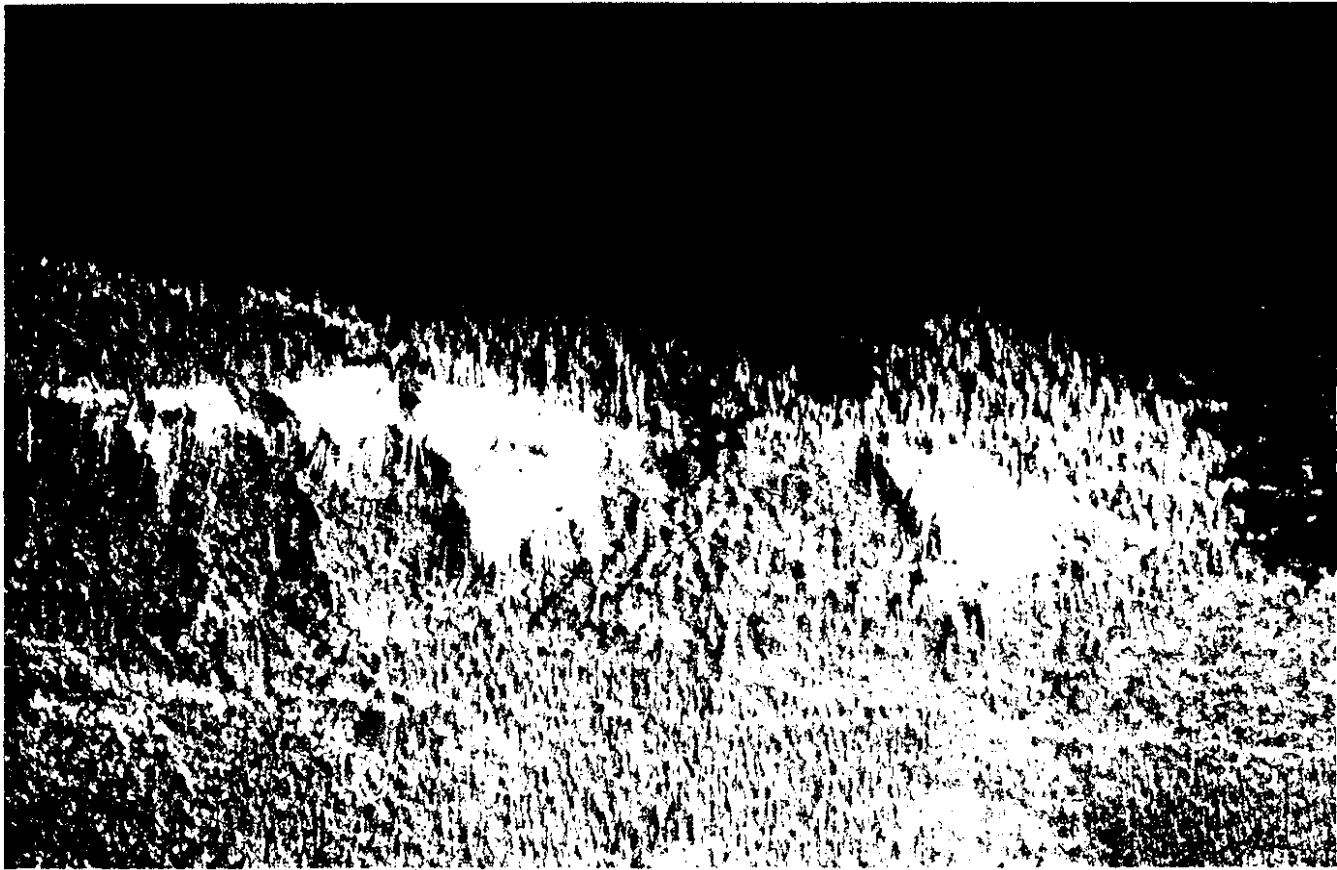


Figure 3-4. Photograph of exposed channel bank (inferred topple) on the Middle Fork of the Nooksack River. Well developed tension cracks, located approximately 1 m away from cliff face with about 10 cm of extension, extended parallel to exposed bank. Stadia rod is 6 m. View is to west.



Figure 3-5. Photograph of back-rotated slump block on Clearwater Creek. Tree tops are back-rotated toward headscarp and the majority of the failure block has been removed by fluvial erosion. View is to southwest. This site also appears as the right slump of Figure 3-3.



Figure 3-6. a. Transects for Quaternary glacio-fluvial deposits surveyed with hand level, stadia rod, and tape plotted with respect to gradient and relief. Values reported to right of thresholds refer to friction angle, $\phi = 29^\circ$ and cohesion, $c = 20$ kPa, i.e. (ϕ in degrees, c in kPa). Thresholds for both dry and completely saturated conditions are shown.

b. Transects for glacial deposits plotted with respect to topographic attributes of base length and relief.

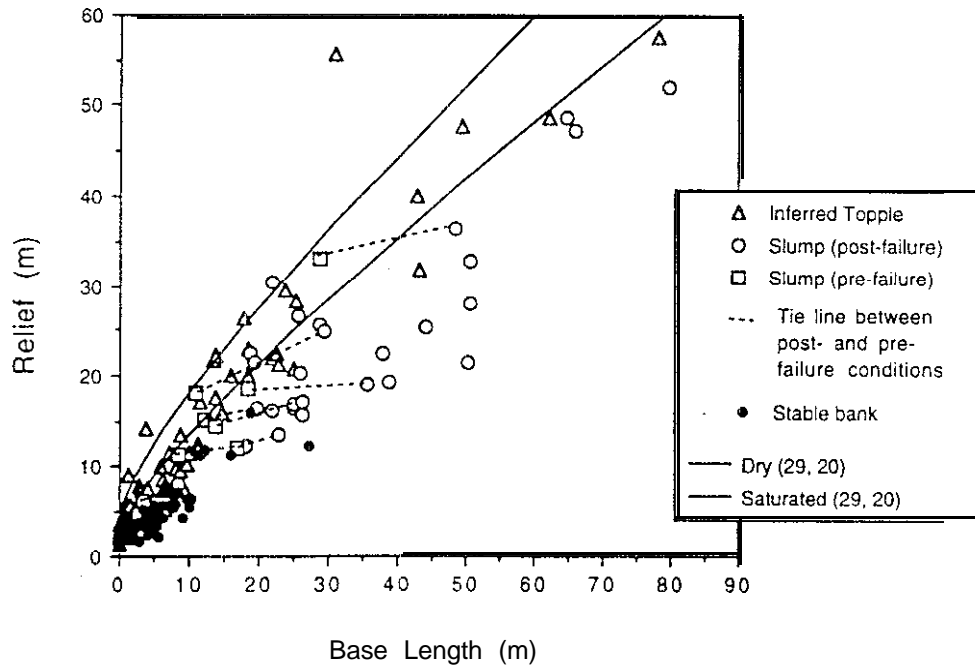
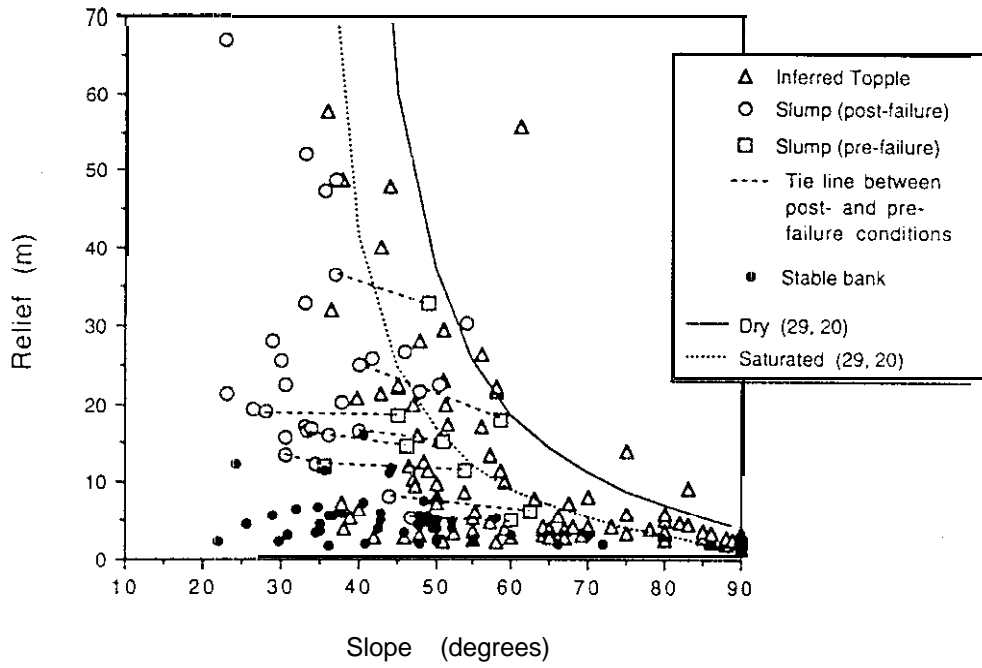


Figure 3-7. Schematic interpretation of Figure 3-6a showing spatial distribution of hillslope processes in the context of topographic development. Sites located above the saturated threshold may be highly susceptible to hydrologic changes within the watershed.

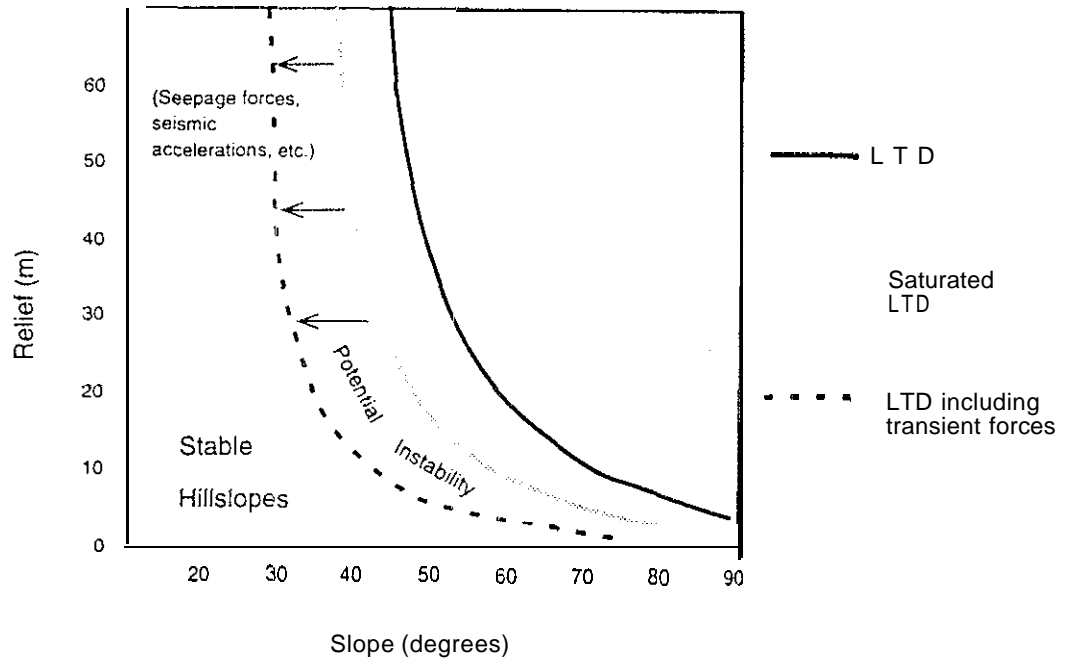
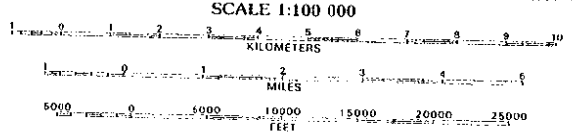
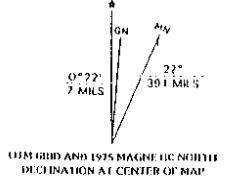
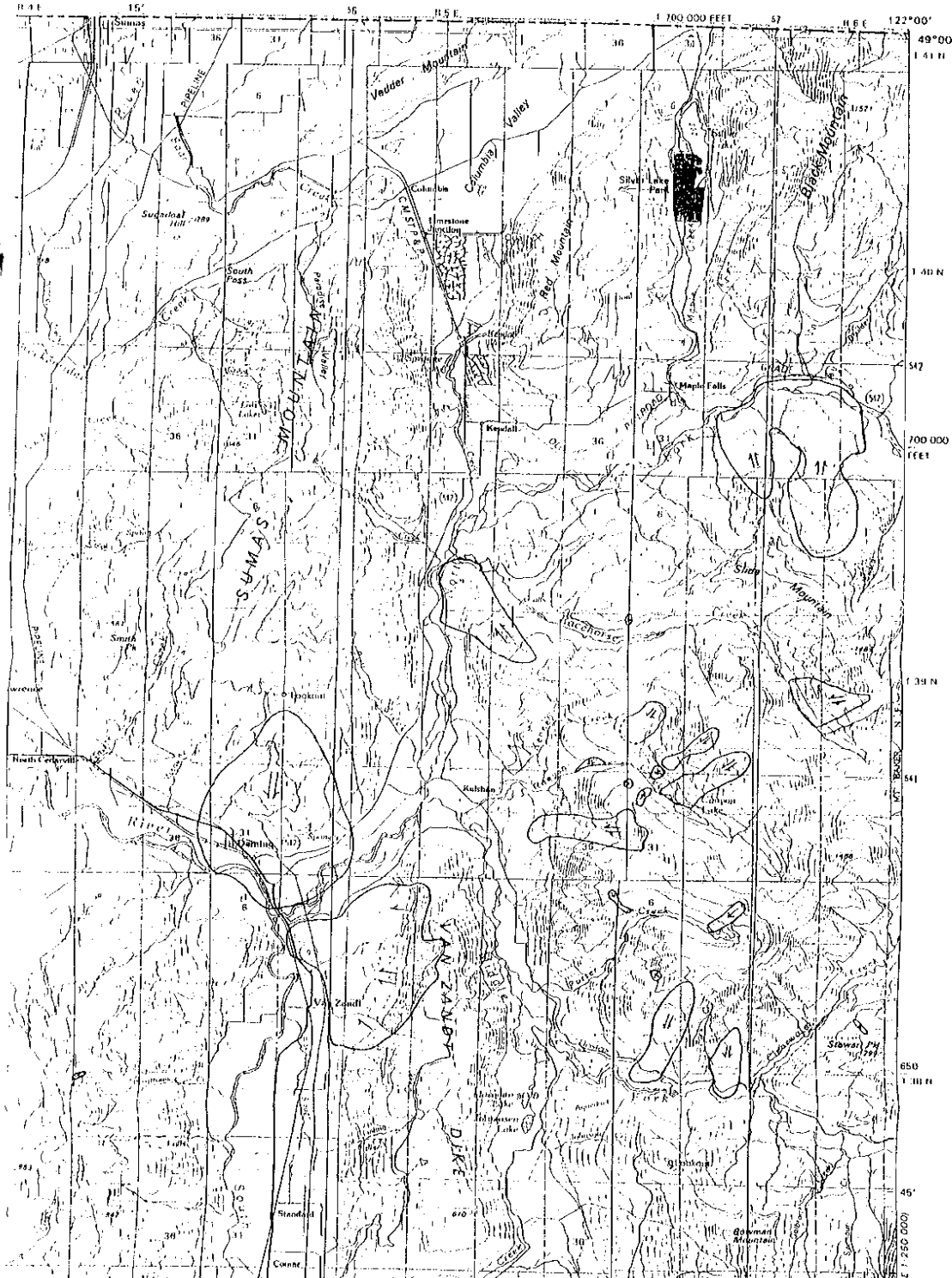


Figure 3-8. Map showing spatial distribution of Chuckanut Formation landslides within study area limits. Scale is 1:100,000. Arrows on landslides indicate approximate movement direction.

BELLINGHAM QUADRANGLE
 WASHINGTON
 1:100 000-SCALE SERIES (TOPOGRAPHIC)



CONTOUR INTERVAL 50 METERS
 WITH SUPPLEMENTARY CONTOURS AT 25-METER INTERVALS
 NATIONAL GEODETIC VERTICAL DATUM OF 1929

Figure 3-9. Photograph of Big Slump Mtn. showing a fresh exposed headscarp and internally deformed landslide hostly. View is to north. Photograph taken by Matthew Brunengo of the Washington State Department of Natural Resources.

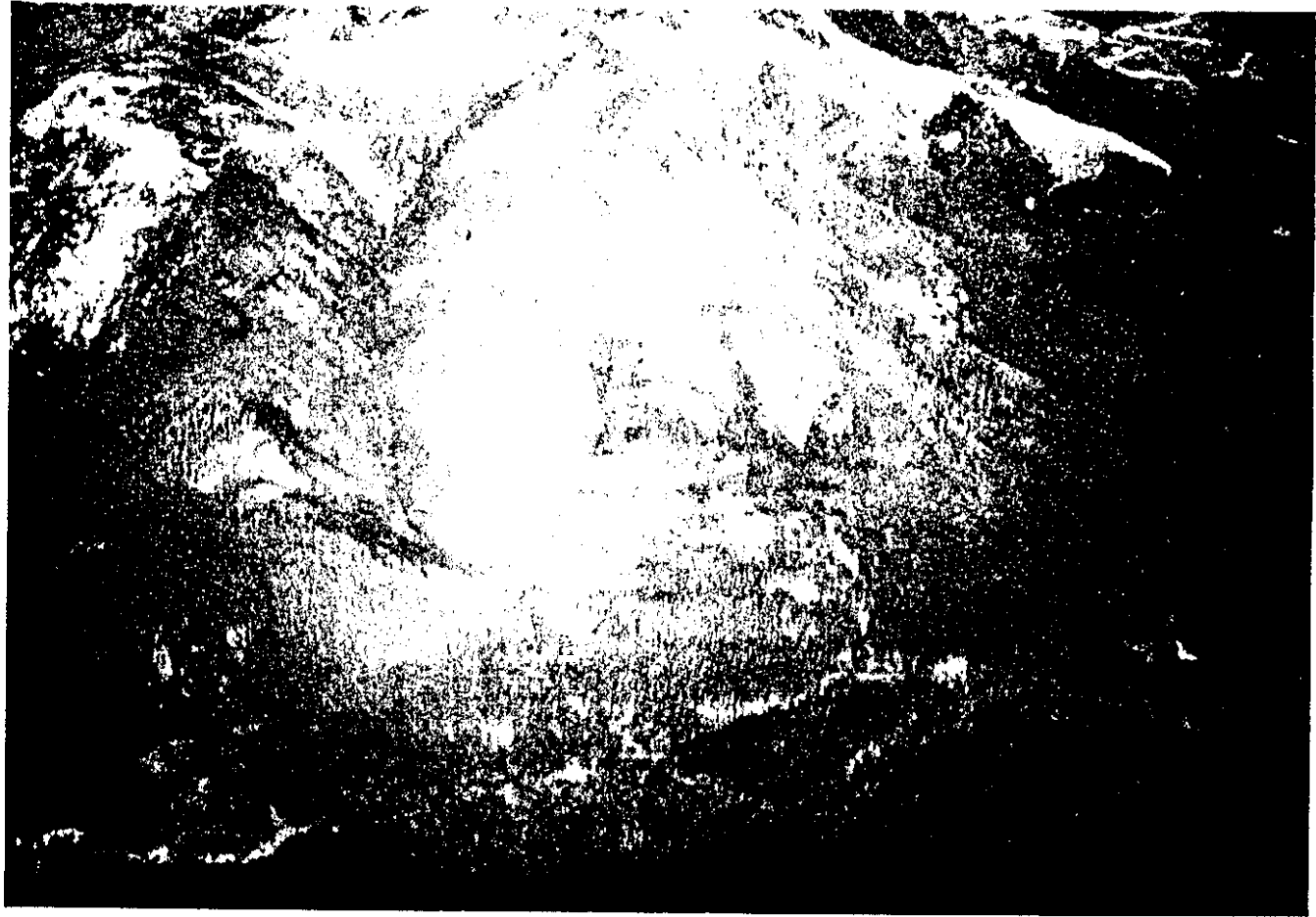


Figure 3-10. Photograph of older, larger failure just west of Big Slump Mtn. (in background). Failure morphology resembles an inverted "U". View is to east. Photograph taken by Matthew Brunengo of the Washington State Department of Natural Resources



Figure 3-11. All site transects (204 total) for the Chuckanut Formation plotted with respect to gradient and relief. Thresholds for both dry and completely saturated conditions are shown. Values reported to right of thresholds refer to friction angle, $\phi = 21^\circ$ and cohesion, $c = 150$ kPa.

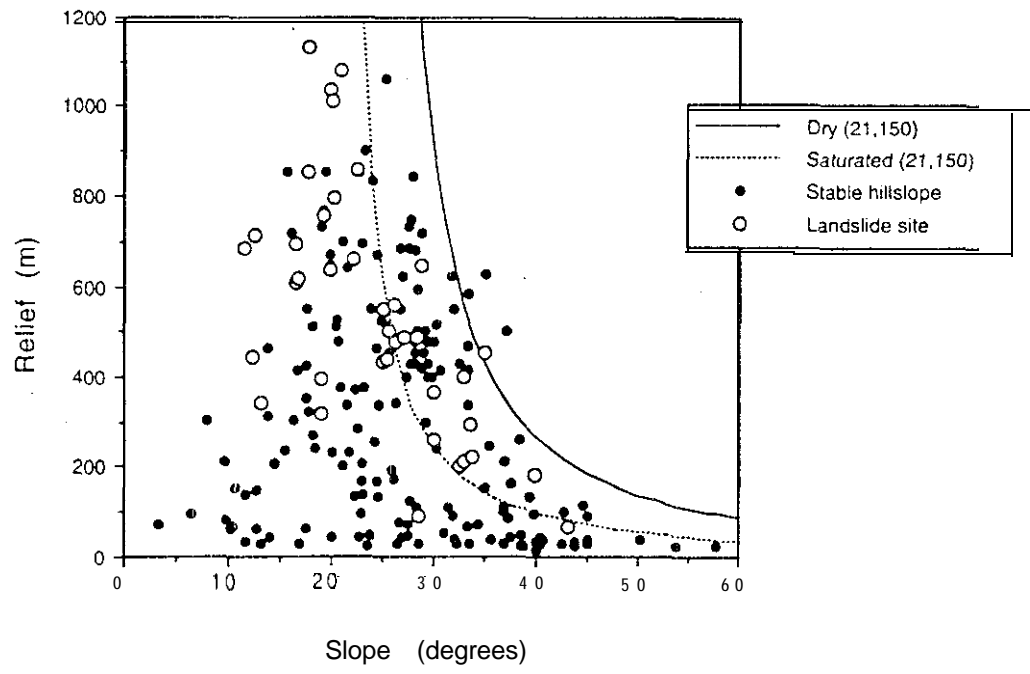


Figure 3-12. a. Anti-dip slope transects for the Chuckanut Formation plotted with respect to gradient and relief. Values reported to right of thresholds refer to friction angle, $\phi \approx 21^\circ$ and cohesion, $c = 150$ kPa.

b. Dip slope transects for the Chuckanut Formation plotted with respect to gradient and relief. Values reported to right of thresholds refer to friction angle, $\phi = 17^\circ$ and cohesion, $c = 120$ kPa.

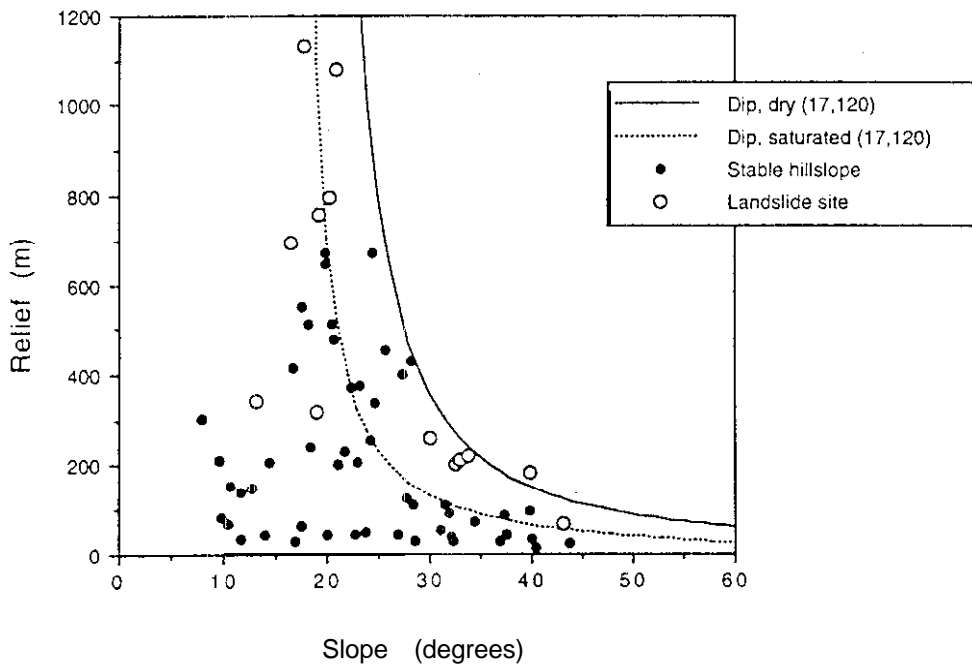
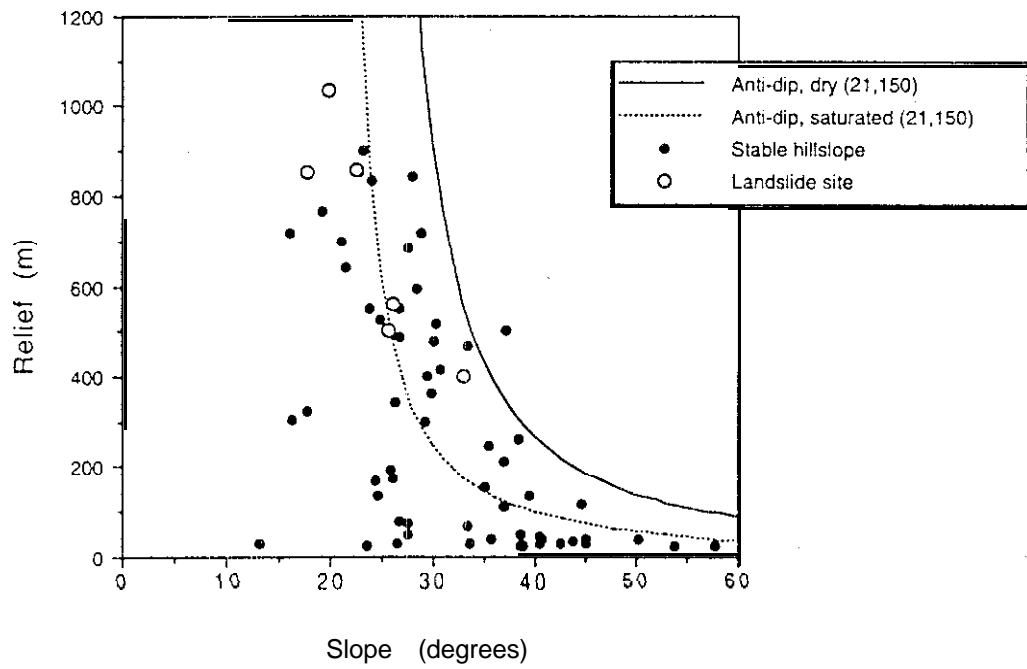


Figure 3-13. a. Anti-dip slope transects for the Chuckanut Formation plotted with respect to base length and relief. Values reported to right of thresholds refer to friction angle, $\phi = 21^\circ$ and cohesion, $c = 150$ kPa.

b. Dip slope transects for the Chuckanut Formation plotted with respect to base length and relief. All sites greater than 700 m relief are unstable. Values reported to right of thresholds refer to friction angle, $\phi = 17^\circ$ and cohesion, $c = 120$ kPa

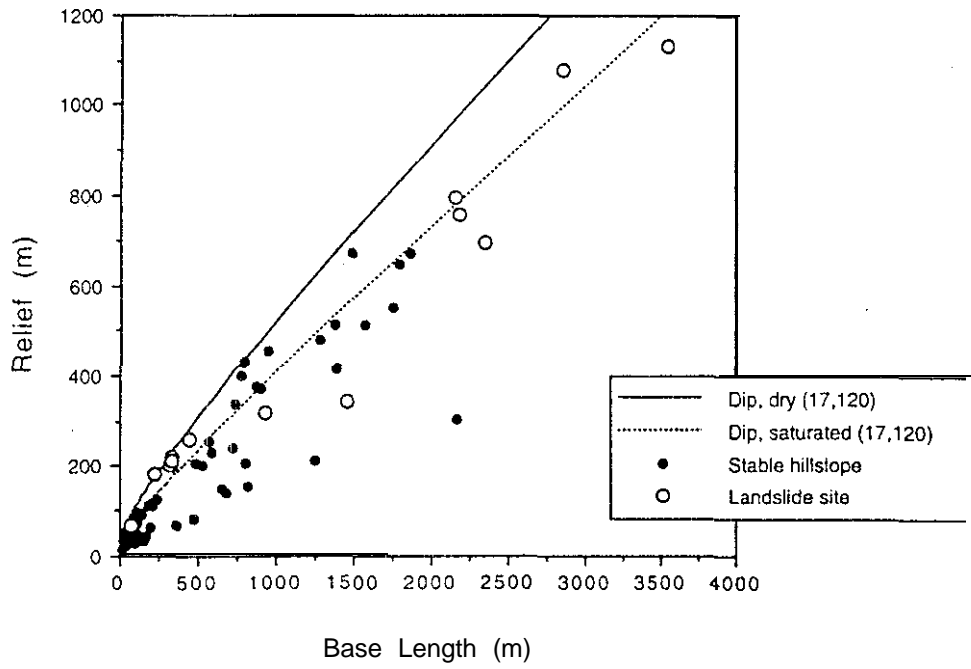
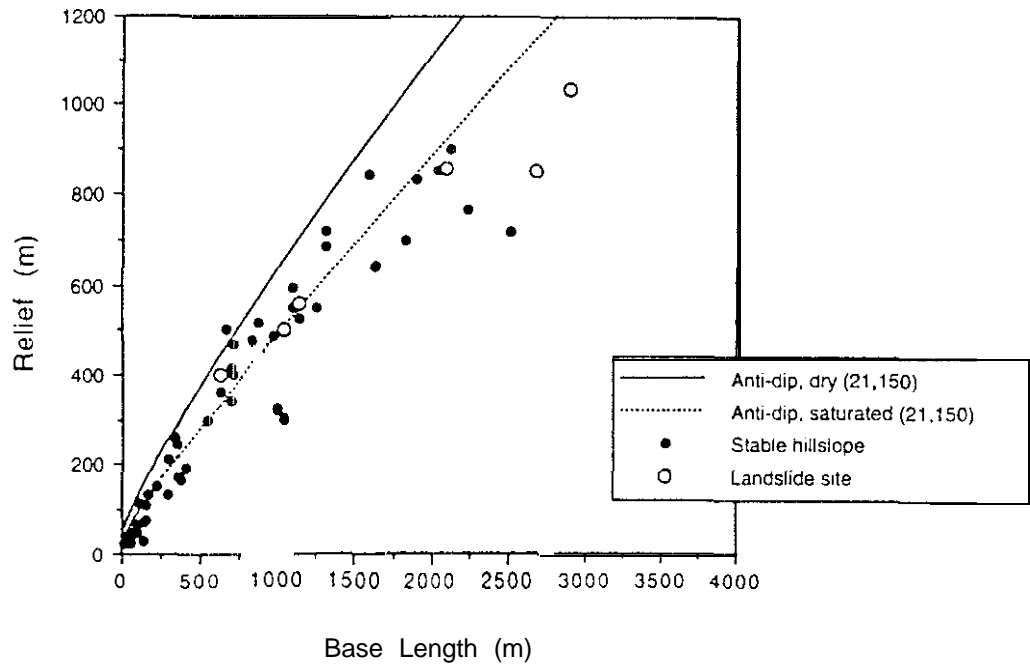


Figure 3-14. Photograph of inner-gorge landslide in weathered Darrington Phyllite along Middle Fork of Nooksack River



Figure 3-15. a. Transects for the Darrington Phyllite depicting both weathered and unweathered rock plotted with respect to gradient and relief. Dashed line, at 180 m relief, represents maximum relief attained by weathered phyllite.

b. Transects for the Darrington Phyllite depicting both weathered and unweathered rock plotted with respect to base length and relief.

Figure 3-1 6. Photograph of rockslide initiating during Loma Prieta earthquake in Santa Cruz Mountains. The rockslide blocked the northbound lanes of State Highway 17 for 33 days costing the California Department of Transportation \$ 1.8 million to repair.

Photograph taken by U.S. Geological Survey Staff.



Figure 3-17. a. Landslide sites (82 total) for marine sedimentary units of the Santa **Cruz** Mountains plotted with respect to gradient and relief. Thresholds for both dry and completely saturated conditions are shown. Values reported to right of thresholds refer to friction angle, $\phi = 20^\circ$ and cohesion, $c = 60$ kPa.

b. Landslide sites of the Santa **Cruz** Mountains plotted with respect to base length and relief. Values reported to right of thresholds refer to friction angle, $\phi = 20^\circ$ and cohesion, $c = 60$ kPa.

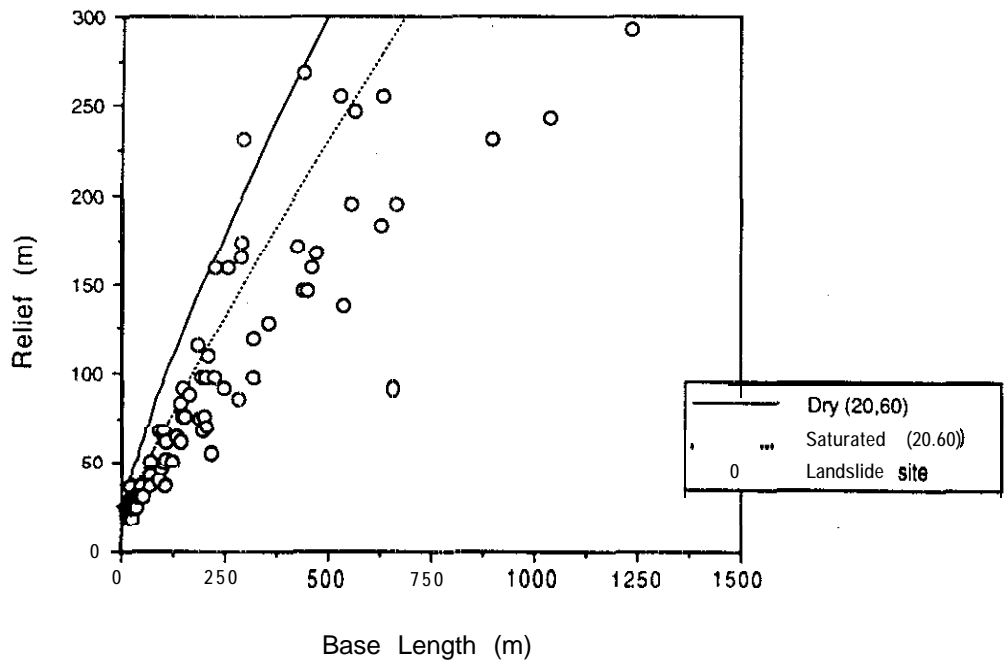
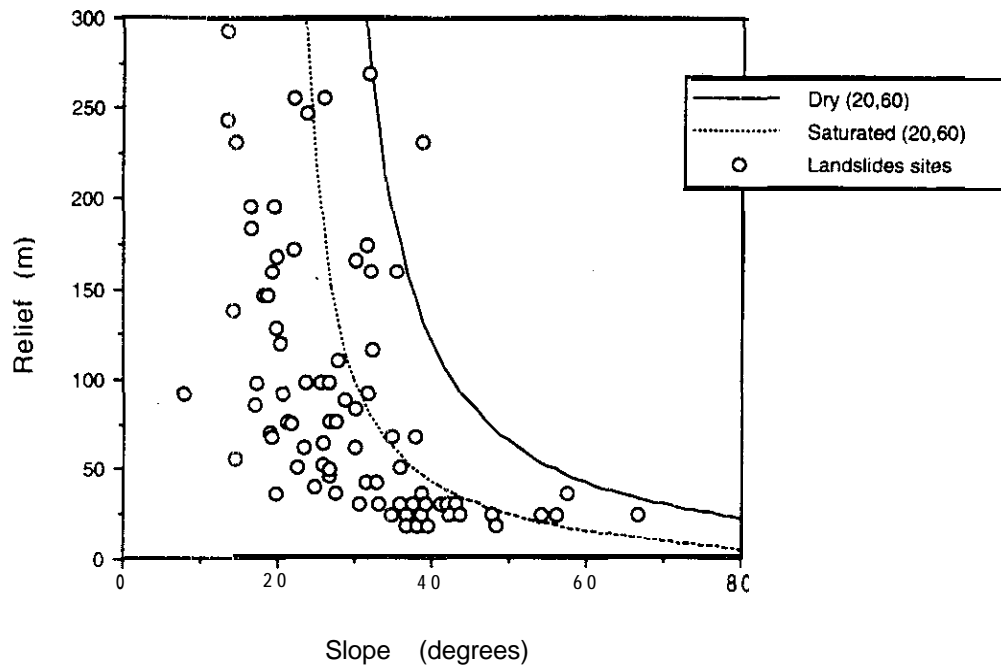


Figure 3- 18. Graphical representation of Coulomb equation for **Quaternary glacio-fluvial** deposits, anti-dip and dip slopes of the Chuckanut Formation, and sedimentary units of the Santa Cmz Mountains.

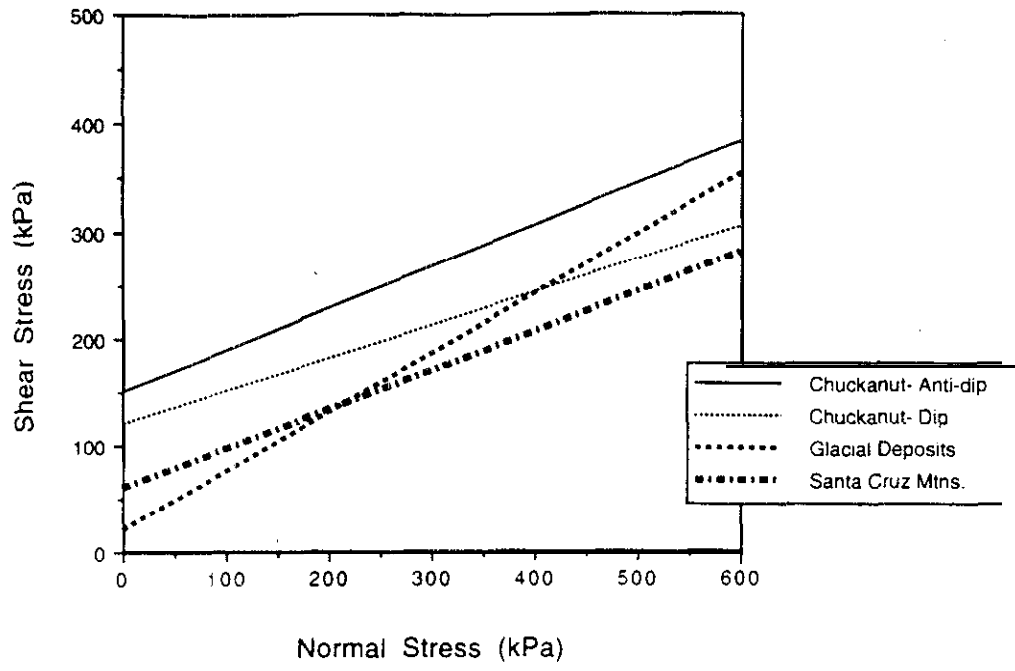


Table 3-1. Strength values for consolidated materials back-calculated from the empirical observations of topographic expression, measured *in situ* with sheargraph, and derived from **laboratory** experiments.

<u>Material</u>	<u>Friction Angle, ϕ (degrees)</u>	<u>Cohesion, (kPa)</u>	<u>Source</u>
Chuckanut Formation Anti-dip slope	21	150	LTD (this study)
Chuckanut Formation Dip slope	17	120	
Santa Cruz Mountains	20	60	
<hr/>			
Santa Cruz Mountains (shale)	20 ± 6	69 ± 32	Laboratory experiments (Keefer, 1991)
Santa Cruz Mountains (shale, siltstone, sandstone, and clay)	30 ± 14	69 ± 32	
Chuckanut Formation (siltstone/shale; characteristic of dip slope strength)	27	26	In situ sheargraph measurements
Weathered Darrington Phyllite	39	7	
<hr/>			
Hard sedimentary rock, ie. sandstone	35 - 45	10,000 - 30,000	Laboratory experiments
Soft sedimentary rock, ie. shale or coal	25 - 35	1,000 - 20,000	(Hoek and Bray, 1977)

Table 3-2. Strength values for unconsolidated materials back-calculated from the empirical observations of topographic expression, measured *in situ* with sheargraph, and derived from laboratory experiments.

<u>Material</u>	<u>Friction Angle, ϕ (degrees)</u>	<u>Cohesion, C (kPa)</u>	<u>Source</u>
Glacial Sediments	29	20	LTD (this study)

Glacial Sediments (sandy outwash)	36 ± 11	12 ± 9	<i>In situ</i> sheargraph measurements

Stiff glacial clay	30 - 32	70 - 150	Laboratory experiments (Hoek and Bray, 1977)
Soft, slightly organic clay	22 - 27	20 - 50	
Dense sand uniform size	32 - 40	0	

"... when you can measure what you are speaking about,
and express it in numbers, you know something about it..."

- Lord Kelvin (1824- 1907)

CHAPTER 4. ROCK MASS STRENGTH ASSESSMENT

PREVIOUS STUDIES

Structural features such as joints, faults, and bedding planes render *in situ* bedrock discontinuous. No single quantitative parameter fully describes either the strength of a rock mass or its relative resistance to weathering and mass wasting. Rather, simultaneous consideration of numerous parameters, with variable significance, are necessary to characterize the strength properties of a rock mass. A number of classification schemes have been used to assess the overall strength of a rock mass (Deere, 1963; Bieniawski, 1973; Piteau, 1973; **Barton** et al., 1974; Barton, 1978; Selby, 1980). Bieniawski (1989) provides a good overview and history of the many studies related to assessing the strength of rock masses. The vast majority of previous studies have focused on using rock mass strength classifications for engineering applications, particularly for the design of tunneling support in underground mining. More recently, Harp and Noble (1993) applied the technique of Barton et al. (1974) to estimate susceptibility of the Wasatch Front in Utah to seismically induced **rockfalls**.

Rock mass strength (RMS) classification schemes quantify strength according to parameters describing both the *in situ* rock material and the nature of the discontinuities. Rock material is the intact rock or the consolidated and cemented assemblage of mineral particles forming me intact blocks between discontinuities in the rock mass. The discontinuities separate intact blocks. The term discontinuity is used here to encompass all partings such as: joints, bedding planes, foliations, laminations, and faults that reduce the overall strength of a rock mass. In the context of slope stability, the importance of intact rock properties are overshadowed by discontinuity properties because rock mass strength decreases as the frequency of discontinuities increases (Teaaghi, 1962). Strength anisotropy, a variation of compressive strength according to the direction of me principal stress, is governed largely by the discontinuity properties.

DISCONTINUITIES AND THEIR INFLUENCE ON ROCK MASS STRENGTH

Joints, the most common discontinuity, are cracks or fractures in rock along which there has been little or no movement. The lack of displacement along joint planes and the fact that joints develop at all ages in the history of rocks makes these structures difficult to analyze (Price, 1966). No single mechanism such as thermal effects or stress conditions can be held responsible for the development of all joints. Barton (1973) provides a detailed discussion of shear strength along joints. In regions of complex geologic structure, such as the plunging folds of the Chuckanut Formation, the frequency of joint sets is partially set by the size and type of fold and the relative competence and thickness of the rock units.

Bedding planes, marking a change in sediment type or a depositional hiatus, also impose a prominent anisotropy on a rock mass. Within the same lithology, bedding planes are often tightly closed, retaining high cohesive strengths and frictional resistance. However, the Chuckanut Formation displays a wide range of lithologies with distinct planes of weakness at lithologic contacts. Contacts between massive sandstone and friable shale beds, for example, mark distinct changes in rock strength and appear to be planes of preferential weathering and water circulation. Along these contacts unloading and weathering should decrease both the cohesive strength and frictional resistance. As discontinuities widen, cohesion approaches zero and frictional resistance decreases, although the strength along a discontinuity may remain high where grains are still interlocking. Consideration of small-scale discontinuities, such as foliations and laminations, as well as the influence of major structural breaks such as faults are beyond the scope of this study.

SELBY'S RMS SCHEME AND MODIFICATIONS FOR APPLICATION TO DEEP-SEATED LANDSLIDING

Rock mass strength assessment is newly applied here in the context of deep-seated landsliding using a modified version of Selby's (1980) classification. Selby's (1980) classification scheme is based on engineering experience, but was altered for geomorphic applications. Seven weighted properties of the rock mass at the outcrop scale are used to quantify strength without expensive equipment or the need to obtain samples for laboratory analysis. The parameters include: relative strength of the intact rock, state of weathering,

spacing of the discontinuities, orientation of discontinuities with respect to the hillslope, width of the discontinuities, lateral or vertical pervasiveness of the discontinuities along with the degree of **infilling** within the discontinuity, and movement of water out of the rock mass (Table 4-1). Each parameter is weighted according to its relative importance and given a rating, R. The sum of all the parameter ratings provides the estimate of rock mass strength. Selby's application **of this** method was limited primarily to correlating rock mass strength with outcrop slope angle. For example, Selby (1980) reports a high positive correlation ($r = 0.88$) between the rock mass strength and outcrop slope with a standard error of 5.1" for the estimation of slope from knowledge of mass strength.

Application of Selby's scheme in the context of deep-seated landslide susceptibility required a few minor revisions. Except for the following modifications, all parameters were assessed based on the procedure outlined in Selby (1980). In order to evaluate the relative importance of joints, bedding planes, and lithologic variability each must be appropriately characterized in the modified classification scheme. Strength assessment at outcrops with sufficient exposure provides several RMS values; one for the influence of bedding planes and one for each well defined joint set. At outcrops exhibiting more than one lithology the intact rock strength was determined as a weighted average reflecting the bulk percentages and strengths of exposed lithologies. With this addition, the influence of lithology can be assessed in a formation such as the Chuckanut that commonly displays more than one lithology at the outcrop scale.

Uniaxial (unconfined) compressive strength is one of the generally accepted measures of intact rock strength. An *in situ* non-destructive test used to determine a surrogate for uniaxial compressive strength is the Schmidt hammer rebound test. Originally used to test concrete, it has been shown that the Schmidt hammer rebound test provides a reasonable correlation with large-scale *in situ* compressive strength (Sheorey et al., 1984). In lieu of a Schmidt hammer, the author qualitatively calibrated his own rock hammer/pick based on the relative rebound distance in response to a similar force impacting *in situ* rock material (Table 4-2). A similar force striking rocks with dramatically different compressive strengths results in either a resounding "ping" for coherent rock or a dull "thud" for weak rock. For further details of intact rock strength rating estimation, R, based on rock hammer and pick rebound characteristics refer to Table 4-2.

The spacing of bedding planes for each lithology must be taken into account because this modified scheme includes the influence of multiple lithologies at the outcrop scale. Similar to the incorporation of multiple intact rock strengths, each discontinuity spacing is classified according to Selby (1980) and then weighted according to the percentage of lithology exposed for a particular outcrop.

The other major modification to Selby's scheme is the classification of discontinuity orientations. The parameter representing discontinuity orientation with respect to the hillslope orientation is weighted heavily in the classification scheme, contributing a maximum of 20% of the available strength index. **Terzaghi** (1962) demonstrated that slope stability depends primarily on the orientation of the major persistent discontinuities with respect to the **hillslope**. In the absence of cohesion, the critical hillslope angle is controlled by the friction angle along the discontinuity in the direction of potential shear. Under conditions of uniaxial stress, the principal stress at the ground surface, σ_1 , is oriented parallel to and down the slope gradient (Figure 4-1a). Therefore, the most stable condition would occur when the discontinuity dip is normal to the topography, that is, the principal stress induced by topography, σ_1 , induces no shear stress on the discontinuity surface. In contrast to Selby's studies which concentrated in steep gradient ($> 30^\circ$), **rockfall** prone environments, application of the scheme in moderate gradient (15" to 40") deep-seated landslide prone environments requires alteration of the angular relationships of the discontinuity relative to the **hillslope** (Table 4-3). For example, the most unstable conditions occur when the hillslope gradient and the dip of the discontinuity are **sub-parallel**. In contrast to Selby's scheme which classifies planar joints dipping 30° to 80° out of the slope as the most unstable, this modified version assigns a planar discontinuity dipping out of the slope face at 10° to 40° , approximately parallel to the **hillslope** gradient, as the lowest strength configuration (Table 4-3).

The remaining parameters of Table 4-1: weathering, width of discontinuity, pervasiveness of discontinuity, and outflow of groundwater were applied in the manner suggested by Selby. As proposed by Moon (1984), the **five** divisions detailed in Table 4-1 should act only as a guide, allowing for interpolation of ratings between discreet categories. Descriptive parameters are continuous, not quantum properties. Therefore, to achieve finer scale resolution discretion **was** used to further subdivide parameter ratings, R, in Table 4-1.

Once the individual parameter ratings were summed, resulting in a rock mass strength value of the outcrop with a maximum value of 100, the value was extrapolated to the hillslope scale for sites without major structural features such as faults, folds smaller than the hillslope wavelength, or geologic contacts. In this manner, strength **values** are obtained that are intermediate in scale between laboratory derived values and the **back-calculated** properties detailed in Chapter 3.

APPLICATION TO CHUCKANUT FORMATION

The modified **rock** mass strength scheme was applied to the Chuckanut Formation to investigate features distinguishing stable hillslopes from landslide sites. Rock mass strength assessments were obtained for bedding planes and for each recognizable joint set at all outcrops. In addition, the manifestation of geologic structure on landscape form was portrayed with rock mass strength estimates and topographic profiles surveyed normal to the bedding strike. Measurements were taken in undisturbed, *in situ* rock masses and extrapolated to the **hillslope** scale to characterize the strength of mountains up to 900 m in relief. Outcrop strength assessments were carried out primarily on road-cut exposures over the region extending from Bellingham to just west of Mt. Baker. Efforts were concentrated in the landscape covered by the Bellingham South and Canyon Lake US. Geological Survey 7.5 minute quadrangles. Equipment required to determine rock mass strength was limited to: a metric tape measure, a rock hammer, and a transit compass. Outcrop dimensions varied greatly depending on field conditions and ranged from a few m² to 100's of m² with a median of **about 10 m²**. Field studies were completed during the summer and fall of 1992, times of characteristically low groundwater tables.

Outcrops of the Chuckanut Formation were examined in areas of both stable hillslopes and recognized landslide sites. RMS values characterizing landslide sites were measured within headscarps or just adjacent to landslide bodies to assure that outcrops analyzed were unaffected by landslide-related deformation. Sites were chosen in portions of the landscape used to define the limit to topographic development and back-calculated strength values described in Chapter 3. A similar plot, depicting the bedding plane influence on rock mass strength of select topographic transects, was generated from field study of **61** sites, including 17 landslides (Figure 4-2). Where multiple outcrop strengths were determined for one topographic transect, the values were averaged.

Figure 4-2 shows that bedding plane RMS values for landslide sites are consistently lower than for the neighboring stable hillslopes. If all valleys in a landscape were incised to the full topographic potential supportable by the maximum bedrock strength, the sites depicted in Figure 4-2 should be stratified such that rock mass strengths increase with relief for a given slope, or alternatively with slope for a given relief. Erosion, however, does not proceed such that the topographic potential of all the hillslopes is synchronously maximized. The resulting distribution of sites in Figure 4-2 may still be used in a predictive sense. For example, stable sites near the limit to topographic development that have relatively low RMS values may represent a high potential for instability. In addition, Figure 4-2 clearly demonstrates that RMS values pertaining to bedding planes are not positively correlated solely with hillslope gradient, as indicated by Selby's 1980 results for the gradient of steep bedrock hillslopes. Where the erosional history has not maximized topographic potential, the same RMS values may occur at different gradients.

Partitioning Figure 4-2 into the individual topographic components of relief and hillslope gradient demonstrates that all hillslopes with bedding plane RMS values greater than 69 are strong enough to retard deep-seated landsliding under the present erosional regime (Figure 4-3). In other words, all landslide sites have RMS values below 69. Two properties of the rock mass primarily control the RMS value: A) intact rock strength (low values usually reflect outcrops with a high proportion of shale) and/or B) unfavorable bedding plane orientation. For comparison, both bedding plane and joint set RMS values within landslide masses were typically 50 to 60. The strength decrease in response to landslide movement was due primarily to a dramatic increase in the concentration of discontinuities, the width of discontinuities, and the pervasiveness of discontinuities. Oversteepened outcrops within landslide bodies typically produce extremely low joint set RMS values (40 to 50), reflected by an abundance of rockfall failures identified on deep-seated landslide masses.

While it has been recognized that joint characteristics are crucial to rockfall susceptibility (Goodman and Bray, 1976; Harp and Noble, 1993), joint set concentrations and orientations were not useful for predicting susceptibility to deep-seated landsliding (Figure 4-4). In contrast to Figure 4-3 where the RMS values pertaining to bedding planes stratify landslide sites below 69, field analysis of 43 sites, including 11 landslides, reveals

that the primary joint set RMS values show no correlation with stability. Apparently, bedding plane orientation with respect to the hillslope orientation serves as the primary control on deep-seated landslide susceptibility within the Chuckanut Formation.

Importance of Discontinuity and Hillslope Orientation

Analysis of both bedding planes and joint sets within the Chuckanut Formation indicates that of the seven variables detailed in Table 4-1, discontinuity orientation with respect to the **hillslope** orientation shows the highest degree of variance and essentially controls the RMS value. Proper evaluation of the influence of the underlying geologic structure on stability requires determining the apparent dip of the discontinuity with respect to the topography by rotating the strike of the discontinuity into the strike of the hillslope. This manipulation assumes that the principal stress is aligned down the steepest gradient of the topography. Therefore, the divergence of the apparent dip of the bedding plane is measured relative to the attributes of hillslope aspect and gradient. Negative values of apparent dip divergence represent bedding with a shallower dip than **the** hillslope gradient. Similarly, positive values of bedding dip represent bedding planes inclined at steeper angles than the hillslope gradient. For stable **hillslopes** there is no correlation of the apparent dip divergence between the bedding plane and the **hillslope** gradient (Figure 4-5a). In contrast, over 75% of the landslide sites have apparent bedding dips oriented within $\pm 20^\circ$ of the hillslope gradient (Figure 4-5b). Roughly slope-parallel **bedding** is most susceptible to failure. A similar examination of apparent dip divergence for primary joint sets indicates no correlation of angular relationships between joint orientation and topography for both stable and unstable sites (Figures 4-6a & b).

The distribution of bedding plane dips relative to the hillslope gradient in Figure 4-5b is skewed toward a positive divergence, that is, the majority of landslide sites have bedding dips steeper than the **hillslope** gradient. This poses a problem with one of the mandatory conditions of failure models. Most models require that the dip of a discontinuity, presumably acting as the failure **plane**, have a shallower angle relative to horizontal than the hillslope gradient, allowing the discontinuity to daylight in the slope face (see Chapter 2). Empirically though, failure sites are not limited to this condition. The frequency of landsliding is associated with the apparent dip divergence between **the** bedding and **hillslope**, but not limited to the conditions assumed by **failure** models. When

bedding planes are steeper than the hillslope gradient, failure must propagate across bedding planes in order to daylight in the slope face. Thus the slip surface morphology is not limited to movement purely along one discontinuity and probably utilizes both the bedding planes and joint sets which are often oriented at high angles to bedding.

The highest incidence of landsliding occurs where the angular divergence between hillslope and bedding orientation, for both strike and dip, is minimized. Figure 4-7a shows that sites where the strike of the **bedding** is within 30° of the trend of the long axis of the **hillslope**, in conjunction with the apparent bedding dip divergence being within -20° to 40° of the **hillslope** gradient, account for almost half of the landslides studied. Furthermore, over the **full range** of **strike** divergences, 94% of the failures are constrained within -20° to 40° of the apparent dip divergence between bedding plane orientation and topography. Where the topography and underlying geologic structure are sub-parallel, the shear stress arising from the principal stress, σ_1 , on the bedding plane will be maximized, creating the highest potential for instability. In contrast, the apparent dip divergence of the primary joint sets for landslide sites are primarily concentrated at high angles to topography (Figure 4-7b). Discontinuities oriented normal to the topography will experience no shear component in response to the principal stress, σ_1 , and thus the normal force will be maximized. Therefore, the relative strength across joint sets is high, further downplaying the role of joint sets in the formation of these deep-seated landslides.

Landscape Profiles, RMS, and Geologic Structure

Where the bedding plane is parallel to the hillslope orientation the **structural** control on topographic expression is evident. The topographic profiles of Figures 4-8a & b, cross-sectional views normal to the trend of the long axis of the topography, were field surveyed with tape, hand level, and compass while Figure 4-8c was produced from the Bellingham South U.S. Geological Survey 7.5 minute quadrangle. All locations were selected such that the strike of the bedding was parallel to the strike of the topography. Anti-dip slopes characteristically have good outcrop exposures and gradients up to 40% steeper than the neighboring dip slope, which typically is mantled with colluvium. Figures 4-8a, b, & c expose a correlation of geologic structure with slope gradient and bedding RMS value. Comparison of the anti-dip and dip slopes at each location indicates that bedding RMS values on steeper anti-dip slopes are consistently higher. Even though all profiles disclose

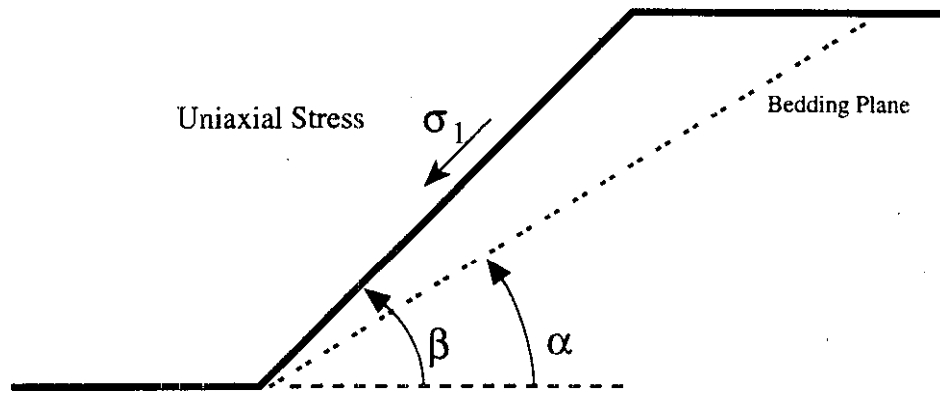
higher **RMS** values on the steeper gradient, anti-dip slope flank of the **hillslope**, the results obtained here do not corroborate Selby's result of a unique positive correlation between **RMS** values and hillslope gradient. Figure 4-2 reveals that it is possible to have equivalent values of **RMS** at different slopes depending on the relief and proximity to the limit of topographic development.

CONCLUSION

The **RMS** framework provides a basis for evaluation of lithologic variability and the importance of bedding plane and primary joint set orientation on deep-seated landslide susceptibility and local topographic expression. The approach developed here distinguishes between stable and unstable sites such that all **landslide** sites on Chuckanut are limited to **RMS** values less than 69. Analysis of the individual parameters within the scheme indicates that low **RMS** values for landslide sites reflect the influence of two factors: A) a large proportion of weak rock, usually shale, and/or B) an unfavorable slope parallel condition of topography and geologic structure.

It should be emphasized, however, that the results reported here are **formation-specific**. Although the description of the parameters responsible for instability in the Chuckanut Formation will be invariant, the relative significance of each parameter will most likely vary in applications to different **lithologies** and other regions. With respect to the Danington Phyllite, for example, it is anticipated that the effects of weathering, previously identified as crucial to slope stability in this lithology, would also **be** successfully represented in the **RMS** values through the intact rock strength and degree of weathering parameters. This approach provides a different perspective to highlight important features of the rock mass but should not be used as a substitute for understanding the mechanics of the issues investigated. In general, rock mass strengths are easily collected by walking or driving roads and examining bedrock in roadcuts. Because no samples are required, one can characterize large areas quickly if access allows. The modified **RMS** classification offers a simple, inexpensive tool to refine and supplement both data available on geologic maps and predictions of computerized slope stability analyses in a multi-level approach for recognizing the potential for deep-seated landsliding.

Figure 4- 1. a. **Uniaxial** stress state with principal stress, $\sigma_1 = \rho g H \cos \beta$, oriented parallel to idealized topography inclined at an angle β to the horizontal.
b. Mohr diagram of **uniaxial** stress state.



$$\sigma_1 = \rho g H \cos \beta$$

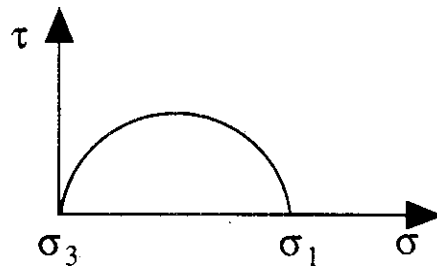


Figure 4-2. Bedding RMS values for transects characterizing the **Chuckanut** Formation **with** respect to topographic development. Landslide sites, enclosed by open circle, typically have lower strengths than neighboring stable hillslopes.

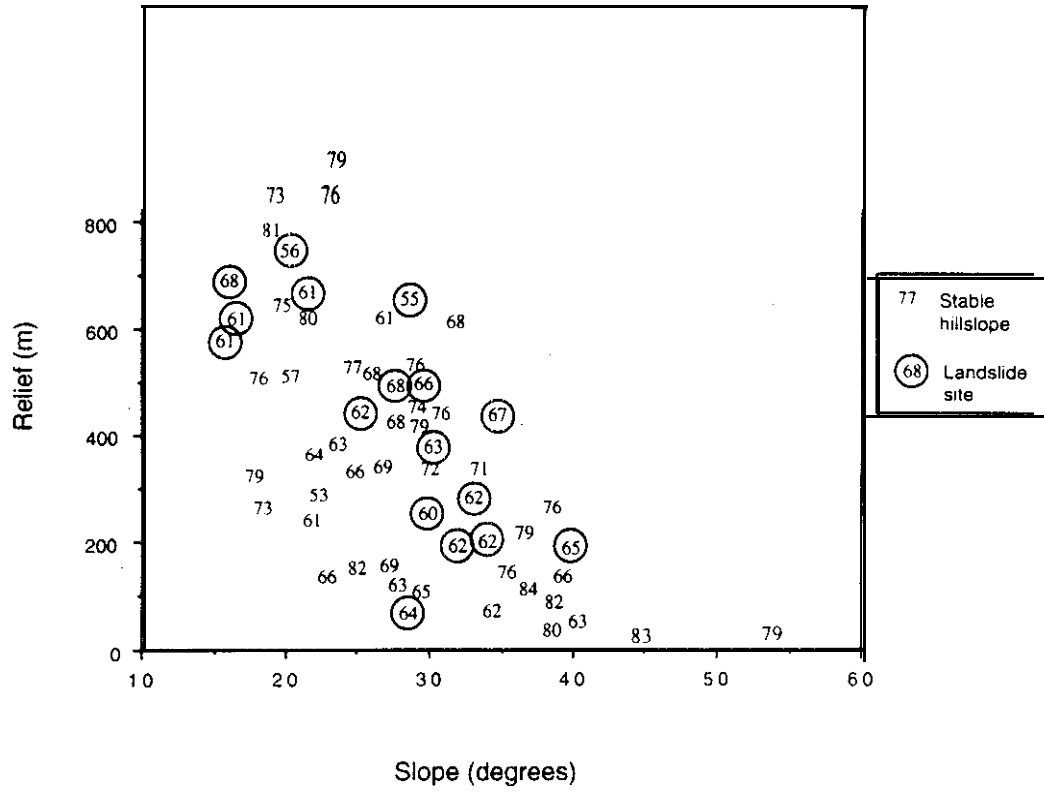


Figure 4-3. a. **Bedding** RMS values vs. relief within Chuckanut Formation.
b. Bedding **RMS** values vs. gradient within Chuckanut Formation. In both plots landslide sites are constrained below a bedding RMS value of 69.

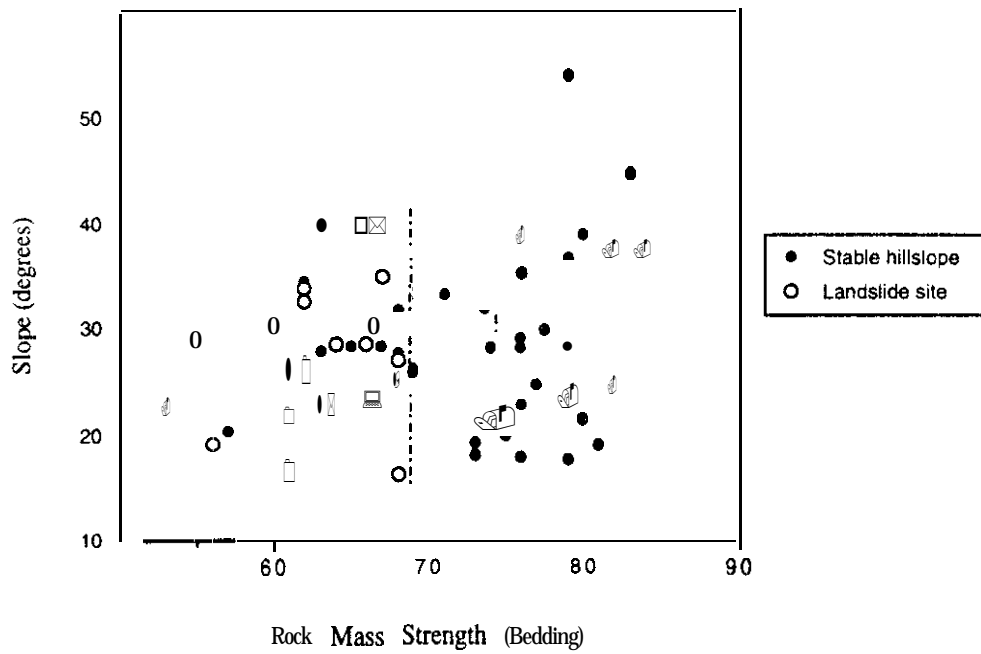
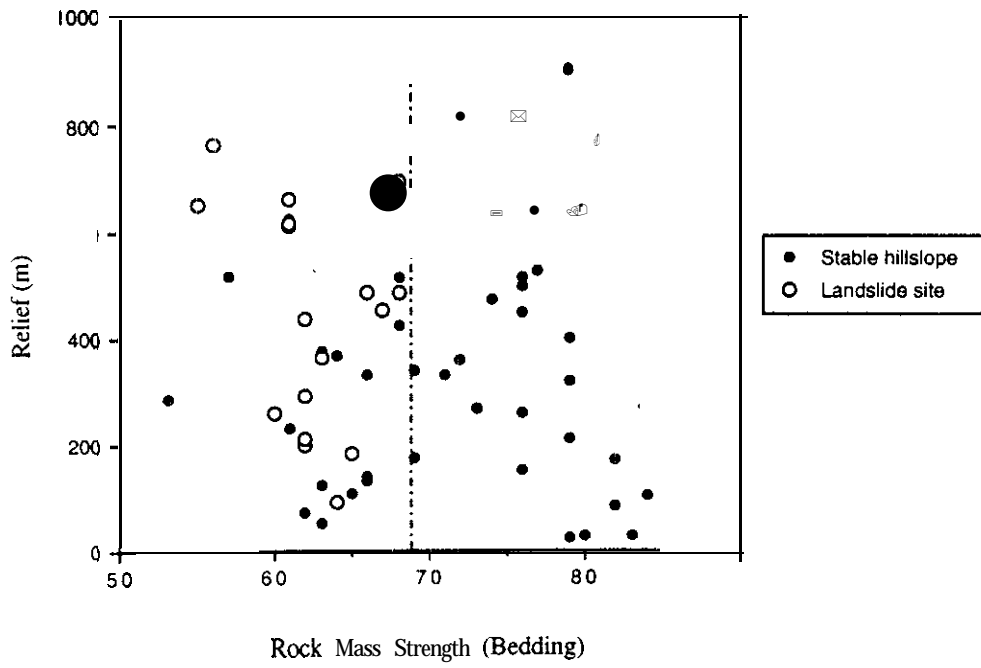


Figure 4-4. a. Jointing RMS values vs. relief within Chuckanut Formation.
b. Jointing RMS values vs. gradient within Chuckanut Formation.
Neither plot shows correlation of jointing **RMS** values with hillslope stability.

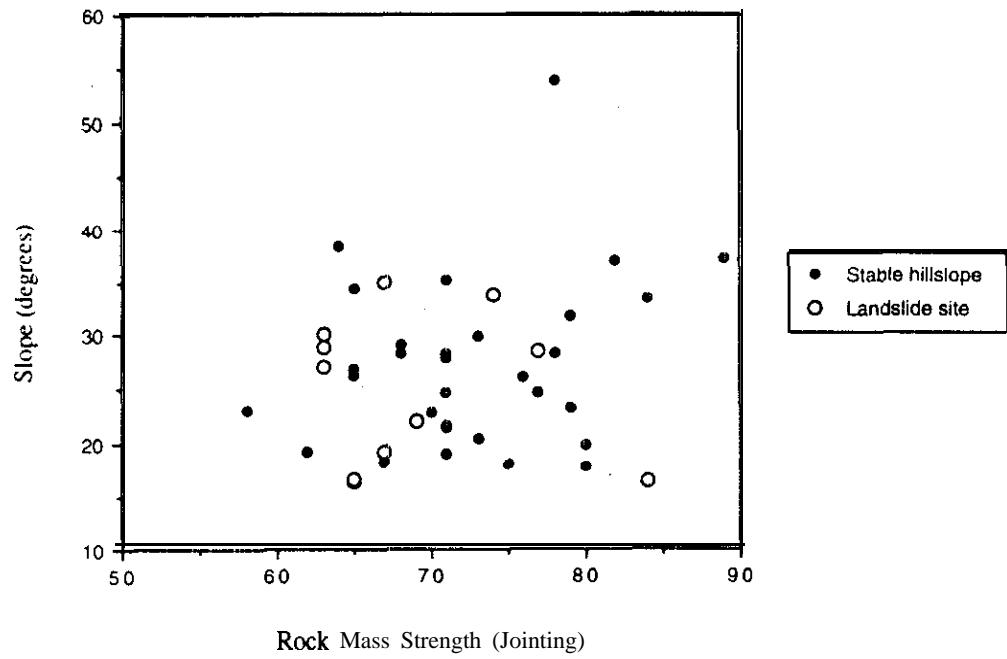
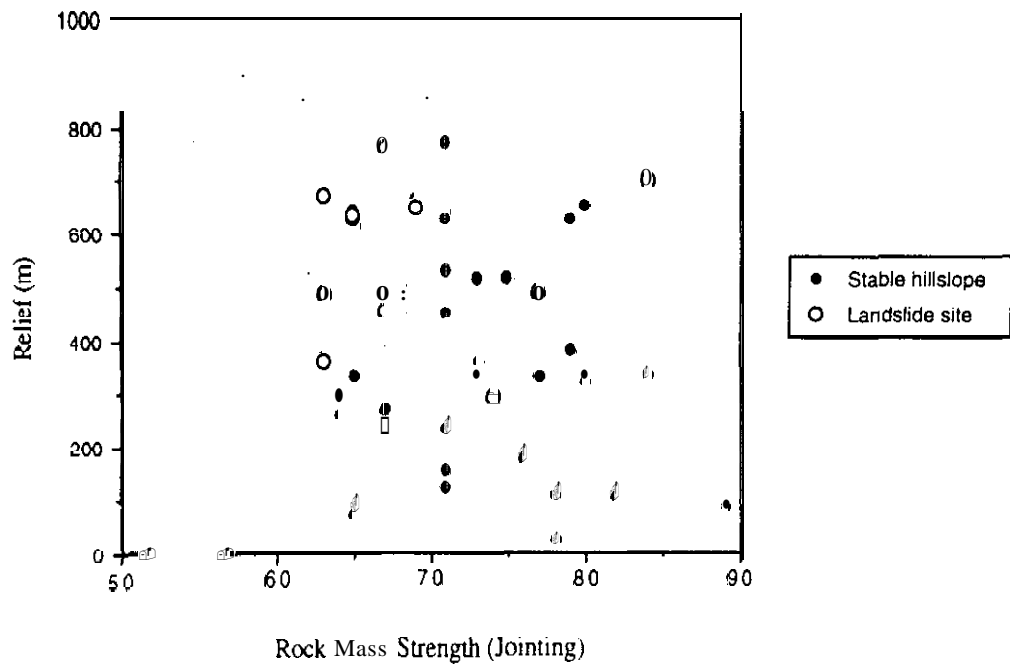


Figure 4-5. a. Frequency of stable **hillslopes** with respect to angular divergence between hillslope gradient and apparent dip of bedding plane showing no correlation.
b. Frequency of landslide sites with respect to the angular divergence between hillslope gradient and apparent dip of bedding plane revealing a **normal** distribution of landslide sites at low angles of divergence.

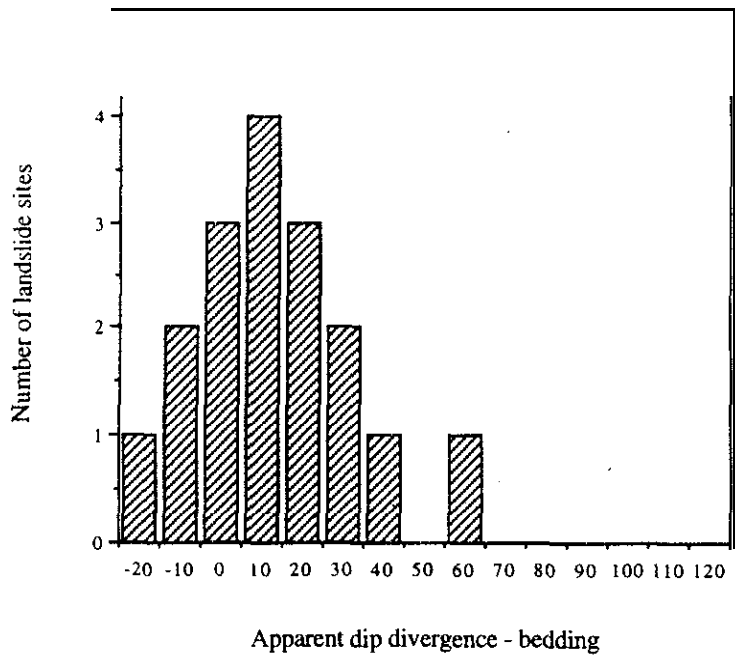
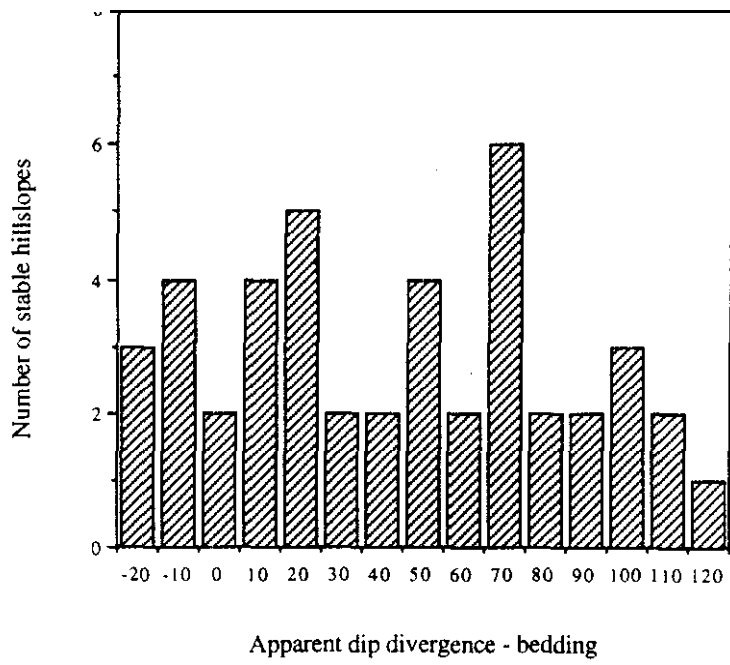


Figure 4-6. a. Frequency of stable **hillslopes** with respect to the angular divergence between hillslope gradient and apparent dip of primary joint set.
b. Frequency of landslide sites with respect to the angular divergence between hillslope gradient and apparent dip of primary joint set. Neither plot reveals a correlation between jointing **RMS** values with stability.

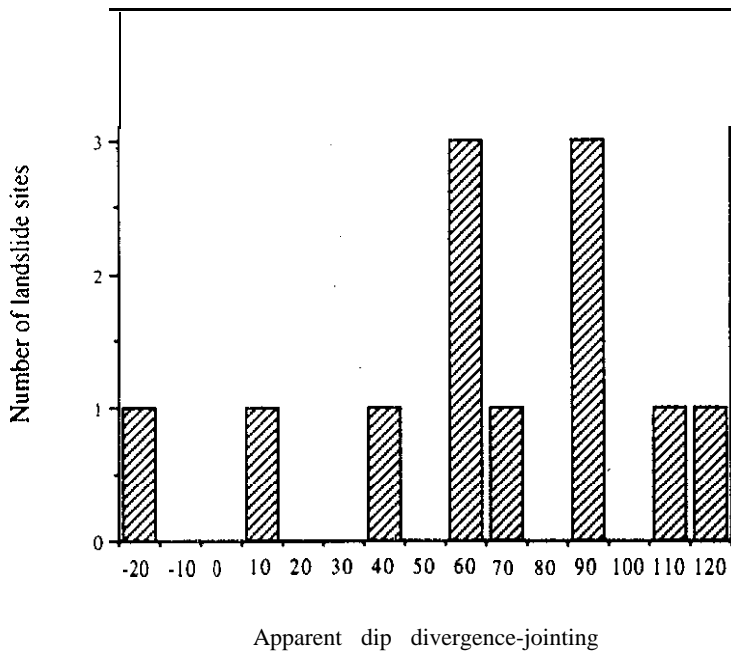
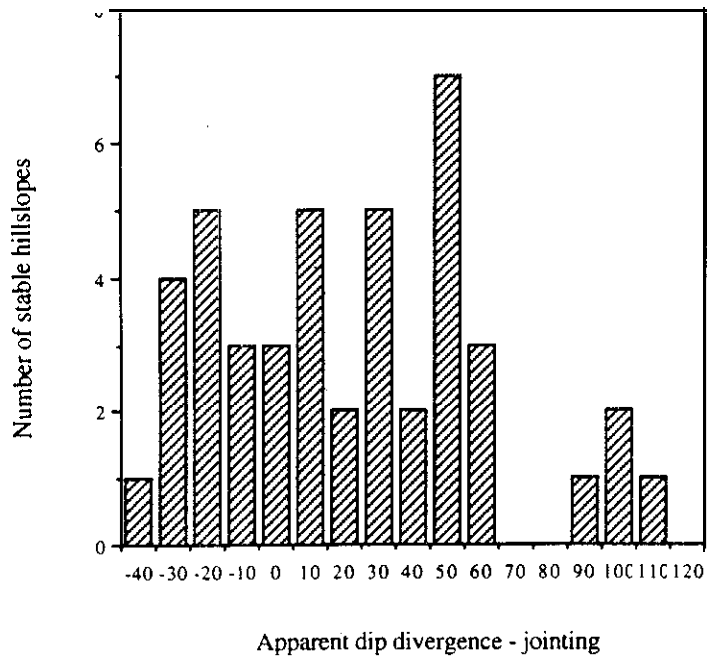


Figure 4-7. a. Distribution of strike and apparent dip divergence for bedding planes with respect to hillslope orientation for stable and unstable **hillslopes**. Values in squares represent percentage of landslide sites constrained within angular relationships denoted by dashed lines.

b. Angular relationships of primary joint sets **with** respect to topography.

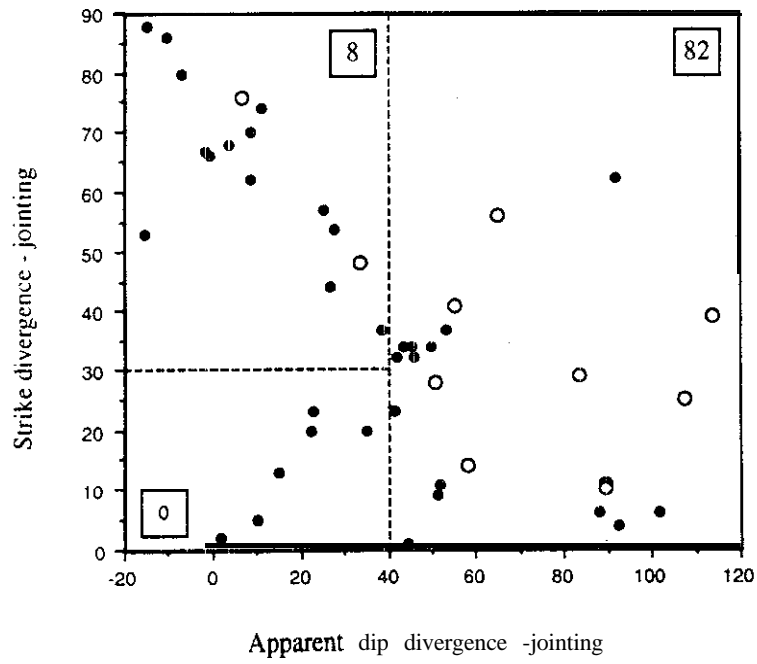
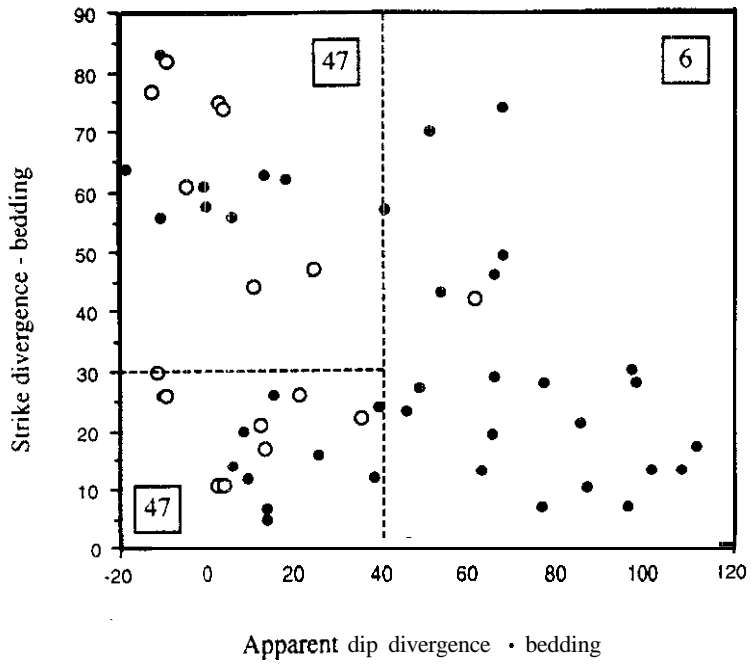


Figure 4-8. a, b, & c. Topographic profiles with varying vertical exaggerations demonstrating relationship between geologic structure, hillslope gradient (shown in square), and bedding **RMS** value (shown in circle).

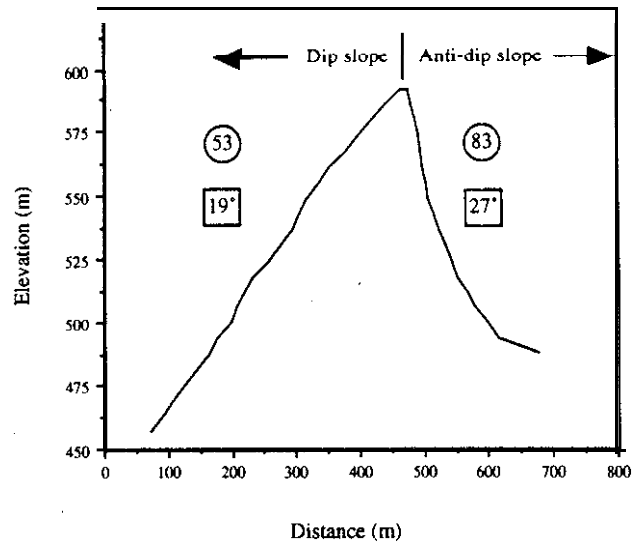
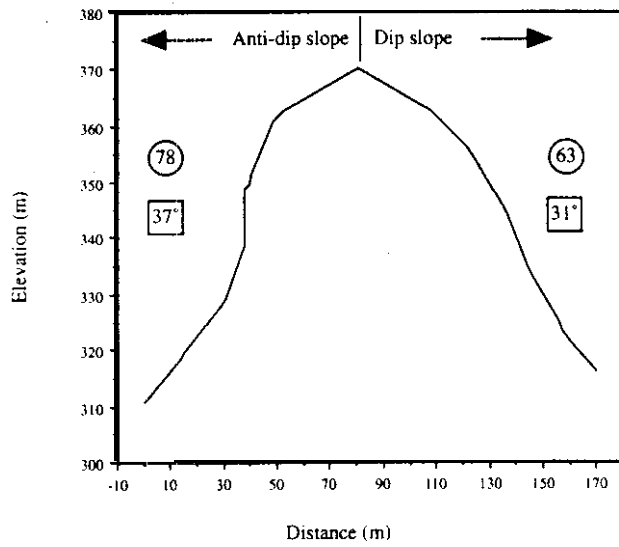
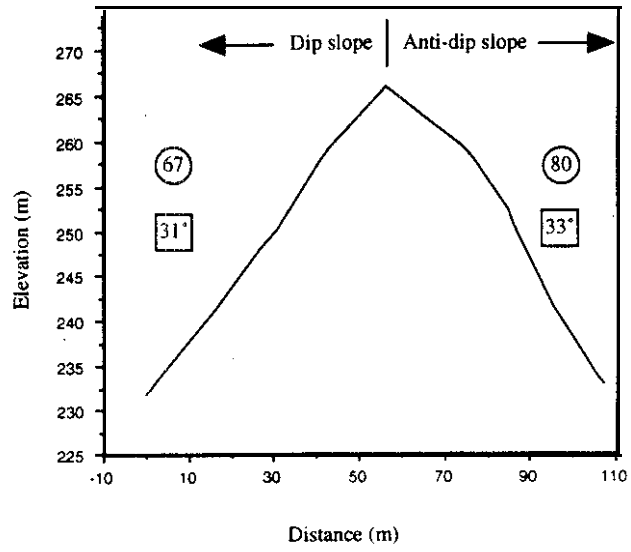


Table 4- 1. Rock mass strength (RMS) parameters and relative rating (R), *after*: Selby (1980).

Parameter	Very Strong	Strong	Moderate	Weak	Very Weak
Intact rock strength	Very coherent rock R = 20	coherent rock = 1	moderately coherent rock R = 14	weak rock R = 10	very weak rock R = 5
Weathering	unweathered R = 10	slightly weathered R = 9	moderately weathered R = 7	highly weathered R = 5	completely weathered R = 3
Discontinuity spacing	> 3 m R = 30	3 - 1 m R = 28	1 - 0.3 m R = 21	0.3 - 0.05 m R = 15	< 0.05 m R = 8
Discontinuity orientation	Very favorable Moderate dips into slope R = 20	Favorable Steep dips into slope R = 18	Fair Horizontal or vertical dips R = 14	Unfavorable Steep dips out of slope R = 9	Very unfavorable Moderate dips out of slope R = 5
Discontinuity width	< 0.1 mm R = 7	0.1 - 1 mm R = 6	1 - 5 mm R = 5	5 - 20 mm R = 4	> 20 mm R = 2
Discontinuity pervasiveness and infilling	none pervasive = 7	few pervasive R = 6	pervasive. no infill R = 5	pervasive, thin infill R = 4	pervasive, thick infill R = 1
Outflow of groundwater	none =	trace R = 5	slight < 25 l/min/10 m ² R = 4	moderate 25-125 l/min/10 m ² R = 3	great > 125 l/min/10 m ² R = 1
Total rating	100 - 91	90 - 71	70 - 51	50 - 26	< 26

after Selby (1980)

Table 4-2. Scheme used to determine intact rock strength by relative rebound of rock hammer, *after*: Selby (1980).

Description of rock strength	Rebound character from rock hammer/pick blow	Approximate unconfined compressive strength, MPa (R value)	Rock type example
Very weak rock crumbles under sharp blows with rock pick, can be cut with knife	no rebound, hammer forms impact crater	1 - 25 (5)	chalk, rock salt, lignite
Weak rock shallow cuts or scratches may be made with sharp knife	little to no rebound, hammer impact resounds with a dull thud; pick indents deeply with tin blow	25 - 50 (10)	coal, siltstone, schist
Moderately strong rock knife cannot scrape surface	little rebound, hammer impact resounds with a thud; pick forms shallow indentation	50 - 100 (14)	slate, shale, sandstone mudstone, ignimbrite
Strong rock hand sample breaks with firm blow from hammer	moderate rebound, hammer impact resounds with a ring; pick spalls small flakes	100 - 200 (18)	marble, limestone, dolomite, andesite, granite, gneiss
Very strong rock requires many blows from hammer to break hand sample	strong rebound, hammer impact resounds with a sharp ring; pick relatively ineffective	> 200 (20)	quartzite, dolerite, gabbro

Table 4-3. Scheme used to evaluate strength parameter representing discontinuity orientation with respect to hillslope orientation.

Stability Condition	Discontinuity orientation with respect to hillslope orientation	(R value)
Very favorable	Discontinuity dips into slope	
	planar discontinuity 10 - 40°	
	random discontinuity 10 - 70	(20)
Favorable	Discontinuity dips into slope	
	planar discontinuity 40 - 80	
	random discontinuity > 70	(18)
Fair	Horizontal to 10° dip out of or into slope	
	Nearly vertical - 4	(14)
Unfavorable	Discontinuity dips out of slope	
	planar discontinuity 40 - 80	
	random discontinuity > 70	(9)
Very unfavorable	Discontinuity dips out of slope	
	planar discontinuity 10 - 40°	
	random discontinuity 10 - 70	(5)

"Some say the Earth was feverous and did shake. "

▪ Shakespeare, *Macbeth*, II, 3

CHAPTER 5. EARTHQUAKES AND THE LIMIT TO TOPOGRAPHIC DEVELOPMENT

This chapter examines the influence of earthquake-induced strong ground motions on slope stability and limits to topographic development (LTD) through the application of a two-dimensional, limit-equilibrium slope stability model modified to include seismic accelerations. Earthquake-induced strong ground motions are considered as equivalent static forces, in stark contrast to their true highly dynamic nature. Appendices D and E present the modifications made to the Culmann model to incorporate the effects of seismic accelerations. The modified model is applied to the region in central California affected by the 17 October 1989 Loma Prieta earthquake as well as the study area in the Pacific Northwest.

HORIZONTAL AND VERTICAL ACCELERATIONS IN MODIFIED CULMANN MODEL

Horizontal and vertical seismic accelerations produce earthquake-induced forces that alter slope stability. The influence of strong ground motions on **hillslope** stability was estimated by modifying the Culmann model to incorporate seismic accelerations. Appendix D derives the equations relating to critical topographic development for equivalent static **earthquake-induced** horizontal forces while Appendix E derives those related to the equivalent static earthquake-induced vertical forces, oriented both vertically upward and downward. Gravitational (g) and seismic (Kg) accelerations are considered as body forces acting equally on every element of mass in a potential failure block. The seismic coefficient (K) is expressed as a fraction of the gravitational acceleration (e.g., $Kg=0.2g$). The magnitude of the force acting on a potential failure block in response to gravity alone is W , while the force induced by the additional seismic acceleration is F_e (Figures 5-1, 5-2, and S-3). Analysis of the individual earthquake component orientations reveals that: A) horizontal earthquake forces are the most destabilizing, adding the greatest amount to the downslope shear component (Figure 5-1), B) earthquake forces oriented vertically downward are not **as** destabilizing as a horizontally oriented earthquake forces (Figure 5-

2), and C) earthquake forces oriented vertically upward increase relative stability by reducing the apparent force of gravity and thus the **downslope** shear component (Figure 5-3).

The influence of these three earthquake-induced force orientations can be expressed in terms of the critical **hillslope** relief. Equation 5-1 (also equation D-4) defines the critical relief of a **hillslope** under the extremely destabilizing influence of horizontally oriented seismic accelerations:

$$H_c = \frac{2c}{\gamma} \frac{\sin \beta}{\sin(\beta - \alpha) [(\sin \alpha + K \cos \alpha) - (\cos \alpha - K \sin \alpha) \tan \phi]} \quad (5-1)$$

As discussed in Appendix D, horizontal accelerations disturb the force balance such that the inclination of the failure surface, α , will have a shallower inclination. The inclination of the maximum stressed failure surface under conditions of an equivalent static horizontal seismic force is expressed by equation 5-2 (also equation D-6):

$$\alpha = \frac{1}{2} \tan^{-1} \left[\frac{\tan \beta + \tan \phi + K(\tan \beta \tan \phi - 1)}{1 - \tan \beta \tan \phi + K(\tan \beta + \tan \phi)} \right] \quad (5-2)$$

That is, if the landslide surface formed **coseismically**, its inclination would be defined by equation 5-2. If, however, the earthquake-induced landslide is a reactivation of an older failure surface formed under **aseismic** conditions, the inclination of the failure surface would be defined by:

$$\alpha = \frac{1}{2}(\beta + \phi) \quad (5-3)$$

Under conditions of earthquake-induced forces oriented vertically downward, the relation for the critical relief is expressed by equation 5-4 (also equation E-9):

$$H_c = \frac{2c}{\gamma} \frac{\sin \beta}{\sin(\beta - \alpha) [\sin \alpha(1 + K) - \cos \alpha(1 + K) \tan \phi]} \quad (5-4)$$

where the inclination of the failure surface is described by equation 5-3. Vertically oriented earthquake forces do not alter the failure surface inclination.

Finally, seismic accelerations oriented vertically upward actually serve to increase the critical relief of a hillslope. Equation 5-5 (also equation E-4) reveals that seismic accelerations oriented vertically 'upward have a stabilizing effect because they tend to decrease the downslope shear component driving instability:

$$H_c = \frac{2c}{\gamma} \frac{\sin \beta}{\sin(\beta - \alpha) [\sin \alpha(1 - K) - \cos \alpha(1 - K) \tan \phi]} \quad (5-5)$$

where the inclination of the failure surface is defined by equation 5-3. Since vertically upward oriented earthquake-induced forces stabilize hillslopes, their influence will subsequently not be discussed. In the following analyses, horizontal and vertically downward earthquake-induced forces are considered using back-calculated properties obtained in Chapter 3. Dry hydrologic conditions are assumed in order to simplify calculations.

APPLICATION TO SANTA CRUZ MOUNTAINS STUDY AREA

The 17 October 1989 **Loma Prieta** earthquake in the Santa Cruz Mountains of central California initiated extensive landsliding. Although landslides triggered during the earthquake occurred throughout an area of nearly 14,000 km², the highest concentration were located in the epicentral region (**Plafker** and Galloway, 1989). Seven kilometers from the epicenter the **M_s7.1** earthquake produced strong ground motions with peak accelerations up to **0.47g** vertically and **0.64g** horizontally (Spittler et al., 1990). For comparison, during the 1971 San Fernando earthquake horizontal accelerations reached **1.15g**, one of the largest recorded accelerations (Bolt, 1988). In the mountainous epicentral region landslides were identified by Weber and Nolan (1989); Spittler and Harp (1990); Spittler et al. (1990); Griggs et al. (1991); McLaughlin et al. (1991); and **Manson** et al. (1992). The location of earthquake-induced coastal failures are identified by Plant and Griggs (1990); Sydnor et al. (1990); and Sitar (1991).

The combination of identified earthquake-induced landslides in conjunction with measured seismic accelerations in the **epicentral** region provides a unique opportunity to test model predictions. Applying the modified Culmann model with back-calculated material properties from Chapter 3, Figure 5-4a shows the LTD suppression under a range of horizontal accelerations for aseismically formed failure surfaces. For comparison, the measured peak horizontal acceleration of **0.64g** would correspond to widespread instability in the model prediction. The modeled LTD suppression produced by vertically downward oriented seismic accelerations (Figure 5-4b), however, is minor relative to the fields of instability produced by horizontal accelerations.

Equating the potency of pore pressures with earthquake forces, the position of the LTD under a horizontal acceleration of **0.4g** (Figure 5-4a) is roughly equivalent to the LTD position under the hydrologic condition of complete saturation depicted in Figure 3-17a. For the case of vertically downward oriented seismic accelerations (Figure 5-4b), though, the **field** of instability predicted by completely saturated conditions is far more encompassing than the considerable acceleration of **0.6g**.

In order to evaluate the choice of failure surface initiation mechanisms for horizontally oriented seismic accelerations, earthquake-induced failures within the relatively weak marine sandstones, mudstones, and shales of the Santa Cruz Mountains are modeled with both coseismically and aseismically formed failure planes (equations 5-2 and 5-3). Figure 5-5 shows the suppression of the LTD for failure planes initiating coseismically under horizontal accelerations (compare with Figure 5-4a which assumes aseismically formed failure planes). It is apparent that the assumption related to the timing of failure plane formation strongly influences the limits of topographic development. The selection, though, of failure plane initiation mechanisms can be guided by the history of landslide movement. For example, a vast number of **Loma Prieta** earthquake-induced landslides were **reactivations** of previously identified dormant landslides (Cooper-Clark and Associates, 1975; Spittler et al., 1990; Griggs et al., 1991). If these sites were originally formed through progressive **aseismic** strain, their reactivation during the **Loma Prieta** earthquake supports the contention that seismic accelerations predominately exaggerate movement on previously formed planes of weakness and only rarely generate coseismic failure surfaces in coherent bedrock.

Coseismically formed failure surfaces produce more widespread instability because they have shallower inclinations than those formed aseismically. Comparison of equations 5-2 and 5-3 reveals that the failure surface inclination, α , will have a shallower angle if formed coseismically given otherwise equal conditions. For example, if $\beta = 60^\circ$, $\phi = 30^\circ$, and $K = 0.2$ equation 5-2 produces a failure plane inclined at $\alpha = 41^\circ$. In contrast, equation 5-3 predicts an **aseismically** formed failure plane inclination of $\alpha = 45^\circ$. Therefore, with a horizontal seismic acceleration of two-tenths of gravity, equation 5-2 yields a failure plane with approximately a 10% shallower gradient. Thus, for a given hillslope gradient, it is this shallower failure surface inclination that dramatically reduces stable relief.

To include **all** sites undergoing failure in response to the **Loma Prieta** earthquake, however, a coseismically formed failure plane would be chosen (Figure 5-5). This approach, though, is radically conservative, encompassing almost the entire landscape. The LTD position is based on back-calculated properties representing maximum values for a wide range of lithologies, spanning seven formations. If all sites exhibited equal strength and were incised to their full topographic potential, they would all plot along a single LTD curve. In reality though, rock strength is spatially variable throughout a landscape. Therefore, identified landslides exhibit a wide range of slope/relief characteristics and the LTD locations based on maximum strength parameters should not be expected to embody all landslide sites. Furthermore, the magnitudes of seismic accelerations are highly variable depending on local site conditions.

APPLICATION TO PACIFIC NORTHWEST STUDY AREA

Although there is no historical record of large shallow thrust earthquakes anywhere along the Cascadia subduction zone within the past 150 yr., recent research has identified an active tectonic past in the Puget Sound region (Schedlock and Weaver, 1991; Atwater and Moore, 1992; Bucknam et al., 1992). The Cascadia subduction zone is quite similar to those in southern Chile, southwestern Japan, and Columbia; all of which have experienced very large ($M_w > 8.0$) earthquakes in historic times (**Heaton and Hartzell, 1986**). This and other evidence led **Heaton and Hartzell (1986)** to suggest the Cascadia subduction zone may produce a $M_w > 8.5$ earthquake with an average repeat time of 400 to 500 yr.

Ground motions resulting from such subduction-zone earthquakes in the study area of the northern Puget Sound and western Cascades are expected to range from **0.2g** to **0.5g**, with ground motions on soil up to four times greater than ground motions on rock. Modeling of acceleration time histories and response spectra for **M_w8** earthquakes in the Puget Sound region by Cohee et al. (1991) indicates **0.2g** peak horizontal accelerations on rock with **0.5g** on soil. A study by Perkins et al. (1980) integrated historic seismicity in 19 seismogenic zones with available geologic information to produce a regional seismic hazard assessment of western Washington. The resulting probabilistic estimates were expressed as **peak** horizontal accelerations on rock for a specific return period. In the study area, the work of Perkins et al. (1980) predicts a peak horizontal acceleration on rock of **0.12g** for a 100 yr. return interval, **0.21g** for a 500 yr. return interval, and **0.33g** for a 2500 yr. return interval. Work by Heaton and Hartzell (1989) using previous ground motion records from large subduction quakes and Green's Function corroborate the above peak horizontal acceleration estimates.

It is commonly recognized that an earthquake can trigger numerous landslides in a broad expanse surrounding its epicenter (Keefer, 1984; Wilson and Keefer, 1985). Studies in the Puget Sound region linking landslides with earthquakes include Keefer (1983), Jacoby et al. (1992), and Schuster et al. (1992).

Using back-calculated material properties and landslide distributions in conjunction with the knowledge of expected peak horizontal ground accelerations resulting from a subduction earthquake, the seismically induced suppression of the LTD is explored with respect to both **Quaternary** glacial deposits and the Chuckanut Formation. Conservative estimates of instability are obtained by only considering the influence of horizontal accelerations. The instability produced by vertically downward oriented accelerations was determined to be relatively minor and thus is not depicted.

Glacial Deposits

Failures within glacial sediments operate on relatively short time scales. Examination of landslide masses in the field indicates the time interval between slump initiation, downslope movement, and removal of failure debris by **fluvial** erosion is on the order of seasons to years. Furthermore, topples may directly enter the channel and rapidly

disaggregate. Therefore, it is assumed that the bulk of the landslide surfaces within glacial sediments form coseismically with inclinations dictated by the severity of strong motions experienced at site. Assuming coseismically formed failure planes, the limits to topographic development under conditions of horizontal seismic accelerations are modeled with equations 5-1 and 5-2 and plotted in Figure S-6.

Figure 5-6 shows the LTD distribution under a range of strong motions from horizontal accelerations of $0g$ to $0.6g$. Comparing the hydrologic and seismic responses reveals that the relative suppression of the LTD at $0.2g$ represents more widespread instability than the LTD position defined by fully saturated conditions (Figure 3-6a). Note that horizontal accelerations of $0.2g$ to $0.4g$ would force the majority of channel banks to become unstable. This observation is critical because accelerations of $0.4g$ are well within the expected range of ground motions on soil resulting from a subduction earthquake (Cohee et al., 1991). Furthermore, if a site is located close to a small local earthquake, the resulting ground motion may be equivalent to a larger far-field earthquake. Supporting this contention is the fact that much historical seismicity has been recorded in the study area (Rasmussen, 1967; Crosson, 1983; Taber and Smith, 1985). Thus, the recurrence interval of an event producing a $0.2g$ horizontal acceleration for soils or unconsolidated materials may be relatively high. When earthquakes generating horizontal accelerations of $0.2g$ or greater occur, a large input of sediment into the adjacent channels should be expected to result from extensive channel bank instability.

Chuckanut Formation

In contrast to glacial deposit landslides which are thought to form coseismically, I suspect that bedrock failures within the Chuckanut Formation form progressively with movement greatly accentuated during earthquakes. That is, failure planes of bedrock landslides develop over long periods of time as rock weathers and cohesive bonds are broken. Subsequently, failure surface inclination is determined by material properties and topography-induced gravitational stresses. Earthquake-induced ground accelerations are thought to increase the pervasiveness of failure surfaces and may greatly accentuate movement along existing planes of weakness within a **hillslope**. Therefore, failure plane inclinations of bedrock landslides within the Chuckanut Formation are presumed to form aseismically in accordance with equation 5-3.

Hillslopes within the Chuckanut Formation are divided into anti-dip and dip orientations and their respective topographic development limits under horizontal seismic accelerations were calculated. Figure 5-7a shows the suppression of the LTD for anti-dip slopes while Figure 5-7b shows LTD locations for dip slopes. From these distributions it appears that horizontal accelerations of **0.4g** are necessary to initiate extensive landsliding. The work of Perkins et al. (1980) indicates that accelerations of **0.33g** on rock occur with a return interval of roughly 2500 yr in this area. Assuming this earthquake return interval frequency, hillslopes of the Chuckanut Formation may have experienced at least five earthquakes capable of generating considerable ground motions since deglaciation (13,000 yrs.). Seismic activity may have a very important, and perhaps dominant, influence on the large-bedrock landslides in the study area. Large magnitude earthquakes, therefore, should be considered as a major factor in the development of bedrock landscapes, as will be discussed in Chapter 6.

CONCLUSION

Highly dynamic earthquake-induced ground motions and the associated influence on hillslope stability has been considered in the context of a simple stability model. Predictions on the extent of instability produced by horizontally and vertically oriented earthquake-induced body forces indicate that worse case scenario estimates are obtained from horizontal seismic accelerations. In addition, the temporary suppression of the LTD decreases in proportion to the magnitude of seismic accelerations. Furthermore, the relative timing of failure plane generation for horizontal forces is crucial to predicting the degree of LTD suppression. The widespread landslide **reactivations** occurring in response to the **Loma Prieta** earthquake may indicate that seismic accelerations opportunistically exaggerate movement on failure planes formed by progressive **aseismic** strain over long time intervals. Under the assumption of coseismically formed failure planes, glacial sediments composing channel banks may undergo widespread landsliding in the event of an earthquake. Under the assumption of aseismically, progressively formed failure planes, the horizontal accelerations necessary to include the distribution of failures in the Chuckanut Formation are in agreement with estimates of peak horizontal ground motions in the Puget Sound from previous studies.

The long-term additive history of repeated seismic disturbance, loosening rock masses and reducing shear resistance, may be more influential than the most recent earthquake. For example, the landscape carved into the Chuckanut Formation may have experienced at least five major **earthquakes** producing horizontal accelerations greater than **0.3g** since deglaciation, **all** contributing incrementally to strength reduction. In contrast, landforms composed of glacial deposits evolve over shorter time scales and the seismic influence may subsequently induce catastrophic hillslope failure coseismically in addition to furthering cumulative strength degradation.

Although the focus has been on major earthquakes as a source for seismic accelerations, locally generated strong ground motions from smaller earthquakes in close proximity must also be considered as a potential origin of strong ground motions. Seismicity generated along the flanks of large **Quaternary** stratovolcanoes in the Cascades, for example, may destabilize **Quaternary** glacial deposits on a fairly frequent basis. More work, however, is required to accurately characterize both recurrence intervals and expected shaking intensity from either source.

The interaction of large magnitude earthquakes and deep-seated landslides implies a potential feedback mechanism serving to limit topographic development in tectonically active **orogenic** belts. Ironically, the same forces that serve to build mountain ranges through compressional deformation, often associated with large earthquakes, also serve to limit the degree of topographic development.

Figure 5-1. Force due to earthquake, F_e , expressed as an equivalent static force with magnitude KW , where K is the seismic coefficient and W is the weight of the failure block. The most **destabilizing** condition is depicted with F_e oriented out of the slope face in the horizontal plane. F_r denotes the resultant force. Dashed line represents potential failure plane.

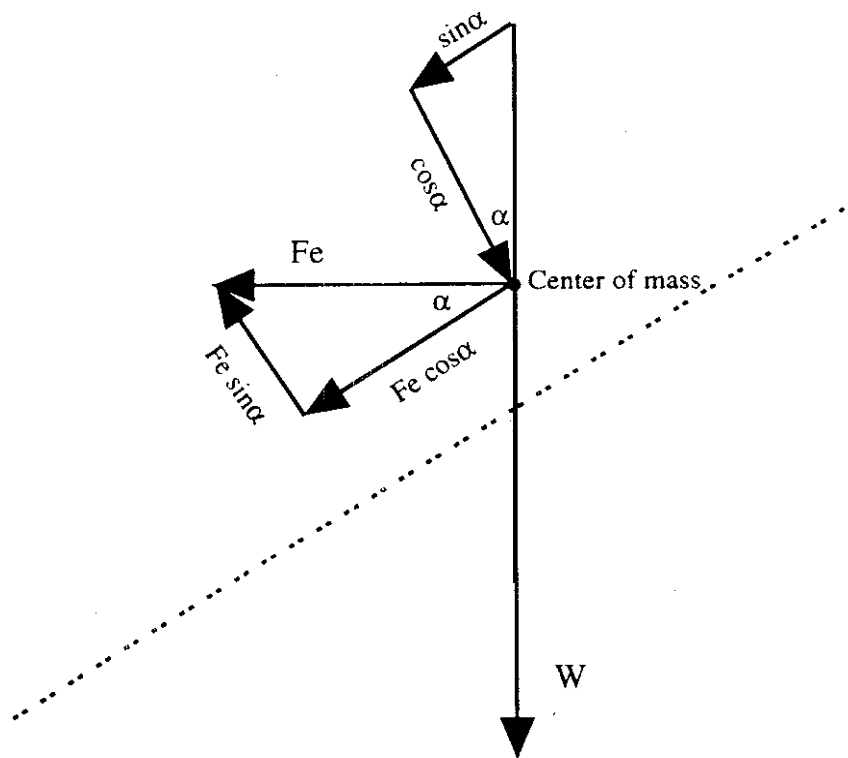
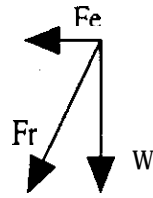
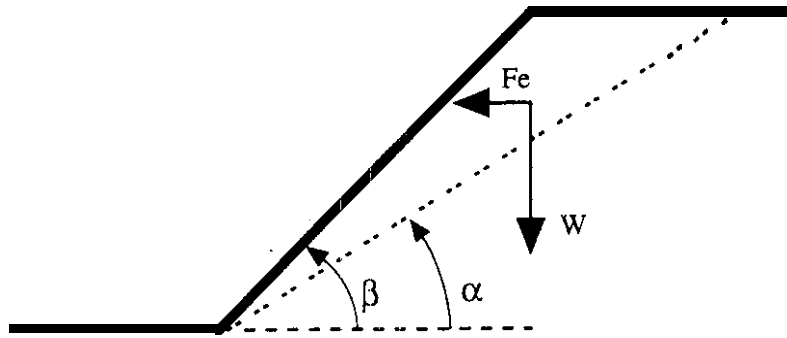


Figure 5-2. Force due to earthquake, F_e , expressed as an equivalent static force with magnitude KW , where K is the seismic coefficient and W is the weight of the failure block. A moderately destabilizing condition is depicted with F_e oriented vertically downward. F_r denotes the resultant force. Dashed line represents potential failure plane.

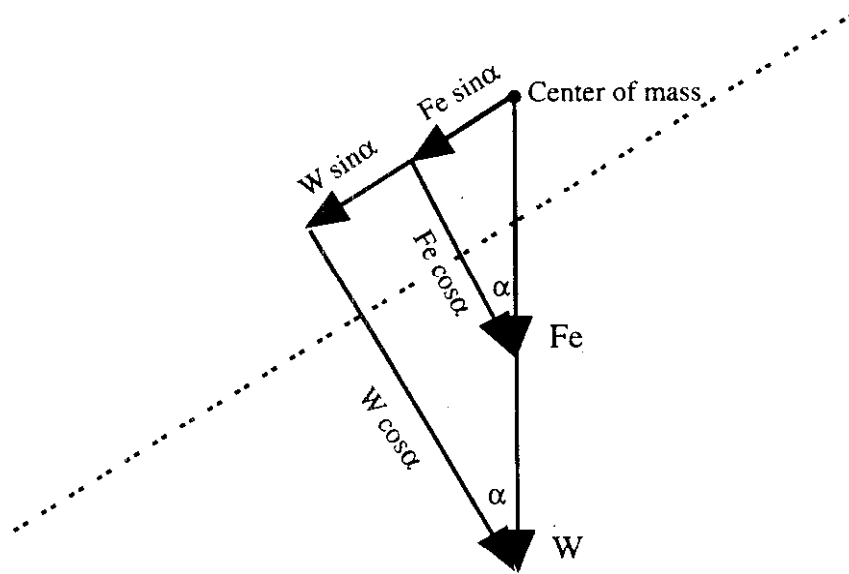
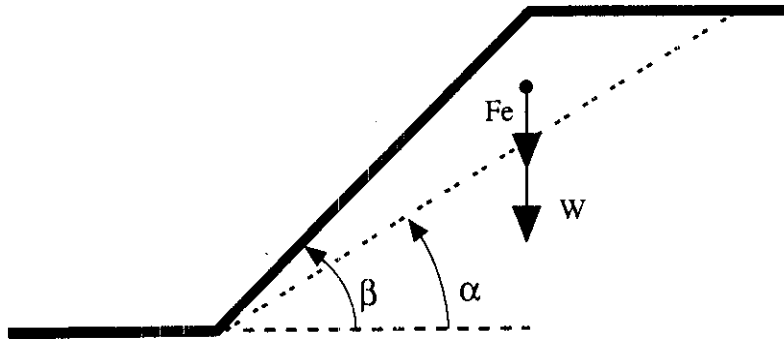


Figure 5-3. Force due to earthquake, F_e , expressed as an equivalent static force with magnitude KW , where K is the seismic coefficient and W is the weight of the failure block. A stabilizing condition is depicted with F_e oriented vertically upward. F_r denotes the resultant force. Dashed line **represents** potential failure plane.

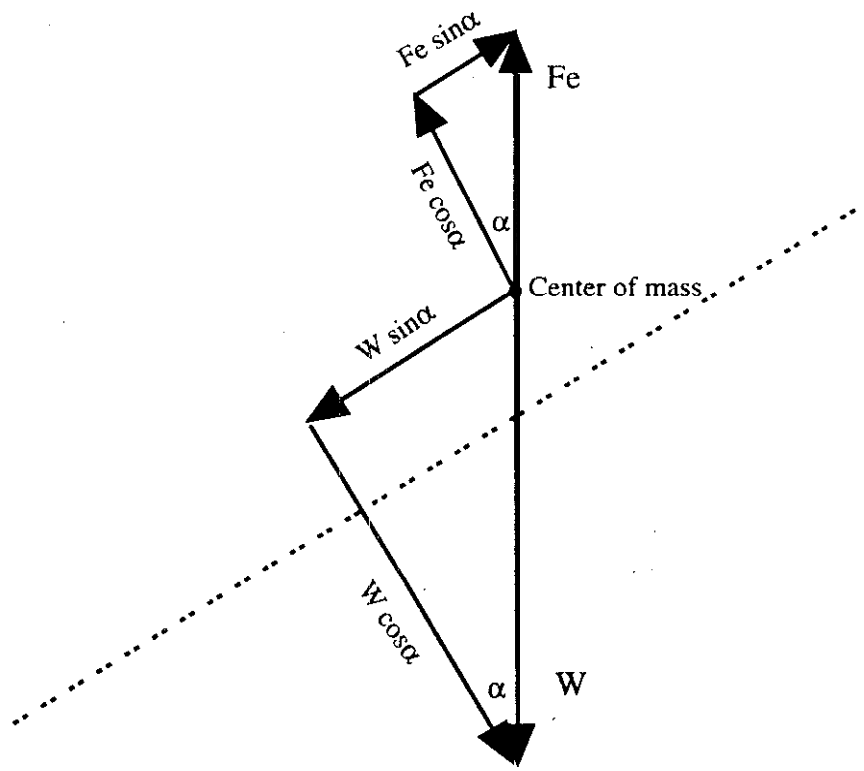
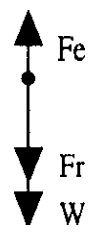
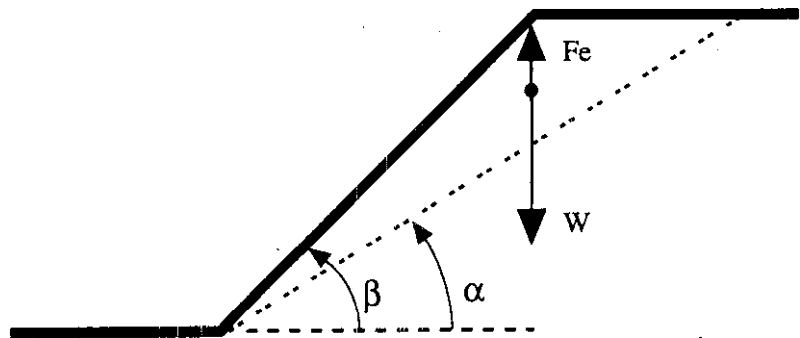


Figure 5-4. a. Location of **LTD** under range of horizontal seismic accelerations from 0g to **0.6g** for lithologies of the Santa **Cruz** Mountains assuming aseismically formed failure planes. The large number of landslide **reactivations** lends credence to the assumption that failure planes formed aseismically.

b. Location of **LTD** under range of static vertically downward oriented seismic accelerations from 0g to **0.6g** for lithologies of the Santa **Cruz** Mountains.

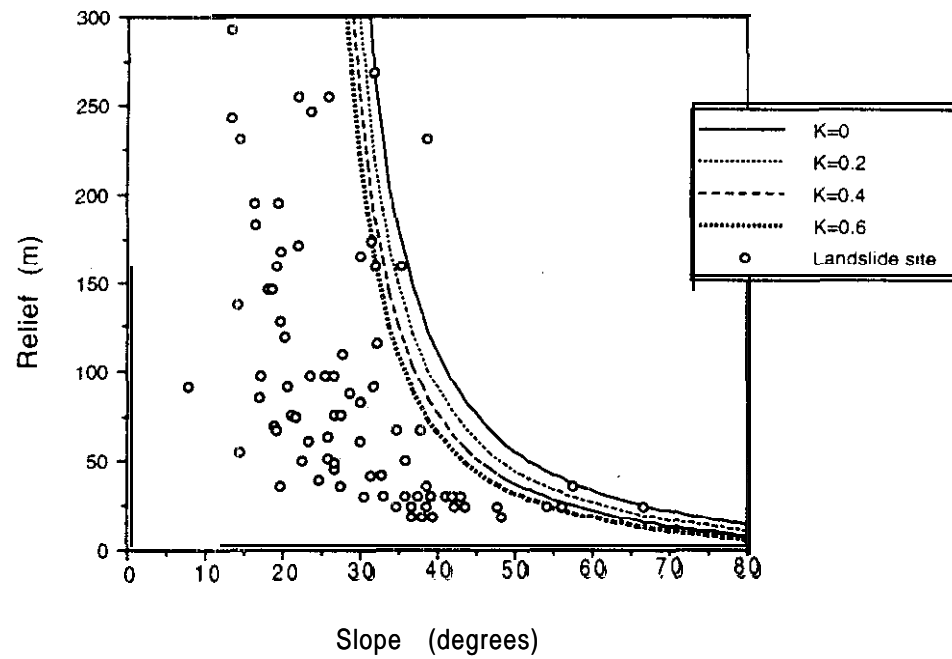
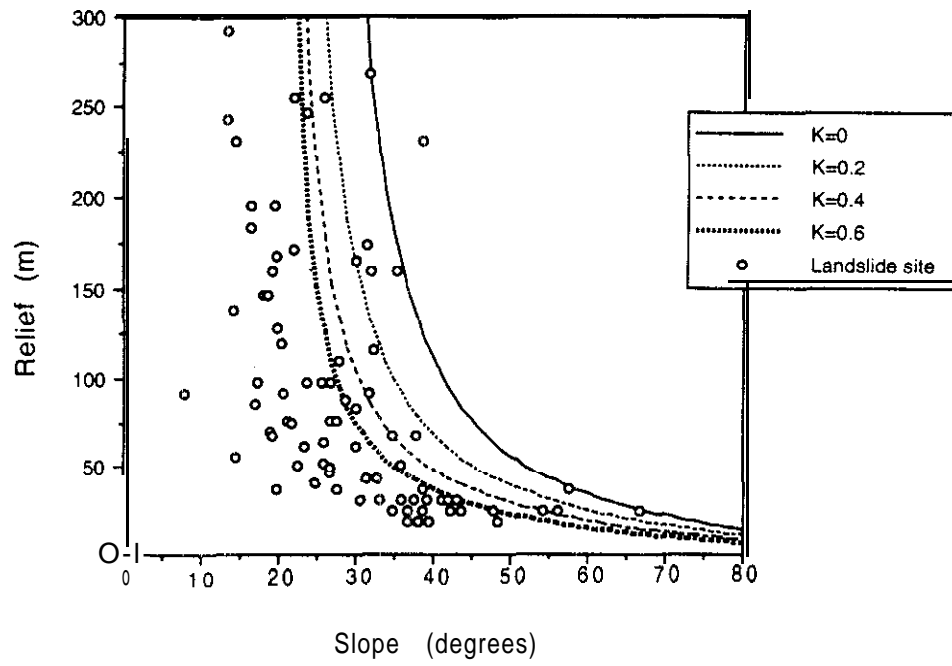


Figure 5-5. Location of LTD under range of horizontal seismic accelerations from 0g to 0.6g for lithologies of the Santa Cruz Mountains assuming coseismically formed failure planes. The vast majority of the landscape is predicted to be unstable with horizontal accelerations of 0.2g or greater.

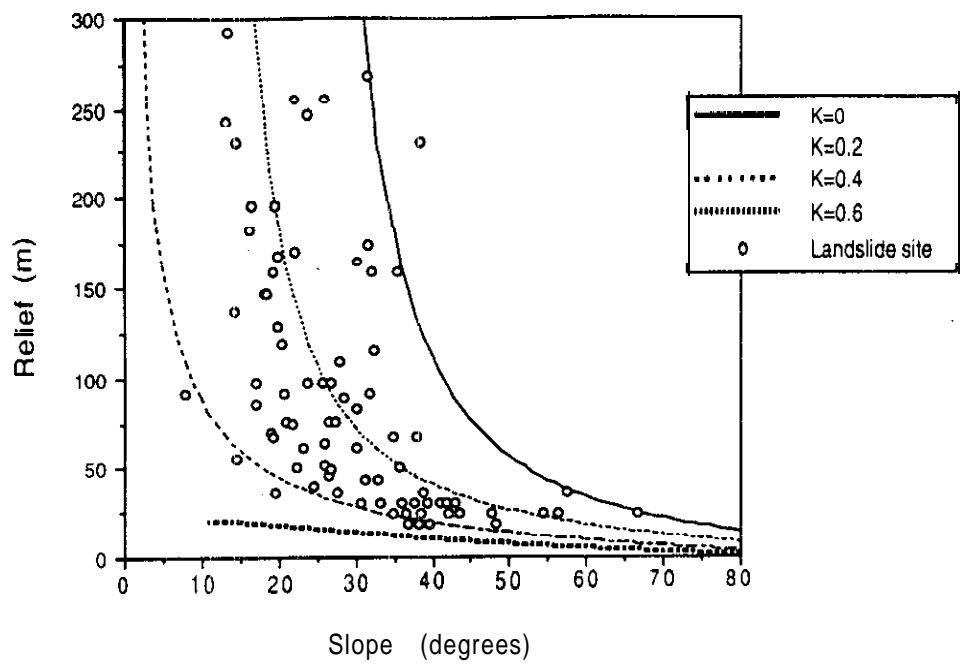


Figure 5-6. Location of **LTD** under a range of horizontal seismic accelerations from $0g$ to $0.6g$ for Quaternary glacial deposits assuming coseismically formed failure planes.

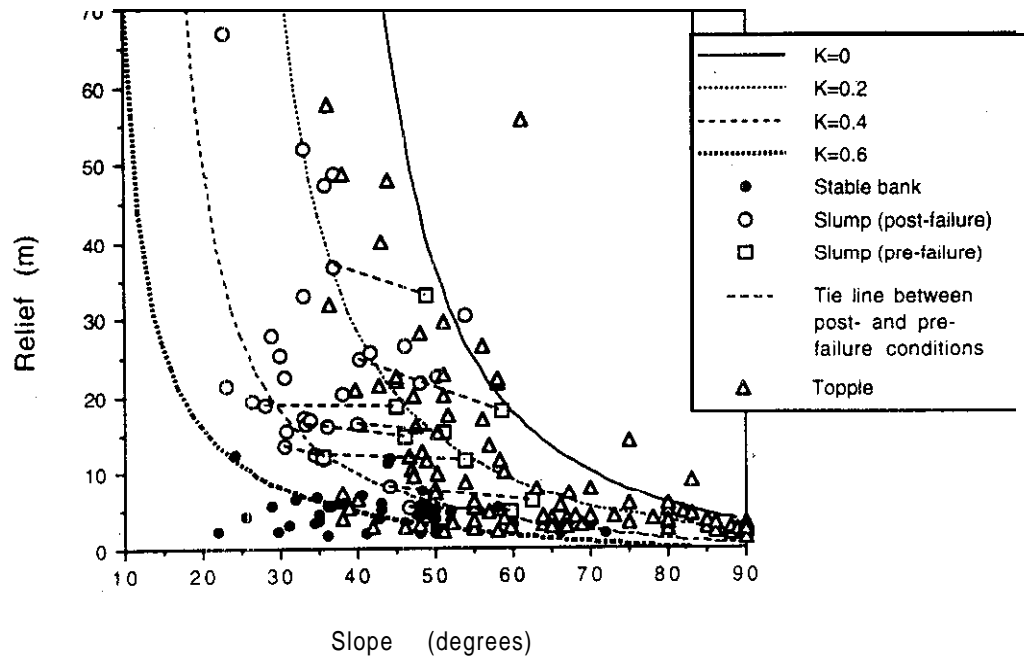
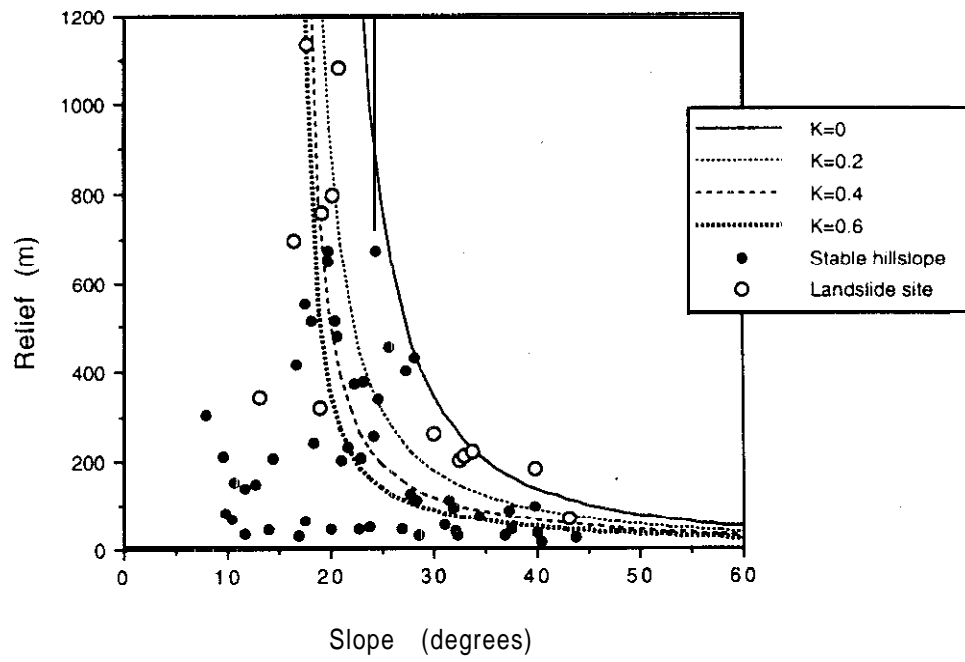
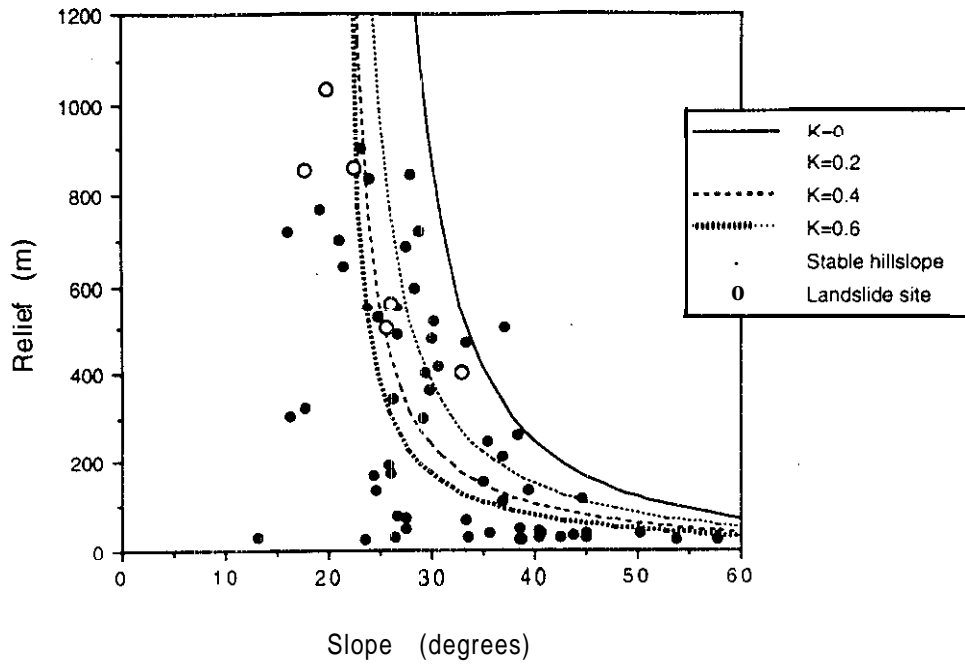


Figure 5-7. a. Location of LTD under range of horizontal seismic accelerations from 0g to **0.6g** for anti-dip slopes of the Chuckanut Formation assuming coseismically formed failure planes.

b. Location of LTD under range of horizontal seismic accelerations from 0g to **0.6g** for dip slopes of the Chuckanut Formation assuming coseismically formed failure planes. The seismic accelerations required to induce known landslides are in agreement with published estimates of strong ground motions in western Washington.



“A landscape, like a man or woman, acquires character through time and endurance. ”

• Edward Abbey (1927-1989)

CHAPTER 6. SPATIAL AND TEMPORAL CONTROLS ON ROCK MASS STRENGTH AND LANDSCAPE DEVELOPMENT

Material properties (friction angle and cohesion) are classically obtained through laboratory testing of intact or remolded earth material. In **contrast** to the commonly used laboratory methods applied to determine material properties (simple, **triaxial**, and direct shear tests), this study examines topographic development and outcrop characteristics to estimate strength of the total rock mass. At the **hillslope** scale, **landform** profiles and topographic development were used **as** an expression of material strength to back-calculate regional-scale strength properties (Chapter 3). Additionally, **rock mass** strength estimates obtained at the outcrop scale and interpolated to the surrounding hillslope were used to gain insight into the specific rock mass characteristics governing **hillslope** strength (Chapter 4). Relative strength was estimated by the distribution of deep-seated landslides within a landscape. Controls on the occurrence of deep-seated **landslides** can be thought of as being deterministic, that is a mechanical correspondence exists between determining cause and effect. For example, seismic accelerations distributed in space, time, and magnitude; weathering, often concentrated within specific geologic units; spatially variable rock strength properties; and **glacial** and **fluvial** erosion generating relief all have predictable influences on landscape development. That is, material strength is determined by preceding events and natural laws. Landscape evolution and the two leading categorical influences on material strength, space and time, are discussed in the following chapter.

SPATIAL INFLUENCE

Sample Size

As discussed in Chapter 3, material properties obtained through topographic analysis of natural hillslopes are lower than typical values derived from laboratory measurements on similar materials (Tables 3-1 and 3-2). This discrepancy in apparent strength is partially rooted in the influence of length scale and the fact that rock masses are

discontinua. Rock strength is size dependent. For example, Bieniawski and Van Heerden (1975) report that the experimentally determined strength of iron ore, diorite, and coal decreases considerably with increasing specimen size. Similarly, the results of strength tests carried out by **Jahns** (1966) showed that specimen strength depends strongly upon size. **Jahns** determined that a 0.1 m cube of iron ore had an *in situ* **uniaxial** compressive strength of 117 **MPa** while a 1 m cube had a strength of only 49 **MPa**. Separate experimentation by Richter (1968) also using iron ore samples concluded that the *in situ* strength was 18 times lower than laboratory-derived estimates of strength. Results from Pratt et al. (1972) disclose that *in situ* and laboratory tests on specimens of quartz diorite ranging in size from 2 in (5.1 cm) to 9 ft (2.74 m) in length indicate that maximum stress decreases by a factor of ten with increasing specimen size.

It is believed that the apparent decrease in strength with increasing sample size is a function of discontinuity concentration. Smaller-sized samples contain fewer macroscale discontinuities, and hence are evidently stronger because failure is forced to initiate new crack growth (Figure 6-1). In other words, sample size determines the total quantity and characteristic frequency of discontinuities represented. Consider discontinuities with characteristic frequencies of 1, 10, and 100 m spacing. A 5 m sample will embody only the 1 m discontinuity frequency spacing, escaping the influence of the 10 m and 100 m frequency discontinuities, thus underestimating the large-scale discontinuity concentration. Posit a strength population with a normal distribution [**Lumb** (1966) concluded that cohesion and friction angle for soil can be represented by a normal frequency distribution], a larger rock mass volume embodies a wider range of strength properties having a higher probability of intersecting both regions of extremely low and high strength (Figure 6-2). Larger samples are thus required to obtain statistically complete collections of **all** the components that influence strength. Therefore, because of their great magnitude, natural hillslopes encompass both very strong and very weak rock masses, but it is the weak links that limit topographic development and slope stability.

Because laboratory-based and *in situ* strength tests generate failure surfaces that are many orders-of-magnitude smaller in surface area than landslide failure surfaces, shearing is restricted to a small sampling of the available discontinuities and the apparent strength of the material will be overestimated. Therefore, the small samples used in laboratory tests do

not yield strength parameters directly applicable to the entire rock mass from which the samples were taken.

Back-calculated strength parameters for glacial deposits are closer to those obtained from laboratory experiments than those obtained for the Chuckanut Formation (Tables 3-1 and 3-2). Because the glacial sediments are unconsolidated and uncemented, the cohesion reduction with increased fracture density is less than a consolidated material. In addition, fractures forming within unconsolidated materials will be less pervasive because stresses are dissipated rapidly across grain boundaries or laminations.

The apparent strength decrease with increasing sample size is also expressed by a suppression of great magnitude hillslopes from the LTD defined for the entire Chuckanut Formation. That is, strength properties back-calculated from observed topography appear to decline with progressively larger hillslopes. Figure 3-13 reveals that the highest relief hillslopes plot below the average strength envelope attributed to the Chuckanut Formation as a whole. Departure from the LTD at great relief is thought to indicate that the largest magnitude hillslopes should be represented by even lower strength properties than the regional material properties back-calculated using the full spectrum of observed topographic development.

Geologic Structure

The large-scale anisotropy offered through geologic structure provides a strong control on **hillslope** strength and thus the maximum attainable topographic development. Structural influence, however, is spatially variable depending on the correlation between topography and the underlying structure. Strength anisotropy is well expressed by rock masses composed of parallel arrangements of discontinuities such as bedding. This study concluded that the highest incidence of **landsliding** in the Chuckanut Formation, a strongly bedded sequence, occurs where the angular divergence between hillslope and bedding orientation, for both strike and dip, is minimized (Figure 4-7a). Chapter 4 examines the structural controls influencing local topographic development and the degree of instability within the Chuckanut Formation. For stable **hillslopes** there is no correlation of the apparent dip divergence between the bedding plane and the hillslope gradient (Figure 4-5a). In contrast, over 75% of the landslide sites have apparent bedding dips oriented within

$\pm 20^\circ$ of the hillslope gradient (Figure 4-5b). Roughly slope-parallel bedding is most susceptible to failure.

A similar examination of apparent dip divergence for primary joint sets indicates no correlation of angular relationships between joint orientation and topography for both stable and unstable sites (Figures 4-6a & b). The orientation of the discontinuity, either bedding plane or joint, with respect to the hillslope orientation can be effectively represented through the rock mass strength classification scheme detailed in Chapter 4. Thus, the distribution of discontinuity planes within a landscape produces a quantifiable influence on hillslope stability with bedding planes acting as the primary control while jointing plays only a secondary role if any in the stability of the Chuckanut Formation.

TEMPORAL INFLUENCE

Stress Rate

Scale issues are also manifest in the comparison of natural hillslope deformation rates versus deformation rates imposed during laboratory strength testing procedures because the stress-strain relation, E , (Young's modulus) is dependent on the applied stress rate. For example, stress rates are many orders-of-magnitude greater in laboratory strength testing experiments than in the natural deformation of a **hillslope**. Data from John (1974) for **norite**, a basic igneous intrusive rock, shows that strength falls when the stress rate is slowed. A **norite** specimen loaded to peak stress at 2.1 **MPa/s** (over about 100 hr) developed about two-thirds of the strength of a specimen loaded to peak stress at 1.8 **MPa/s** (over about a twentieth of a second). Taylor (1948) and **Terzaghi** (1955) have shown that the shear strength of clays decreases with increasing time of applied shear. Schmidtke and **Lajtai** (1985) report that the time-dependence of the uniaxial compressive strength of a granite may be represented by an exponential strength decay with time. Sustained compressive loading experiments on granite and anorthosite lasting up to seventeen days led **Lajtai** and Schmidtke (1986) to estimate that in a humid environment the long-term strengths of crystalline rocks could be less than 60% of their dry instantaneous strengths. If the material is strain-sensitive, the peak strength occurs at a small strain with a considerable subsequent drop to the residual strength at large strains. During the course of

deformation, the integrity of the rock is gradually destroyed and thus the material strength would **be** regarded as time-dependent.

Back-calculated glacial deposit strength parameters are in closer agreement to those obtained from laboratory experiments than those obtained for the Chuckanut Formation. This disparity may reflect the hypothesized time-dependence of strength properties. In comparison with the Eocene Chuckanut Formation, the stress rates acting upon the Quaternary glacial deposits operate on time scales closer to those replicated in strength testing experiments. Forces destabilizing Quaternary glacial sediments are largely controlled by rates of valley incision and lateral migration of channels incising into the glacial sediments. It is estimated that these processes serving to increase the relief and/or gradient of glacial deposit landforms function on the scale of seasons to thousands of years. In contrast, stress rates in bedrock are driven by rates of large-scale topographic development which are thought to operate on time scales of thousands to millions of years.

Weathering

The consequences of weathering, both physical and chemical, on material properties serve to preferentially reduce cohesive over frictional strength. While **back-**calculated friction angle values are only slightly lower than those obtained from laboratory tests, cohesion values are substantially diminished (Tables 3-1 and 3-2). These results are supported by Cripps and Taylor (198 1). They report that the weathering of **mudrocks** is characterized by a several order-of-magnitude reduction of cohesion with a lesser reduction in friction angle. The pronounced decrease in cohesion arises as the structural integrity of a rock is diminished through weathering and fracturing into smaller pieces (Mencl, 1965). Therefore, high cohesion values are to be expected for intact, unweathered rock samples, whereas in highly fractured materials the aggregate properties may be expected to reflect those of the weakest link in the mass.

Weathering commonly involves the breakdown of chemically unstable constituents leading to an increase in the relative clay content, water content, plasticity, and compressibility with accompanied reductions in strength. The extent or maturity of weathering is dependent on the initial material composition, climate, vegetation, and

exposure time. Overall, though, a longer exposure to weathering processes leads to more advanced weathering products and a subsequent decrease in strength.

The Darrington Phyllite exhibits varying degrees of strength depending on its extent of weathering. Whereas analysis of the strongly bedded Chuckanut Formation revealed that stability is highly dependent on geologic structure, examination of slopes underlain by Darrington Phyllite suggests that the degree of weathering dramatically alters material strength. Rock comprising the inner gorge is subjected to enhanced fracture intensity through mechanical weathering induced by the local topographic stress field (Miller, 1993). Greater fracture density allows for increased hydraulic conductivity and intensified chemical weathering. **In** addition, rock within valley floors such as an inner gorge are subject to focusing of groundwater flow (Freeze and Cherry, 1979). Consequently, rock comprising the inner gorge is well weathered and fails at much lower reliefs, for a given hillslope gradient, than the same unweathered rock (Figure 3-15) above the groundwater flow **field**. Thus, rock strength predictably varies through the landscape as exposure time to conditions conducive to advanced weathering increases, with inner gorges identified as sites possessing weathered, weak rock conducive to extensive landsliding.

Earthquakes

Although the downward oriented acceleration of gravity is commonly the primary force acting on a landscape, accelerations of a dynamic nature arising from earthquakes serve to dramatically decrease hillslope stability. Even though ground disturbance resulting from earthquakes may be localized along narrow zones parallel **to the** primary surface rupture, strong ground motions may affect regions hundreds-of-thousand km² in area. It is commonly recognized that an earthquake can trigger numerous landslides in a broad expanse surrounding its epicenter with larger areas affected by greater earthquake magnitudes (Keefer, 1984; Wilson and Keefer, 1985). Studies in the Puget Sound region recognizing the link between earthquakes and landslides include Keefer (1983). **Jacoby et al. (1992)**, and Schuster et al. (1992).

The long-term impact of **repeated** seismic disturbance may be highly influential in loosening rock masses **and** reducing shear resistance. Strong ground motions may extend and widen the aperture of existing fractures, initiate new fractures, and expand

groundwater flow conduits allowing for accelerated weathering. Consequently, the **long-term** additive history of piecemeal degradation due to strong ground motions recorded within a hillslope over time may be more important than the magnitude of the most recent earthquake. The work of Perkins et al. (1980) indicates that the bedrock landscape in the Pacific Northwest study area experienced at least five major earthquakes producing horizontal accelerations greater than **0.3g** since deglaciation. The integrated effects of these past earthquakes contribute incrementally to strength reduction. In contrast, **hillslopes** composed of unconsolidated Quaternary glacial deposits evolve over much shorter time scales and seismic accelerations may induce catastrophic hillslope failure as opposed to adding to cumulative strength reduction of consolidated materials.

Seismic activity may have a very important, and perhaps dominant, influence on the large-bedrock landslides in the Pacific Northwest study area by acting as a **final** triggering mechanism in addition to compounding incremental strength degradation. The relative importance of the two main landslide triggering mechanisms, hydrologic and seismic, were discussed previously. While Chapter 3 examined the relative LTD suppression under saturated conditions, Chapter 5 concluded that horizontal seismic accelerations are the most destabilizing, temporarily suppressing the LTD in proportion to the magnitude of seismic accelerations. A comparison of the seismic and hydrologic responses of the LTD for the Chuckanut Formation (Figures 3-12 and 5-7) reveals that the relative LTD suppression defined by fully saturated conditions is roughly equivalent to the LTD position for horizontal ground accelerations of **0.4g**. In the scope of long-term landscape development, the recurrence interval of ground accelerations exceeding **0.4g** may be relatively moderate and may occur at a similar frequency as storms required to saturate steep bedrock hillslopes. It is not, however, a unique driving mechanism leading to **hillslope** instability but rather the combined affects of seismic accelerations and relative degree of saturation. To test the hypothesis that the Chuckanut Formation rockslides are earthquake-induced, one could date the regional occurrence of the landslides. **If** all landslide sites have similar dates, corresponding to previously identified earthquakes in the area, circumstantial evidence may indicate a seismic triggering mechanism.

Glacial Buttresses

As discussed in Chapter 3, the present stability of some hillslopes in Figure 3- 11 greater than 750 m in relief is partially explained by the buttressing of lower valley walls with glacio-fluvial deposits. **While** only 37% of the recognized landslide sites above 750 m are buttressed with glacial sediments, 80% of the currently stable sites have thick benches of glacial sediments buttressing their lower slopes. The added mass on the valley floor decreases the overall hillslope gradient and provides a downward directed imposed load on the **hillslope** toes, thus increasing the relative stability and maximum topographic development.

In addition to a discontinuous spatial distribution of glacial deposits within valley floors, relative slope stability also decreases over time as the sedimentary deposits are removed by erosion. Valley-bottom glacial sediments provide a geologically ephemeral influence on stability because the sediments are erosionally incompetent and are removed relatively quickly over the scale of tens of thousands of years. As valley fills are evacuated, the bedrock hillslopes are unloaded and will become less stable. **Infinite-slope-**derived estimates of strength reduction with removal of glacial tills indicate that the factor of safety may be decreased by as much as 30%. This strength reduction may be sufficient to induce deep-seated landsliding. Thus, identification of currently stable buttressed sites near the LTD may be used as a predictive tool to identify sites of future instability.

LANDSCAPE EVOLUTION

Erosion appears to be concentrated where strength is lowest or alternatively where susceptibility to erosion is greatest. The selection principle in surface erosion of Scheidegger (1985) suggests that present **landforms** are statistically the most stable, being selected over time by erosional and weathering processes. Although erosion occurs in a spatially random fashion, erosive activity is greatest where strength is low. When the topography generated exceeds that sustainable by material strength, deep-seated landsliding provides a feedback mechanism that subsequently limits topographic development. In addition, deep-seated landslides produce a higher degree of three dimensional complexity in a landscape. Mass wasting in the form of deep-seated landslides does not, however, result

in a wholesale, regional decrease in relief but a piecemeal, stochastic removal of portions of the landscape serving to locally decrease slope gradients and increase valley widths.

In the context of landscape evolution, the recurrence interval of shallow, **fast-**moving debris flows operates on a much shorter time scale than deep-seated landslides. In general, debris flows **stochastically** trigger at the same location with a frequency of thousands to tens of thousands of years. The relatively short return frequency for debris flows is evidenced by the clustering of basal radiocarbon ages between 9000 and 15,000 B.P. in central coastal California (Reneau et al., 1986; Reneau et al., 1990). between **4000** and 7500 yr B.P. in southern coastal Oregon (**Benda** and Dunne, 1987; Reneau and Dietrich, 1991), and between 7200 and 12,200 yr B.P. in western Washington (Reneau et al., 1989). The grouping of basal colluvial ages apparent in California and Washington is thought to reflect the climatic change associated with the Pleistocene-Holocene transition. The time scale reflected by the return frequency of debris flows is controlled by the weathering of rock into regolith, hollow infilling rate, and climatic/hydrologic conditions,

In contrast to the processes governing debris flow frequency, the return interval of deep-seated landslides is controlled by longer term processes such as glacial cycles, isostatic rebound, base level fluctuations, incision of **fluvial** networks into bedrock, and earthquake recurrence interval. While colluvial **infilling** rates of hollows control debris flow generation, the recurrence frequency for deep-seated landslides depends on topographic development and is thought to operate on time scales of thousands to millions of years.

Where present, **deep-seated** landslides greatly alter landscape form and transport large volumes of rock. While debris flows may scour off the available colluvium removing little bedrock, deep-seated landslides transport large volumes of bedrock in addition to the overlying thin mantle of colluvium and may be the dominant sediment source of a **fluvial** network. Both mass wasting processes assist with incision of the channel network and fixing of the drainage density, but in the short term after failure, deep-seated landslides may entirely obliterate and reshape portions of **fluvial** networks.

In **orogenic** belts, relief is developed when either surface uplift across some boundary (i.e. a fault) exceeds exhumation or when channel networks are incised into the

crust. As **hillslope** relief increases, the base length remains essentially constant relative to the vertical change in height. The characteristic V-shape of most unglaciated valleys in high relief landscapes reflects the relation that vertical valley incision and the subsequent increase in **hillslope** relief is greater than the magnitude of valley width increase. As relief and hillslope gradient attain some threshold value, further vertical valley incision induces **deep-seated** landsliding which **serves as** a feedback mechanism to limit continued relief development. Once the maximum material strength is mobilized, exhumation holds the landscape in a state of dynamic equilibrium as topographically induced stresses exceed rock strength upon further valley incision.

Furthermore, material strength of the rock mass comprising a landscape decreases over time through the generation of increased fracture concentrations and chemical degradation in response to topographically induced stresses, weathering, repeated earthquake-induced strong ground motions, and large magnitude hydrologic events. Decreases in rock mass strength over time may then trigger hillslope failure without an apparent increase in relief. Figure 6-3 schematically represents that over long periods of time, unweathered strong rock capable of sustaining high limits of topographic development (great relief and steep gradient slopes) will be transformed into highly weathered rock only capable of expressing low limits to topographic development (minor relief and gentle gradient slopes).

Figures 6-4a & b compare the actual topographic development of a landscape with the maximum limit to topographic development defined by material strength. In these hypothetical scenarios the landscape begins with a relatively low relief and gentle gradient. Channel incision serves to increase relief and **hillslope** gradient and subsequent **interfluvial** erosion results in lower levels of topographic development. Figure 6-4a depicts the case where the actual amount of topographic development (solid curve) does not approach the maximum topographic development potential (dotted curve) and deep-seated landslides are not triggered. When the magnitude of channel incision is great enough to intersect the LTD, the maximum strength of the material is mobilized and deep-seated landsliding occurs (Figure 6-4b). Continued landsliding will produce topography with shallower gradients and less relief by **translational** movements on progressively shallower landslide surfaces, expressed by a suppression of the actual topographic development from the LTD on Figure 6-4b. After the rock is weakened by weathering processes over long time periods, the

interfluves are easily eroded and the actual relief is suppressed below the potential LTD. At this time the actual topographic development is less than the LTD and renewed valley incision is required to reinstate widespread landsliding.

The climatic regime will strongly influence the relative rock mass strength and thus the potential limit to **topographic** development. For example, Figure 6-5a represents the evolution of the LTD (dotted line) for two different weathering rates. Low weathering rates allow high degrees of topographic development (**LTD₁**) over long time spans while high weathering rates produce weak rock and thus less relief and gentler hillslope gradients (**LTD₂**). High weathering rates may be indicative of moist, humid environments while low weathering rates may **represent arid** climates where physical, chemical, and biotic processes are retarded.

Limits to topographic development will also vary greatly in different tectonic regimes. Relative tectonic quiescence within a stable **craton** may constrain a landscape to a relatively uniform limit of topographic development for long periods of time (**LTD₁**) while the LTD in an active tectonic margin (**LTD₂**) is rapidly diminished (Figure 6-5b). In active **orogenic** belts, such as the Santa **Cruz** Mountains schematically illustrated by LTD₂, the topographic, geologic, and seismologic conditions are optimum for producing **earthquake**-induced landslides. Steep slopes, mechanically weak rock, and frequent large magnitude earthquakes that are stochastic both in space and time act to initiate deep-seated landsliding that subsequently acts as a feedback mechanism to limit topographic development. Ironically, the same forces that build mountain ranges through compressional deformation, often associated with large earthquakes, **may** also serve to limit the degree to which the topography can be incised.

Figures 6-4 and 6-5 illustrate that the present relief and gradient of hillslopes are a function of their environment and the degree of actual landscape incision relative to the LTD. Thus, **hillslope** gradients of an area are related **to the** local morphological history (defined by rock mass strength and erosion) and are not intrinsic features of slope development.

Figure 6- 1. Spatial distribution of discontinuities (solid black lines) varying with sample size. Depicted are 1 m², 2 m², and 4 m² cross sections of the same hypothetical sample. Greatest number of throughgoing discontinuities are recognized in largest sample.

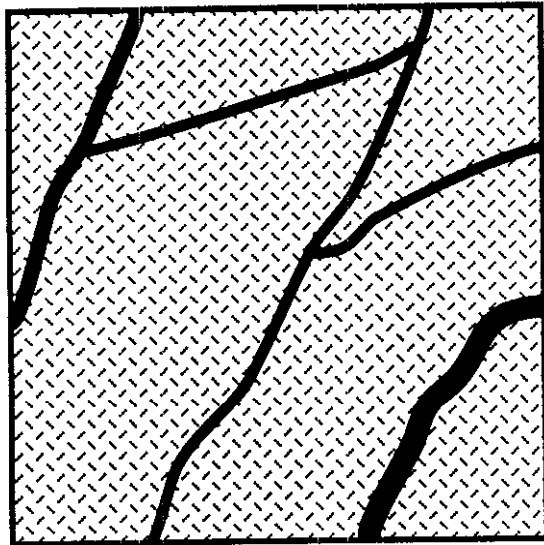
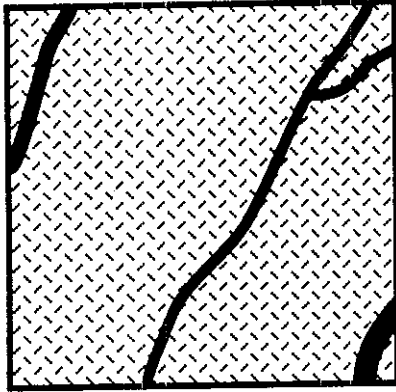
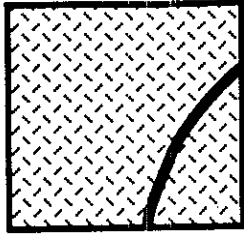


Figure 6-2. Hypothetical rock mass strength distribution. Small samples are dominated by average strength values while large samples also possess the tail ends of the strength distribution.

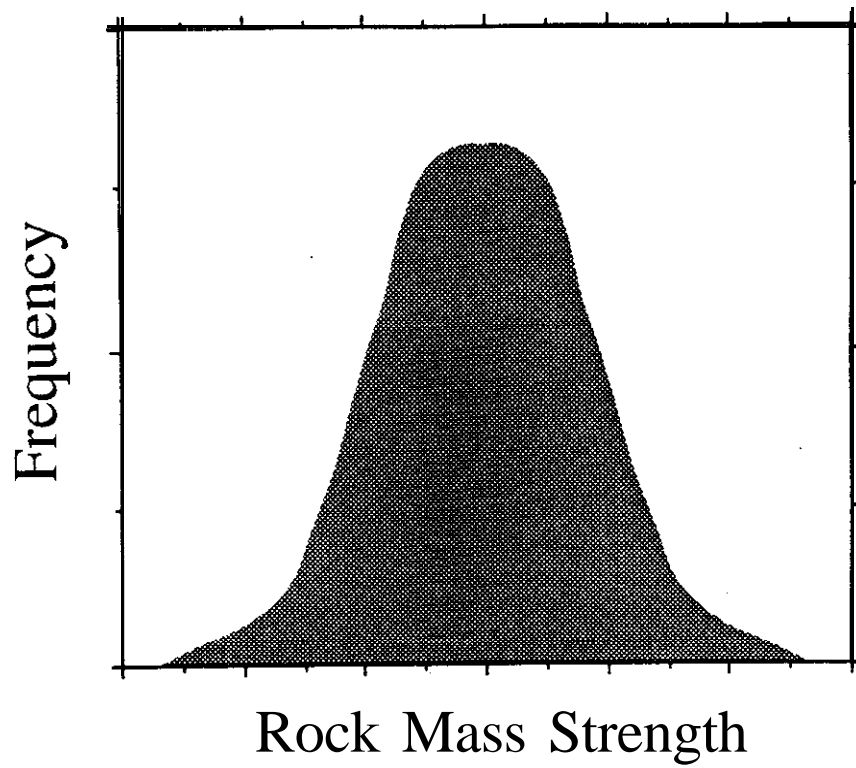


Figure 6-3. Limit to topographic development (LTD) (dotted curve), a function of hillslope relief and gradient, declines as rock strength decreases over time. Note, LTD is schematic and was not intended to represent any particular location or environment.

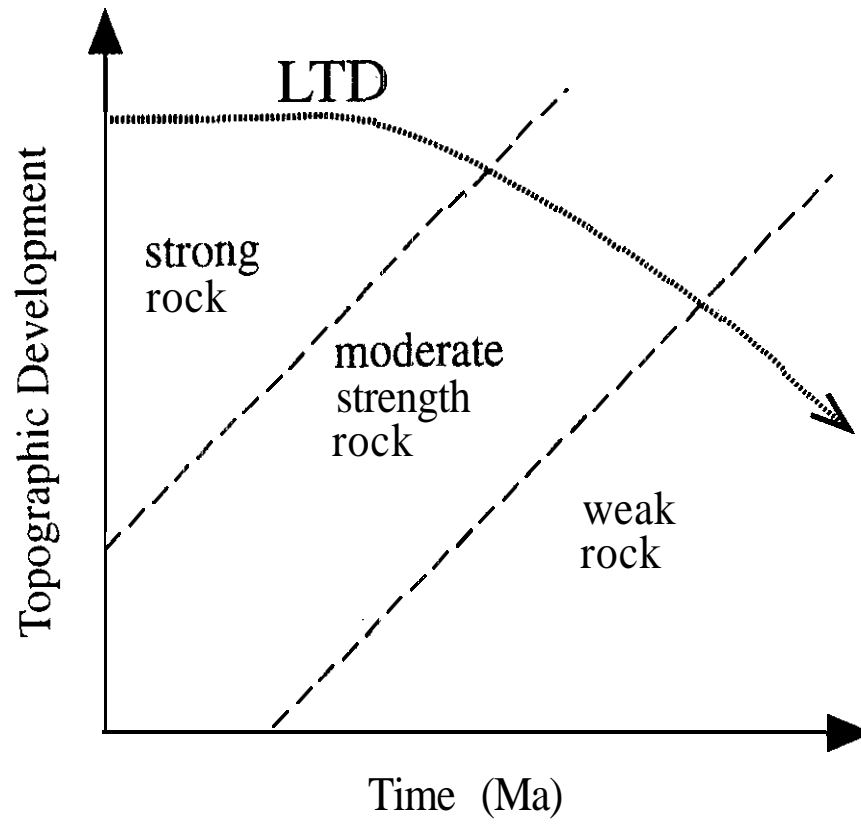


Figure 6-4. a. Limit to topographic development (LTD) (dotted curve) greater than actual topographic development (solid curve).
b. Limit to topographic development (**LTD**) (dotted curve) coinciding with actual topographic development (solid curve) and the accompanied generation of deep-seated landsliding.

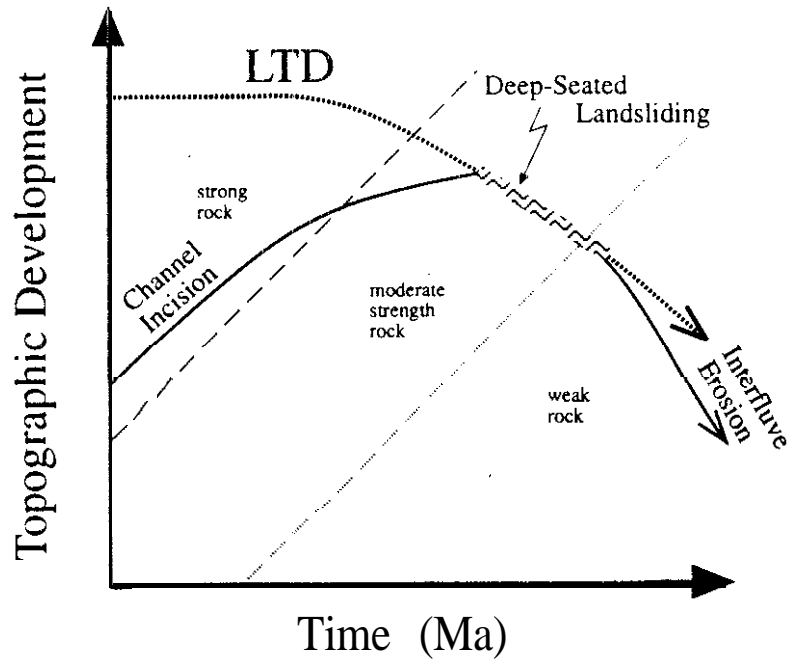
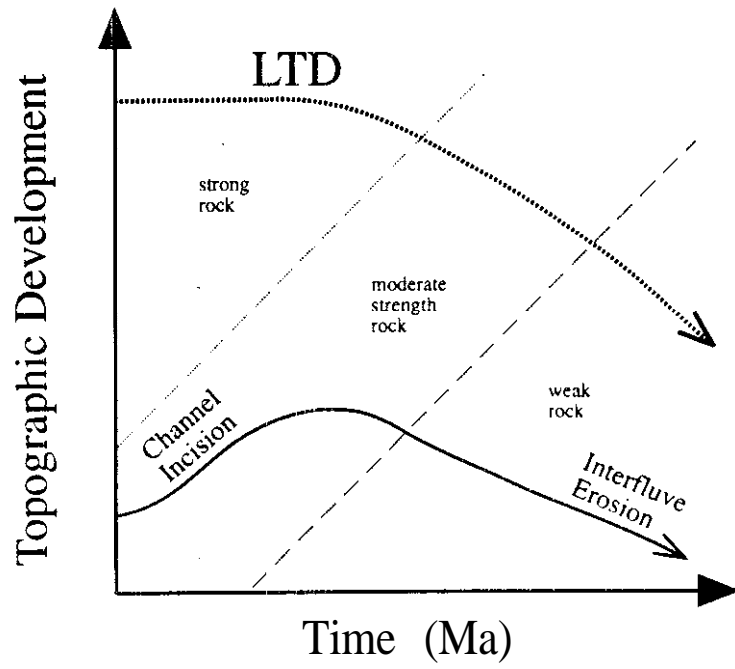
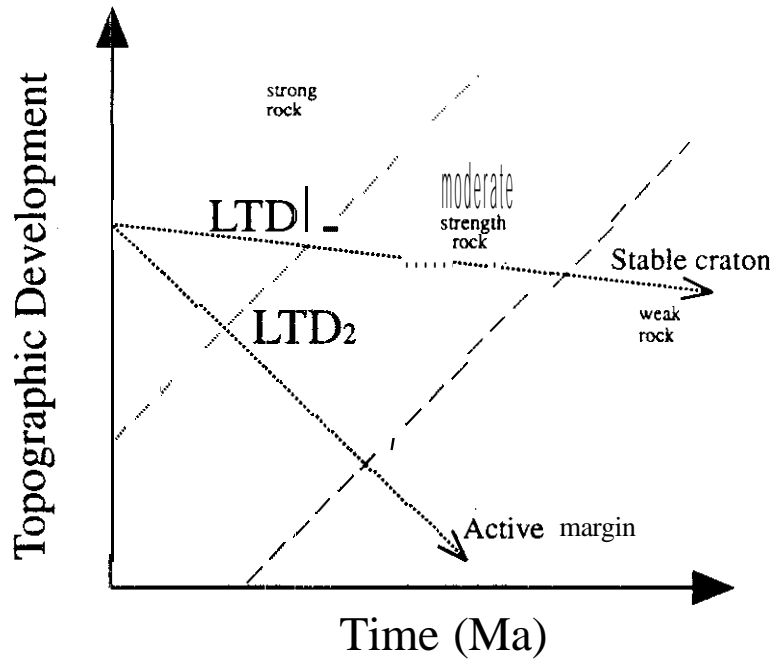
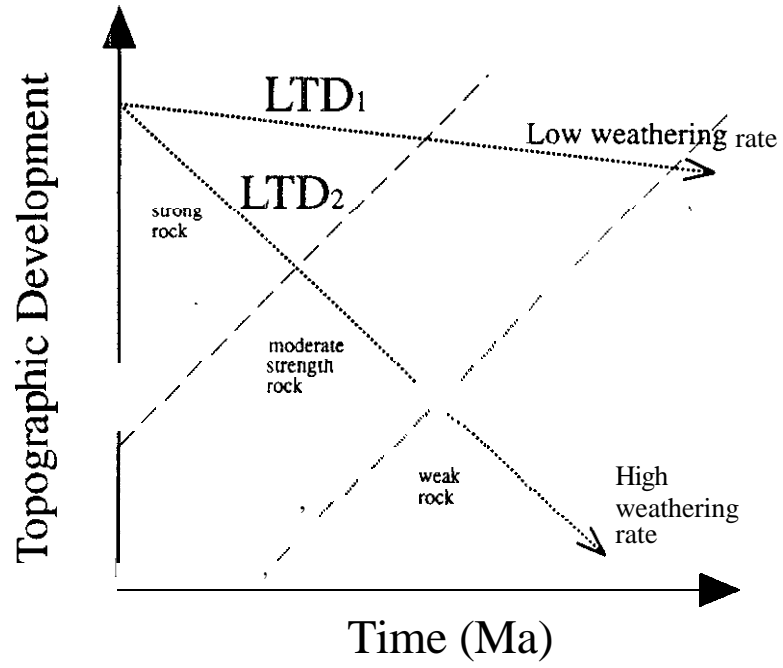


Figure 6-5. a. Limits to topographic development (**LTD**) (dotted line) for two different weathering rates. Low weathering rates allow high degrees of topographic development (**LTD₁**) over long time spans while high weathering rates produce weak rock and thus less relief and gentler hillslope gradients (**LTD₂**).

b. Limits to topographic development (**LTD**) (dotted line) for two different tectonic regimes. Relative tectonic quiescence within a stable **craton** may constrain a landscape to a relatively constant limit of topographic development for long periods of time (**LTD₁**) while the **LTD** in an active tectonic margin (**LTD₂**) is rapidly diminished.



"The direction in which education starts a man, will determine his future life. "

• Plato

CHAPTER 7. SUMMARY

The presence of widespread landsliding in a landscape implies that the full material strength is engaged and that the material composing hillslopes is not capable of supporting further increases in relief. I hypothesized that integrated rock strength properties limit local topographic development and effectively bound the size of stable hillslopes for mountain drainage basins in a given lithologic, climatic, and tectonic regime. This hypothesis was investigated using theory and field examples located in the northern Cascades of Washington state and in the Santa Cruz Mountains of California. In *situ* large-scale strength properties were back-calculated from observed topography and rock mass strength estimates at the outcrop scale were used to investigate the influence of discontinuities and seismic accelerations on landslide susceptibility and topographic development. The following chapter represents a synopsis of the conclusions reached in the preceding chapters.

LANDSCAPE EVOLUTION AND MATERIAL PROPERTIES

- The large-scale strength properties of bedrock slopes provide a limit to topographic development that links the maximum stable relief and gradient of mountains, deep-seated landsliding, and incision of the intervening valleys.
- The climatic regime will strongly influence relative rock mass strength and thus the potential limit to topographic development. Limits to topographic development will also vary greatly in different tectonic regimes.
- The geomorphic problem of defining **limits** to local topographic development and traditional engineering methods of determining material strength parameters operate at drastically different spatial and temporal scales.

- The regional application of a limit-equilibrium stability model may be used to **back-**calculate strength parameters in areas where observations of widespread landsliding indicate mobilization of the peak material strength. These back-calculated parameters provide estimates of in-situ strength that incorporate the effects of material discontinuities and transient forces (e.g. seepage forces and seismic accelerations).

BACK-CALCULATED MATERIAL PROPERTIES

Glacial Sediments

- The highest degree of instability within **Quaternary** glacial sediments is found in the apex of meander bends where banks are oversteepened and material is actively removed by **fluvial** erosion. The predicted depth of tension in a vertical bank from Rankine Theory, 3.4 m, is in excellent agreement with the value of 3.5 m measured in the **field** on the Middle Fork of the **Nooksack** River. In a predictive sense, those sites situated above the saturated threshold designated in Figure 3-6 would be most susceptible to changes in the hydrologic response of a watershed induced by land management activities.

Chuckanut Formation

- Structural control greatly influences local topographic development and the degree of instability within the Chuckanut **Formation**. Dip slopes and slopes striking parallel to the trend of fold axes lie significantly below the threshold of maximum topographic development defined by anti-dip slopes. Furthermore, buttressing of mountain fronts by glacial benches may increase the relative factor of safety of higher ridges by as much as 30%.

Darrington Phyllite

- The extent of weathering markedly influences local topographic development and slope stability within the Darrington **Phyllite**. Certain predictable locations of the landscape, such as inner gorges, experience pronounced strength degradation due to

heightened chemical weathering, ground water focusing, and mechanical weathering arising from topographic stresses.

Santa Cruz Mountains Sedimentary Units

- Back-calculated strength parameters are in close agreement with laboratory derived strength parameters. This agreement is significant because the laboratory derived parameters independently validate the process geomorphology approach adopted here. Both methods aim to characterize the nature of the weak portions of hillslopes controlling rock mass strength so the resulting strength parameters should be equivalent.

BACK-CALCULATED VS. LABORATORY DERIVED PARAMETERS

- The fact that back-calculated strength values obtained in this study are slightly lower than traditional laboratory analysis on intact rock is believed to reflect the influences of spatial and temporal variability.

Spatial Influence

- Rock strength is size dependent. It is believed that the apparent decrease in strength with increasing sample size is a function of discontinuity concentration. Small samples contain fewer macroscale discontinuities, and hence are evidently stronger because failure is forced to initiate new crack growth. Larger samples are required to obtain statistically complete collections of all the components that influence strength.
- The large-scale anisotropy offered through geologic structure provides a strong control on hillslope strength and thus maximum topographic development attainable.
- The present stability of some Chuckanut Formation hillslopes is partially explained by the buttressing of lower valley walls with glacio-fluvial deposits.

Temporal Influence

- Scale issues are also manifest in the comparison of natural hillslope deformation rates versus deformation rates imposed during laboratory strength testing procedures because the stress-strain relation, E , (Young's modulus) is dependent on the applied stress rate. For example, **stress** rates are many orders-of-magnitude greater in laboratory strength testing experiments than in the natural deformation of a **hillslope**.
- Over long periods of time, unweathered strong rock capable of sustaining high limits of topographic development (great relief and steep gradient slopes) will be transformed into highly weathered rock only capable of expressing low limits to topographic development (minor relief and gentle gradient slopes).
- The frequency of deep-seated landsliding is controlled by long term processes such as glacial cycles, isostatic rebound, base level fluctuations, incision of **fluvial** networks into bedrock, and earthquake recurrence interval.
- Back-calculated **Quaternary** glacial deposit strength parameters are in closer agreement to those obtained from laboratory experiments than those representing the much older Eocene Chuckanut Formation.
- The Darrington **Phyllite** exhibits varying degrees of strength depending on its extent of weathering. Consequently, rock comprising the inner gorge is well weathered and fails at much lower reliefs, for a given **hillslope** gradient, than the same unweathered rock (Figure 3-15) above the groundwater flow field.

ROCK MASS STRENGTH

. The RMS framework provides a means for evaluating lithologic variability and the importance of discontinuities on deep-seated landslide susceptibility and local topographic expression. The approach developed here distinguishes between stable and landslide sites such that all landslide sites **are** limited to RMS values less than 69. Analysis of the individual parameters within the scheme indicates that low RMS values for landslide sites reflect the influence of hvo factors: A) a large proportion of weak

rock, usually shale, and/or B) an unfavorable slope parallel condition of topography and geologic structure.

EARTHQUAKE-INDUCED STRONG GROUND MOTIONS

- Seismic accelerations temporarily suppress the LTD in proportion to the magnitude of seismic accelerations. Furthermore, the timing of failure plane generation (aseismic vs. coseismic) is critical to predicting the degree of LTD suppression.
- Seismic accelerations oriented horizontally are the most destabilizing with respect to landsliding and limits to topographic development.
- In addition to seismically triggered landslides, the long-term cumulative history of piecemeal degradation due to strong ground motions recorded within a hillslope over time may serve to regionally reduce material strength.
- **A** comparison of the seismic and hydrologic responses of the LTD for the Chuckanut Formation and sedimentary units of the Santa Cruz Mountains reveals that the relative LTD suppression **defined** by fully saturated conditions is roughly equivalent to the LTD position for horizontal ground accelerations of **0.4g**.

This study demonstrates that it is possible to apply simple theories to examine the constraints on the magnitude of stable hillslopes and thus the limits of topographic relief development. It has been shown that it is possible to back-calculate material strength properties based on the topographic characteristics of a landscape. As material strength spatially varies throughout a landscape, so will the maximum attainable topographic relief with steeper, greater relief **hillslopes** supported by stronger more competent lithologies. In the case of the Santa **Cruz** Mountains, the back-calculated strength properties are in close agreement with specialized sampling of layers **within** the landslide slip surfaces, the weak links in the units leading to instability. Because the back-calculated properties integrate the effects of discontinuities over large scales, they may be successfully applied in a regional deep-seated landslide hazard analysis. The rock mass strength assessment of the Chuckanut Formation indicates that the maximum sustainable topographic development, and hence the degree to which a landscape may be dissected, is controlled by numerous

factors that may be characteristic to a particular lithology. Furthermore, in a tectonically active region such as the Puget Sound the limit to topographic development may be significantly suppressed by momentous earthquake-induced strong ground motions.

REFERENCES

- Ahnert, F., 1984, Local relief and the height limits of mountain ranges: *American Journal of Science*, v. 284, p. 1035-1055.
- Anderson, R. S., 1990, Evolution of the northern Santa **Cruz** Mountains by advection of crust past a San **Andreas** fault bend: *Science*, v. 249, p. 397-401.
- Anderson, R. S. and **Menking**, K. M., 1994, The Quaternary marine terraces of Santa **Cruz**, California: Evidence for coseismic uplift on two faults: *Geological Society of America Bulletin*, v. 106, p. 649-664.
- Atwater, B. F. and Moore, A. L., 1992, A tsunami about 1000 years ago in Puget Sound, Washington: *Science*, v. **258**, p. 1614-1620.
- Aydin, A. and Page, B. M., 1984, Diverse Pliocene-Quaternary tectonics in a transform environment, San Francisco Bay region, California: *Geological Society of America Bulletin*, v. 95, p. 1303-1317.
- Barton, N., 1973, Review of a new shear-strength criterion for rock joints: *Engineering Geology*, v. 7, p. 287-332.
- Barton, N., 1978, International Society for Rock Mechanics Commission on Standardization of Laboratory and Field Tests-Suggested methods for the quantitative description of discontinuities in rock masses: *International Journal of Rock Mechanics and Mining Sciences and Geomechanics Abstracts*, v. **15**, p. 319-368.
- Barton, N., Lien, R. and Lunde, J., 1974, Engineering classification of rock masses for the design of tunnel support: *Rock Mechanics*, v. 6, p. 189-236.
- Benda**, L. and Dunne, T., 1987, Sediment routing by debris flows, *in* R. L. Beschta, T. Blinn, G. E. Ice and F. J. Swanson, ed., *Erosion and sedimentation in the Pacific rim*, IAHS Publication No. 165, p. 213-223.

Berris, S. N. and **Harr**, R. D., 1987, Comparative snow accumulation and melt during rainfall in forested and clear-cut plots in the western Cascades of Oregon: *Water Resources Research*, v. 23, p. 135-142.

Bieniawski, Z. T., 1973, Engineering Classification of Jointed Rock Masses: *Transactions of the South African Institute of Civil Engineers*, v. 15, p. 335-344.

Bieniawski, Z. T., 1989, *Engineering Rock Mass Classifications*, John Wiley and Sons, New York, 251 p.

Bieniawski, Z. T. and Van Heerden, W. L., 1975, The significance of *in situ* tests on large rock specimens: *International Journal of Rock Mechanics and Mineral Science*, v. 12, p. 101-113.

Bjerrum, L. and **Jørstad**, F. A., 1968, Stability of rock slopes in Norway, Norwegian Geotechnical Institute Publication Number 79, 11 p.

Bolt, B. A., 1988, *Earthquakes*, W.H. Freeman and Co., New York, 282 p.

Boore, D. M., **Seekins**, L. and Joyner, W. B., 1989, Peak accelerations from the 17 October 1989 Loma Prieta earthquake: *Seismological Research Letters*, v. 60, p. 151-166.

Bradley, W. C. and **Griggs**, G. B., 1976, Form, genesis, and deformation of central California wave-cut platforms: *Geological Society of America Bulletin*, v. 87, p. 433-449.

Brown, E. H., Blackwell, D. L., Christenson, B. W., Frasse, F. I., Haugerud, R. A., Jones, J. T., Leiggi, P. A., Morrison, M. L., Rady, P. M., **Reller**, G. J., Sevigny, J. H., Silverberg, D. S., Smith, M. T., Sondergaard, J. N. and Ziegler, C. B., 1987, Geologic map of the northwest Cascades, Washington: Geological Society of America, MC-6 1, scale 1:100,000.

Bucknam, R. C., Hemphill-Haley, E. and Leopold, E. B., 1992, Abrupt uplift within the past 17,000 years at Puget Sound, Washington: *Science*, v. 258, p. 1611-1614.

Carson, M. A. and **Kirkby**, M. J., 1972, Hillslope Form and Process, Cambridge University Press, London, 475 p.

Clark, J. C., Brabb, E. E. and McLaughlin, R. J., 1989, Geologic map and structure sections of the Laurel 7-1/2' quadrangle, Santa Clara and Santa Cruz Counties, California: U.S. Geological Survey Open-File Report 89-676, **scale 1:24,000**.

Cohee, B. P., Somerville, P. G. and Abrahamson, N. A., 1991, Simulated ground motions for hypothesized **M_w=8** subduction earthquakes in Washington and Oregon: Bulletin of the Seismological Society of America, v. 81, p. 28-56.

Cooper-Clark and Associates, 1975, Preliminary map of landslide deposits in Santa Cruz County: Cooper-Clark, and Associates, **scale 1:62,500**.

Crandell, D. R., 1965, The glacial history of western Washington and Oregon, *in* H. E. J. Wright and D. G. Frey, ed., The Quaternary of the United States, Princeton University Press, Princeton, N.J., p. 341-353.

Cripps, J. C. and Taylor, R. K., 1981, The engineering properties of mudrocks: Quarterly Journal of Engineering Geology, v. 14, p. 325-346.

Crosson, R. S., 1983, Review of seismicity in the Puget Sound region from 1970 through 1978, *in* J. C. Yount and R. S. **Crosson**, ed., Proceedings of Workshop XIV Earthquake hazards of the Puget Sound region, Washington, U.S. Geological Survey Open-File Report 83-19, p. 6-18.

Cruden, D. M. and Krahn, J., 1978, Frank rockslide, Alberta, Canada, *in* B. Voight, ed., Rockslides and Avalanches, 1, Elsevier Scientific, Amsterdam, p. 97-112.

Culmann, C., 1875, Die Graphische Statik, Meyer and **Zeller**, Zürich, 644 p.

Deere, D. U., 1963, Technical description of rock cores for engineering purposes: Felsmechanik und Ingenieurgeologie, v. 1, **p.** 16-22.

Easterbrook, D. J., 1979, The last glaciation of northwest Washington, in J. M. Armentrout, M. R. Cole and H. J. **TerBest**, ed., Cenozoic Paleogeography of the Western United States, Society of Economic Paleontologists and Mineralogists, Pacific Section, Los Angeles, p. 177-189.

England, P. and Molnar, P., 1990, Surface uplift, uplift of rocks, and exhumation of rocks: *Geology*, v. 18, p. 1173-1 177.

Fiksdal, A. J. and Brunengo, M. J., 1981, Forest slope stability project phase II, Washington State Department of **Ecology**, 62 p.

Freeze, R. A. and Cherry, J. A., 1979, *Groundwater*, Prentice-Hall, Inc., New Jersey, 604 p.

Goodman, R. and Bray, J., 1976, Toppling of rock slopes, Specialty conference on rock engineering for foundations and slopes, University of Colorado, Boulder, Colorado, American Society of Civil Engineers, p. 201-234.

Grant-Taylor, T. L., 1964, Stable angles in Wellington Greywacke: *New Zealand Engineering*, v. 19, p.129-30.

Griggs, G. B., Marshall, J. S., Rosenbloom, N. A. and Anderson, R. S., 1991, Ground cracking in the Santa **Cruz** Mountains, in J. E. Baldwin and N. Sitar, ed., *Loma Prieta Earthquake: Engineering Geologic Perspectives*, Special Publication 1, Association of Engineering Geologists, Sudbury, MA, p. 25-41.

Hancox, G. T., Chinn, T. J. and **McSaveney**, M. J., 1991, Immediate Report, Mt. Cook rock avalanche, 14 December 1991, New Zealand Department of Scientific and Industrial Research, File Reference **H36/942**, 15 p.

Harp, E. L. and Noble, M. A., 1993, An engineering rock classification to evaluate seismic rock-fall susceptibility and its application to the Wasatch Front: *Bulletin of the Association of Engineering Geologists*, v. 30, p. 293-3 19.

Harr, R. D., 1986, Effects of clearcutting on rain-on-snow runoff in western Oregon: a new look at old **studies**: Water Resources Research, v. 22, p. 1095-1100.

Heaton, T. H. and Hartzell, S. H., 1986, Source characteristics of hypothetical subduction earthquakes in the northwestern United States: **Bulletin** of the Seismological Society of America, v. 76, p. 675-708.

Heaton, T. H. and Hartzell, S. H., 1989, Estimation of strong motions from hypothetical earthquakes on the Cascadia subduction zone, Pacific Northwest: Pure and Applied Geophysics, v. 129, p. 131-201.

Hendron, A. J. and Patton, F. D., 1985, The Vaiont Slide, a geotechnical analysis based on new geologic observations of the failure surface, U.S. Army Engineer Waterways Experiment Station, Vicksburg, MS, Technical Report **GL-85-5**, p.

Hoek, E. and Bray, J. W., 1977, Rock Slope Engineering, Institute of Mining and Metallurgy, London, 402 p.

Iverson, R. M. and Major, J. J., 1986, Groundwater seepage vectors and the potential for hillslope failure and debris flow mobilization: Water Resources Research, v. 22, p. 1543-**1548**.

Jacoby, G. C., Williams, P. L. and Buckley, B. M., 1992, Tree ring correlation between prehistoric landslides and abrupt tectonic events in Seattle, Washington: Science, v. 258, p. **1621-1623**.

Jahns, H., 1966, Measuring the strength of rock in **situ** at an increasing scale, Proceedings of the 1st International Society of Rock Mechanics Congress, Lisbon, p. 477-482.

John, M., 1974, Time dependence of fracture processes of rock materials (in German), Third Congress of the International Society of Rock Mechanics, Denver, CO, National Academy, p. 330-335.

Johnson, S. Y., 1982, **Stratigraphy**, sedimentology, and tectonic setting of the Eocene Chuckanut Formation, northwest Washington [Ph.D.]: Seattle, University of Washington, p. 221.

Johnson, S. Y., 1984, Stratigraphy, age, and paleogeography of the Eocene Chuckanut Formation, northwest Washington: Canadian Journal of Earth Sciences, v. 21, p. 92-106.

Keefer, D. K., 1983, Landslides, soil liquefaction, and related ground failures in Puget Sound earthquakes, in J. C. Yount and R. S. Crosson, ed.. Proceedings of Workshop XIV Earthquake hazards of the Puget Sound region, Washington, U.S. Geological Survey Open-File Report 83-19, p. 280-299.

Keefer, D. K., 1984. Landslides caused by earthquakes: Geological Society of America Bulletin, v. 95, p. 406-421.

Keefer, D. K., 1991, Geologic hazards in the Summit Ridge area of the Santa Cruz Mountains, Santa Cruz County, California, evaluated in response to the October 17, 1989, Loma Prieta earthquake: report of the technical advisory group, U.S. Geological Survey Open-File Report 91-618, 427 p.

Kelsey, H. M., 1988, Formation of inner gorges: Catena, v. 15, p. 433-458.

Kojan, E. and Hutchinson, J. N., 1978, **Mayunmarca** rockslide and debris flow, Peru, in B. Voight, ed.. Rockslides and Avalanches, 1, Elsevier Scientific, Amsterdam, p. 315-361.

Lajtai, E. Z. and Schmidtke, R. H., 1986, Delayed failure in rock loaded in uniaxial compression: Rock Mechanics and Rock Engineering, v. 19, p. 11-25.

Lane, K. S., 1961, Field slope charts for stability studies, Proceedings of the Fifth International Conference on Soil Mechanics and Foundation Engineering, Paris, p. 651-655.

Leroueil, S. and Tavenas, F., 1981, Pitfalls of back-analyses, Proceedings of the Tenth International Conference on Soil Mechanics and Foundation Engineering, Stockholm, p. 185-190.

Lohnes, R. A. and Handy, R. L., 1968, Slope angles in friable loess: Journal of Geology, v. 76, p. 247-58.

Lumb, P., 1966, The variability of natural soils: Canadian Geotechnical Journal, v. 3, p. 74-97.

Manson, M. W., Keefer, D. K. and McKittrick, M. A., 1992, Landslides and other geologic features in the Santa Cruz Mountains, California, resulting from the Loma Prieta earthquake of October 17, 1989, California Division of Mines and Geology, Open-File Report 91-05, 45 p.

Matheson, D. S. and Thomson, S., 1973, Geological implications of valley rebound: Canadian Journal of Earth Science, v. 10, p. 961-978.

Matthews, W. H. and McTaggart, K. C., 1978, Hope rockslides, British Columbia, Canada, in B. Voight, ed., Rockslides and Avalanches, 1, Elsevier Scientific, Amsterdam, p. 259-275.

McGreal, W. S., 1979, Factors promoting coastal slope instability in southeast County Down, N. Ireland: Zeitschrift für Geomorphologie, v. 23, p. 76-90.

McLaughlin, R. J., Clark, J. C. and Brabb, E. E., 1988, Geologic map and structure sections of the Loma Prieta 7-1/2' quadrangle, Santa Clara and Santa Cruz Counties, California: U.S. Geological Survey Open-File Report 88-752, scale 1:24,000.

McLaughlin, R. J., Clark, J. C., Brabb, E. E. and Helley, E. J., 1991, Geologic map and structure sections of the Los Gatos 7-1/2' quadrangle, Santa Clara and Santa Cruz Counties, California, U.S. Geological Survey, Open-File Report 91-593, 50 p.

- McSaveney**, M. J., 1978, Sherman Glacier Rock Avalanche, Alaska, U.S.A., in B. Voight, ed., *Rockslides and Avalanches*, 1, Elsevier Scientific, Amsterdam, p. 197-258.
- Megahan, W. F., 1983, Hydrologic effects of clearcutting and wildfire on steep granitic slopes in Idaho: *Water Resources Research*, v. 19, p. 811-819.
- Mencl, V., 1965, Proportions of cohesion and of internal friction in the strength of rocks, Norwegian Geotechnical **Institute** Publication #61, 17-19 p.
- Miller, D. J., 1993, *Topographically Induced Stress Fields and Patterns of Bedrock Fracturing* [Ph.D.]: University of Washington, Seattle, p. 286.
- Miller, J. F., Fredrick, R. H. and **Tracey**, R. H., 1973, *Precipitation-frequency atlas of the western United States*, vol. **IX**, Washington, U.S. Department of Commerce, National Oceanic and Atmospheric Administration, 43 p.
- Moen**, W. S., 1962, *Geology and mineral deposits of the north half of the Van Zandt quadrangle, Whatcom County, Washington*, Washington Division of Mines and Geology, 129 p.
- Molnar**, P. and England, P., 1990, Late Cenozoic uplift of mountain ranges and global climate change: chicken or egg?: *Nature*, v. 346, p. 29-34.
- Montgomery, D. R., 1993, Compressional uplift in the central California Coast Ranges: *Geology*, v. 21, p. 543-546.
- Moon, B. P., 1984, Refinement of a technique for determining rock mass strength for **geomorphological** puposes: *Earth Surface Processes and Landforms*, v. 9, p. 189-193.
- Miiller, L., 1964, The rock **slide** in the Vaiont Valley: *Mechanics and Engineering Geology*, v. 2, p. 148-212.
- Nagel**, D. K. and **Mullins**, H. T., 1983, Late Cenozoic offset and uplift along the San Gregotio fault zone: central California continental margin, *Tectonics and sedimentation*

along faults of the San **Andreas** system, Sacramento, Ca, Society of Economic Paleontologists and Mineralogists Pacific Section, p. 91- 103.

Perkins, D. M., Thenhaus, P. C., Hanson, S. L., Ziony, J. I. and Algermissen, S. T., 1980, Probabilistic estimates of maximum seismic horizontal ground motion on rock in the Pacific Northwest and the adjacent outer continental shelf, U.S. Geological Survey, Open-File Report 80-47 1.39 p.

Piteau, D. R., 1973, Characterizing and extrapolating rock joint properties in engineering practice: Rock Mechanics, v. 2, p. 5-3 1.

Plafker, G. and Galloway, J. P., eds, 1989, Lessons learned from the Loma Prieta, California, Earthquake of October 17, 1989, U.S. Geological Survey Circular 1045.48 p.

Plant, N. and Griggs, G. B., 1990, Coastal landslides caused by the October 17, 1989 earthquake, Santa Cruz County, California: California Geology, v. 43, p. 75-84.

Porter, S. C., Pierce, K. L. and Hamilton, T. D., 1983, Late Wisconsin mountain glaciation in the western United States, *in* S. C. Porter, ed., Late-Quaternary Environments of the United States, vol. 1, The Late Pleistocene, University of Minnesota Press, Minneapolis, p. 71 - 111.

Pratt, H. R., Black, A. D., Brown, W. D. and Brace, W. F., 1972, The effects of specimen size on the mechanical properties of unjointed diorite: International Journal of Rock Mechanics and Mining Sciences, v. 9, p. 513-530.

Price, N. J., 1966, Fault and Joint Development in Brittle and Semi-brittle Rock, Pergamon Press, Oxford, 176 p.

Rahn, P. H., 1971, The weathering of tombstones and its relationship to the topography of New England Journal of Geological Education, v. 19, p. 112-118.

Rankine, W. J. M., 1857, On the stability of loose earth: Transactions of the Royal Society, London, v. 147, p. 9-27.

Rantz, S. E., 1971, Mean **annaul** precipitation and precipitation depth-duration-frequency data for the San Francisco Bay region, California, U.S. Geological Survey-HUD San Francisco Bay Region Environment and Resources Planning Study Basic Data Contribution **32**, **23** p.

Rasmussen, N., 1967, Washington state earthquakes 1840 through 1965: **Bulletin** of the Seismological Society of America, v. 57, p. 463-476.

Reneau, S. L. and Dietrich, W. E., 1991, Erosion rates in the southern Oregon coast range: evidence for an equilibrium between hillslope erosion and sediment yield: *Earth Surface Processes and Landforms*, v. 16, p. 307-322.

Reneau, S. L., Dietrich, W. E., Donahue, D. J., **Jull**, A. J. T. and **Rubin**, M., 1990, Late **Quaternary** history of colluvial deposition and erosion in hollows, central California Coast Ranges: *Geological Society of America Bulletin*, v. 102, p. 969-982.

Reneau, S. L., Dietrich, W. E., Dom, R. I., Berger, C. R. and **Rubin**, M., 1986, Geomorphic and paleoclimatic implications of latest Pleistocene radiocarbon dates from colluvium-mantled hollows, California: *Geology*, v. 14, p. 655-658.

Reneau, S. L., Dietrich, W. E., **Rubin**, M., Donahue, D. J. and **Jull**, A. T. J., 1989, Analysis of hillslope erosion rates using dated colluvial deposits: *Journal of Geology*, v. 97, p. 45-63.

Richter, E., 1968, **Druckversuche in situ zur** Bestimmung von Verformungs- und Festigkeitsparametern des **kluftigen** Gebirges: *Bergakademie*, v. 20, p. 721-724.

Ross-Brown, D. M., 1973, Design considerations for excavated mine slopes in hard rock: *Quarterly Journal of Engineering Geology*, v. 6, p. 315-334.

Schedlock, K. M. and Weaver, C. S., 1991, Program for Earthquake Hazards Assessment in the Pacific Northwest, U.S. Geological Survey Circular **1067**, **29** p.

Scheidegger, A. E., 1961, Theoretical Geomorphology, Springer-Verlag. Berlin, 333 p.

Scheidegger, A. E. and **Kohlbeck**, F., 1985, The selection principle in surface erosion, International Symposium on Erosion, Debris Flow and Disaster Prevention, Tsukuba, Japan, p. 285-290.

Schmidtko, R. H. and Lajtai, **E. Z.**, 1985, The long-term strength of Lac du Bonnet Granite: **International** Journal of Rock Mechanics and Mineral Sciences and Geomechanical Abstracts, v. 22, p. 461-465.

Schuster, R. L., Logan, R. L. and Pringle, P. T., 1992, Prehistoric rock avalanches in the Olympic Mountains, Washington: Science, v. 258, p. 1620-1621.

Scott, R. F., 1963, Principles of Soil Mechanics, Addison-Wesley, Reading, Mass., 550 p.

Selby, M. J., 1980, A rock mass strength classification for geomorphic purposes: with tests from Antarctica and New Zealand: Zeitschrift für Geomorphologie, v. 24, p. 3 1-5 1

Selby, M. J., 1982, Hillslope materials and processes, Oxford University Press, Oxford, 264 p.

Shakal, A. F., **DeLisle**, M. J., **Reichle**, M. S. and Darragh, R. B., 1990, Strong ground shaking from the **Loma Prieta** earthquake of 17 October 1989, and its relation to near surface geology in the Oakland area, in S. R. **McNutt** and R. H. Sydnor, ed., The **Loma Prieta** (Santa **Cruz** Mountains), California, Earthquake of 17 October 1989, Department of Conservation Division of Mines and Geology, Sacramento, CA., p. 29-46.

Sheorey, P. R., **Barat**, D., Das, M. N., Mukherjee, **K. P.** and Singh, B., 1984, Schmidt Hammer rebound data for estimation of large scale *in-situ* coal strength: International Journal of Rock Mechanics and Mining Sciences and Geomechanics Abstracts, v. 21, p. 39-42.

Simon, A., 1989, Shear-strength determination and stream-bank instability in loess-derived alluvium, West Tennessee, USA, *in* E. F. J. DeMulder and B. P. Hageman, ed., Applied Quaternary Research, Balkema, Rotterdam, p. 129- 146.

Simon, A. and Hupp, C. R., 1992, Geomorphic and vegetative recovery processes along modified stream channels of **west Tennessee**, U.S. Geological Survey Open-File Report 9 1-502, 142 p.

Sitar, N., 1991, Earthquake-induced landslides in coastal bluffs and marine terrace deposits, in J. E. Baldwin and N. Sitar, ed., **Loma Prieta Earthquake: Engineering Geologic Perspectives**, Special Publication 1, Association of Engineering Geologists, Sudbury, MA, p. 75-82.

Skempton, A. W., 1953, Soil Mechanics in relation to geology: Proceedings of the Yorkshire Geological Society, v. 29, p. 33-62.

Spangler, M. G., 1960, Soil Engineering, International Textbook Co., New York, 483 p.

Spittler, T. E. and Harp, E. L., 1990, **Preliminary** map of landslide features and coseismic fissures in the Summit Road area of the Santa Cruz Mountains triggered by the **Loma Prieta** earthquake of October 17, 1989, U.S. Geological Survey Open-File Report **90-688**, scale 1:4,800 p.

Spittler, T. E., Harp, E. L., Keefer, D. K., Wilson, R. C. and Sydnor, R. H., 1990, Landslide features and other coseismic fissures triggered by the **Loma Prieta** earthquake, central Santa Cruz Mountains, California, *in* S. R. McNutt and R. H. Sydnor, ed., **The Loma Prieta (Santa Cruz Mountains), California, Earthquake of 17 October 1989**, p. 59-66.

Sydnor, R. H., Griggs, G. B., Weber, G. E., McCarthy, R. J. and Plant, N., 1990, Coastal bluff landslides in Santa Cruz County resulting from the **Loma Prieta** earthquake of 17 October 1989, in S. R. McNutt and R. H. Sydnor, ed., **The Loma Prieta (Santa Cruz Mountains), California, Earthquake of 17 October 1989**, Department of Conservation Division of Mines and Geology, Sacramento, CA, p. 67-82.

Taber, J. J. and Smith, S. W., 1985, Seismicity and focal mechanisms associated with the subduction of the Juan de Fuca plate beneath the Olympic Peninsula, Washington: Bulletin of the Seismological Society of America, v. 75, p. 237-249.

Taylor, D. W., 1937, Stability of earth slopes: Journal of the Boston Society of Civil Engineers, v. 24, p. 337-86.

Taylor, D. W., 1948, Fundamentals of Soil Mechanics, John Wiley and Sons, Inc., New York, 700 p.

Tetzgahi, K., 1943. Theoretical Soil Mechanics, John Wiley and Sons, Inc., New York, 510 p.

Terzaghi, K.. 1955, Influence of geological factors on the engineering properties of sediments: Economic Geology, Fiftieth Anniversary Volume 1905-1955, v. p. 557-618,

Terzaghi, K.. 1962. Stability of steep slopes on hard unweathered rock: *Géotechnique*, v. 12, p. 251-270.

Terzaghi. K. and Peck. R. 5.. 1948, Soil Mechanics in Engineering Practice, John Wiley & Sons, Inc.. New York. 423 p.

Thorson, R. M.. 198 I. Isostatic effects of the last glaciation in the Puget Lowland, Washington. U.S. Geological Survey Open-File Report 81-370, 100 p.

U.S. Geological Survey Staff. 1990, The Loma Prieta. California, earthquake: An anticipated event: *Science*, v. 247, p. 286-293.

Voight, B., 1978. Lower Gros Ventre slide, Wyoming, U.S.A., in B. Voight, ed., Rockslides and Avalanches, 1, Elsevier Scientific, Amsterdam, p. 113-166.

Voight, B. and Pariseau, W. G., 1978, Rockslides and avalanches: an introduction, *in* B. Voight, ed., Rockslides and Avalanches, 1, Elsevier Scientific, Amsterdam, p. 1-67.

Vonheeder, E. R., 1975, Coal reserves of Whatcom County, Washington, Washington Division of Geology and Earth Resources, Open File Report 75-9, 86 p.

Wagner, D. L., 1990, Geologic and tectonic setting of the epicentral area of the Loma Prieta earthquake, Santa Cruz Mountains, central California, *in* S. R. McNutt and R. H. Sydner, ed., The Loma Prieta (Santa Cruz Mountains), California, Earthquake of 17 October 1989, Department of Conservation Division of Mines and Geology Special Report 104, p. I-10.

Wagner, D. L., Bortugno, E. J. and McJunkin, R. D., 1990, Geologic map of the San Francisco-San Jose quadrangle: California Department of Conservation, Division of Mines and Geology, Map No. 5A, scale: 1,250,000.

Waitt, R. B. J. and Thorson, R. M., 1983, The Cordilleran ice sheet in Washington, Idaho, and Montana, *in* S. C. Porter, ed., Late-Quaternary Environments of the United States, vol. 1, The Late Pleistocene, University of Minnesota Press, Minneapolis, p. 53-70.

Weber, G. E. and Nolan, J. M., 1989, Landslides and associated ground failure in the epicentral region of the October 17, 1989, Loma Prieta earthquake, Weber and Associates, Program Element 4A, 17 p.

Wu, T. H., 1966, Soil Mechanics, Allyn and Bacon, Inc., Boston, 431 p.

“Nature is indifferent towards the difficulties it causes to a mathematician.”

• Fourier

APPENDIX A. RANKINE THEORY AND DEPTH OF TENSION IN A VERTICAL FACE

The following derivations use the theory of an active Rankine stress state to relate the depth of tension and the stress state close to a level ground surface to material properties. For the case of a vertical face, $\beta=90^\circ$, the maximum depth of tension, Z_c , can be determined where the lateral stress, σ_3 , is zero while σ_2 and σ_1 arise from the weight of the near surface materials. The Mohr stress circle (Figure 2-1) provides the equations for the shear and normal forces:

$$\tau = \left(\frac{\sigma_1 - \sigma_2}{2} \right) \sin 2\alpha \quad (\text{A-1})$$

$$\text{a n d } \sigma = \left(\frac{\sigma_1 + \sigma_2}{2} \right) + \left(\frac{\sigma_1 - \sigma_2}{2} \right) \cos 2\alpha \quad (\text{A-2})$$

where $\tau = c + \sigma \tan \phi$ defined by the Navier-Coulomb criterion

$$\left(\frac{\sigma_1 - \sigma_2}{2} \right) \sin 2\alpha = c + \left[\left(\frac{\sigma_1 + \sigma_2}{2} \right) + \left(\frac{\sigma_1 - \sigma_2}{2} \right) \cos 2\alpha \right] \tan \phi$$

Using the trigonometric identities, $\sin 2\alpha = 2 \sin \alpha \cos \alpha$ and $\cos 2\alpha = \cos^2 \alpha - 1$

$$(\sigma_1 - \sigma_2) \sin \alpha \cos \alpha = c + \left[\left(\frac{\sigma_1 + \sigma_2}{2} \right) + 2 \left(\frac{\sigma_1 - \sigma_2}{2} \right) \cos^2 \alpha - \left(\frac{\sigma_1 - \sigma_2}{2} \right) \right] \tan \phi$$

$$(\sigma_1 - \sigma_2) \sin \alpha \cos \alpha = c + [\sigma_2 + (\sigma_1 - \sigma_2) \cos^2 \alpha] \tan \phi$$

$$(\sigma_1 - \sigma_2) (\sin \alpha \cos \alpha - \cos^2 \alpha \tan \phi) = c + \sigma_2 \tan \phi$$

$$(\sin \alpha \cos \alpha - \cos^2 \alpha \tan \phi) = \frac{c + \sigma_2 \tan \phi}{(\sigma_1 - \sigma_2)} \quad (A-3)$$

The failure plane then has an angle α that minimizes the value of σ_2 for a given value of σ_1 . In equation A-3, σ_2 is minimized when the left hand side of the equation is a maximum. Therefore, the critical value of α is determined by setting:

$$\frac{d}{d\alpha}(\sin \alpha \cos \alpha - \cos^2 \alpha \tan \phi) = 0$$

$$\text{So, } \cos^2 \alpha - \sin^2 \alpha + 2 \tan \phi \sin \alpha \cos \alpha = 0$$

$$\text{where } \cos^2 \alpha - \sin^2 \alpha = \cos 2\alpha \quad \text{and} \quad 2 \sin \alpha \cos \alpha = \sin 2\alpha$$

$$\text{and } \cos 2\alpha + \tan \phi \sin 2\alpha = 0$$

$$\frac{\cos 2\alpha}{\sin 2\alpha} \tan \phi = -1$$

$$\frac{1}{\tan 2\alpha} = -\tan \phi$$

$$\text{Or, } \alpha = 45^\circ + \frac{\phi}{2} \quad (A-4)$$

Substituting equation A-4 into A-3,

$$\sigma_2 = \sigma_1 \tan^2 \left(45^\circ - \frac{\phi}{2} \right) - 2c \tan \left(45^\circ - \frac{\phi}{2} \right)$$

$$\text{At the ground surface, } \sigma_1 = 0, \quad \text{so } \sigma_2 = -2c \tan \left(45^\circ - \frac{\phi}{2} \right) \quad (A-5)$$

At some depth, the tension of the lateral force is zero, $\sigma_2 = 0$

So, $\sigma_1 \tan^2\left(45^\circ - \frac{\phi}{2}\right) = 2c \tan\left(45^\circ - \frac{\phi}{2}\right)$ where σ_1 is given by ρgH or γH

Therefore, $Z_c = \frac{2c}{\gamma} \tan\left(45^\circ + \frac{\phi}{2}\right)$ (A-6)

Figure 2-2 and equation A-5 demonstrate that σ_2 is negative (a state of tension) down to a critical depth, Z_c , which depends on the cohesion, friction angle, and specific weight of the material. Equation A-6 (2-2 in text), in turn, determines the maximum depth of tension in a vertical mass knowing the same material properties. For further discussion of Rankine theory see Wu (1966).

APPENDIX B. CULMANN MODEL

The following derivations are used in the stability analysis **first** presented by Culmann (1875). Subsequent references discussing the Culmann analysis include Spangler (1960); Terzaghi **and** Peck (1967); Lohnes and Handy (1968); and Carson and Kirkby (1972).

Conditions for failure in this analysis include a headscarp in the upper slope surface, a planar failure surface, and a **hillslope** inclination steeper than the failure plane ($\beta > \alpha$).

The shear stress acting on a failure plane due to weight of block is:

$$\tau = W \sin \alpha \quad (\text{B-1})$$

Shear strength, S , along the failure plane is composed of the cohesion, cA , plus the frictional component, $W \cos \alpha \tan \phi$, where $W \cos \alpha$ is the normal force, c is cohesion, and A is the strip of unit width on the failure plane over which cohesion acts.

so,
$$S = cA + W \cos \alpha \tan \phi \quad (\text{B-2})$$

(general condition: $S = c + \sigma \tan \phi$)

The factor of safety is then,
$$F = \frac{S}{\tau} = \frac{cA + W \cos \alpha \tan \phi}{W \sin \alpha}$$

$$= \frac{cA}{W \sin \alpha} + \cot \alpha \tan \phi$$

At limiting equilibrium the shear force equals the shear strength,

$$\tau = S = W \sin \alpha = cA + W \cos \alpha \tan \phi$$

or,
$$W(\sin \alpha - \cos \alpha \tan \phi) = cA \quad (\text{B-3})$$

Figure App-1 depicts the dimensions of the failure wedge with length, A , of unit width and wedge thickness, p . The weight of the failure block is then,

$$W = \frac{1}{2} p A \gamma \quad (\text{B-4})$$

where

$$\gamma = \rho g$$

and

$$\sin(\beta - \alpha) = \frac{p}{l}$$

where l is the hillslope length measured parallel to the hillslope surface.

$$p = l \sin(\beta - \alpha)$$

$$l = \frac{H}{\sin \beta}$$

Substituting into B-4,

$$W = \frac{1}{2} \left(\frac{H \sin(\beta - \alpha) A \gamma}{\sin \beta} \right) \quad (\text{B-3})$$

Combing B-3 and B-5,

$$\frac{1}{2} \left(\frac{H \sin(\beta - \alpha) A \gamma}{\sin \beta} \right) (\sin \alpha - \cos \alpha \tan \phi) = cA$$

Solving for height,

$$H = \frac{2cA \sin \beta}{[\sin(\beta - \alpha) A \gamma] (\sin \alpha - \cos \alpha \tan \phi)}$$

At limiting stability, $H=H_c$

$$H_c = \frac{2c}{\gamma} \frac{\sin \beta}{[\sin(\beta - \alpha)] (\sin \alpha - \cos \alpha \tan \phi)} \quad (\text{B-6})$$

The actual shear stress along A for the general condition is $S = \frac{c}{F} + \frac{\sigma}{F} \tan \phi$ where F is the factor of safety. At limiting equilibrium, $F=1$. Consider failure planes oriented at increasing inclinations α . As α is increased, F decreases. Thus, S increases to a maximum value when $F=1$. The shear resistance then along any potential failure plane is a function of the angle α . This is true for the individual strength parameters c and ϕ as well.

For cohesion, $c_d = f(\alpha)$ where c_d is the amount of cohesion actually developed over the potential failure plane. The value of the developed cohesion, where $c_d = \frac{c}{F}$, is maximized when the factor of safety with respect to cohesion is unity. The function $\frac{dc_d}{d\alpha}$ is then determined and set equal to zero to obtain the value of α for which c_d is a maximum.

In equation B-6 replace c with c_d ,

$$H_c = \frac{2c_d}{\gamma} \frac{\sin \beta}{[\sin(\beta - \alpha)](\sin \alpha - \cos \alpha \tan \phi)}$$

Let $u = \frac{1}{2} \frac{H\gamma}{\sin \beta}$ and solve for c_d .

$$c_d = u \sin(\beta - \alpha)(\sin \alpha - \cos \alpha \tan \phi)$$

Differentiate.

$$\frac{dc_d}{d\alpha} = \frac{d}{d\alpha} [u \sin(\beta - \alpha)(\sin \alpha - \cos \alpha \tan \phi)]$$

Expanding.

$$\frac{dc_d}{d\alpha} = \frac{d}{d\alpha} [u(\sin \beta \cos \alpha \sin \alpha - \sin \beta \cos^2 \alpha \tan \phi - \cos \beta \sin^2 \alpha + \cos \beta \sin \alpha \cos \alpha \tan \phi)]$$

where $\sin(\beta - \alpha) = \sin \beta \cos \alpha - \cos \beta \sin \alpha$

so,

$$\frac{dc_d}{d\alpha} = u[\sin\beta\cos^2\alpha - \sin\beta\sin^2\alpha + 2\sin\beta\tan\phi\cos\alpha\sin\alpha - 2\cos\beta\sin\alpha\cos\alpha + \cos\beta\tan\phi\cos^2\alpha - \cos\beta\tan\phi\sin^2\alpha]$$

Condensing terms,

$$\frac{dc_d}{d\alpha} = u[(\sin\beta + \cos\beta\tan\phi)(\cos^2\alpha - \sin^2\alpha) + 2\sin\alpha\cos\alpha(\sin\beta\tan\phi - \cos\beta)]$$

Setting $\frac{dc_d}{d\alpha} = 0$

where $\sin 2\alpha = 2\sin\alpha\cos\alpha$ and $\cos 2\alpha = \cos^2\alpha - \sin^2\alpha$

so, $0 = \cos 2\alpha(\sin\beta + \cos\beta\tan\phi) + \sin 2\alpha(\sin\beta\tan\phi - \cos\beta)$

$$\cos 2\alpha(\sin\beta + \cos\beta\tan\phi) = \sin 2\alpha(\cos\beta - \sin\beta\tan\phi)$$

$$\frac{\sin 2\alpha}{\cos 2\alpha} = \frac{\sin\beta + \cos\beta\tan\phi}{\cos\beta - \sin\beta\tan\phi}$$

$$\tan 2\alpha = \frac{\sin\beta + \cos\beta\tan\phi}{\cos\beta - \sin\beta\tan\phi}$$

$$\tan 2\alpha = \frac{\tan\beta + \tan\phi}{1 - \tan\beta\tan\phi} = \tan(\beta + \phi) \text{ by trigonometric identities}$$

so, $\tan 2\alpha = \tan(\beta + \phi)$

$$2\alpha = (\beta + \phi)$$

The inclination of the failure plane which maximizes cohesion is:

$$\alpha = \frac{1}{2}(\beta + \phi) \tag{B-7}$$

In the limiting case of a vertical face, $\beta = \frac{\pi}{2}$,

equation B-7 yields $\alpha = \frac{\pi}{4} + \frac{\phi}{2}$

Substituting equation B-7 into B-6,

$$H_c = \frac{2c}{\gamma} \frac{\sin \beta}{\sin\left(\beta - \frac{\beta}{2} - \frac{\phi}{2}\right) \left[\sin\left(\frac{\beta + \phi}{2}\right) - \cos\left(\frac{\beta + \phi}{2}\right) \tan \phi \right]}$$

and $\tan \frac{\sin \phi}{\cos \phi}$

$$H_c = \frac{2c}{\gamma} \frac{\sin \beta \cos \phi}{\sin\left(\frac{\beta - \phi}{2}\right) \left[\sin\left(\frac{\beta + \phi}{2}\right) \cos \phi - \cos\left(\frac{\beta + \phi}{2}\right) \sin \phi \right]}$$

Using the trigonometric identity, $\sin(\beta - \phi) = \sin \beta \cos \phi - \cos \beta \sin \phi$

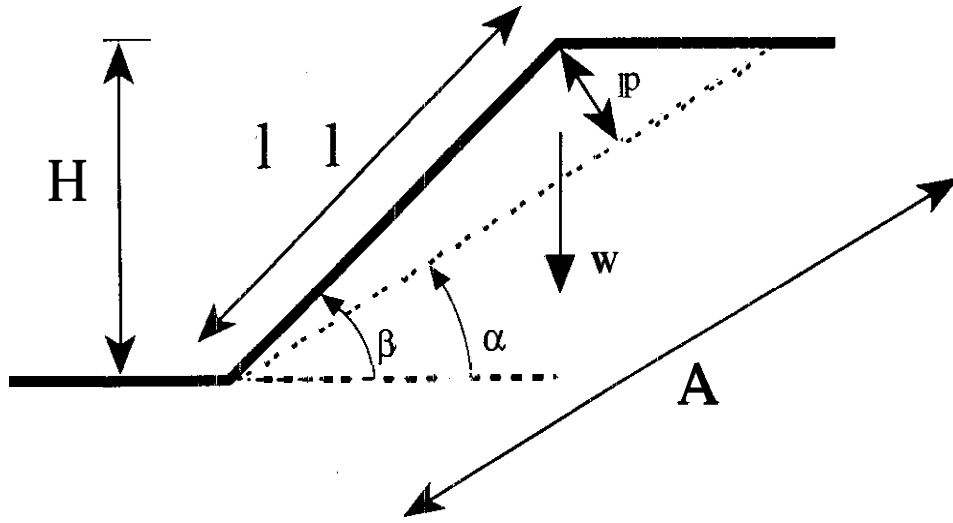
$$H_c = \frac{2c}{\gamma} \frac{\sin \beta \cos \phi}{\sin\left(\frac{\beta - \phi}{2}\right) \left[\sin\left(\frac{\beta + \phi}{2} - \phi\right) \right]}$$

$$H_c = \frac{2c}{\gamma} \frac{\sin \beta \cos \phi}{\sin^2\left(\frac{\beta - \phi}{2}\right)} \quad \text{where} \quad 2 \sin^2\left(\frac{\beta - \phi}{2}\right) = 1 - \cos 2\left(\frac{\beta - \phi}{2}\right)$$

So,
$$H_c = \frac{4c}{\gamma} \frac{\sin \beta \cos \phi}{[1 - \cos(\beta - \phi)]} \quad (\text{B-8})$$

Equation B-8, equation 2-3 in text, expresses the critical height of a hillslope in terms of the hillslope geometry and material properties.

Figure App- 1. Idealized hillslope form with relief, H , inclination angle, β , and length, l . The Culmann method defines a failure plane, dashed line, inclined at angle α to the horizontal with a length A of unit width. The failed wedge has a thickness of p and weight W acting on the center of mass.



APPENDIX C. HOEK AND BRAY MODEL

The following equations are used in the plane failure analysis presented in chapter 7 of Hoek and Bray (1977).

Two failure block geometries are considered: (See Figure 2-4)

- 1) Tension crack in upper hillslope surface
- 2) Tension crack in hillslope face

The following assumptions are made in this analysis:

- 1) Both sliding surface and tension crack strike parallel to hillslope surface.
- 2) The failure plane must daylight in the slope face, i.e. $\beta > \alpha$.
- 3) The failure plane dip must be greater than the friction angle, i.e. $\alpha > \phi$.
- 4) The tension crack is vertical and may be filled with water to a maximum depth of z_w .

5) **Atmospheric** equilibrium occurs where the failure surface daylights on the **hillslope** face and at the top of the water column in the tension crack.

6) The weight of the sliding block, W , the uplift force due to positive pore pressure, U , and the force due to water pressure in the tension crack, V , all act on the centroid of the sliding mass. Failure is by sliding, translational movement only.

7) The shear strength of the sliding surface is defined by cohesion, c , and friction angle, ϕ , which are related by $S = c + \sigma \tan \phi$.

8) The model considers a slice of unit width and it is assumed that there is no resistance to sliding at the lateral boundaries of the failure block.

The factor of safety, F , is then:

$$F = \frac{cA + (W \cos \alpha - U - V \sin \alpha) \tan \phi}{W \sin \alpha + V \cos \alpha} \quad (\text{C-1})$$

where from Figure 24, the strip of unit width over which cohesion acts:

$$A = (H - Z) \text{cosec} \alpha \quad (\text{C-2})$$

the uplift force due to water pressure on sliding surface:

$$U = \frac{1}{2} \gamma_w Z_w (H - Z) \operatorname{cosec} \alpha \quad (\text{C-3})$$

and the cleft pressure, uplift force due to water pressure in tension crack:

$$V = \frac{1}{2} \gamma_w Z_w^2 \quad (\text{C-4})$$

For the tension crack in the upper slope surface the weight of the sliding block is,

$$W = \frac{1}{2} \gamma H^2 \left\{ \left[1 - \left(\frac{Z}{H} \right)^2 \right] \cot \alpha - \cot \beta \right\} \quad (\text{C-5})$$

and for the tension crack in the slope face the weight of the sliding block is,

$$W = \frac{1}{2} \gamma H^2 \left[\left(1 - \frac{Z}{H} \right)^2 \cot \alpha (\cot \alpha \tan \beta - 1) \right] \quad (\text{C-6})$$

In order to simplify calculations, equation C-1 can be expressed in a dimensionless form,

$$F = \frac{\left(\frac{2c}{\gamma H} \right) P + [Q \cot \alpha - R(P + S)] \tan \phi}{Q + RS \cot \alpha} \quad (\text{C-7})$$

where $P = \left(1 - \frac{Z}{H} \right) \operatorname{cosec} \alpha \quad (\text{C-8})$

For a tension crack in the upper slope surface:

$$Q = \left\{ \left[1 - \left(\frac{Z}{H} \right)^2 \right] \cot \alpha - \cot \beta \right\} \sin \alpha \quad (\text{K-9})$$

$$R = \frac{\gamma_w}{\gamma} \frac{Z_w}{Z} \frac{Z}{H} \quad (\text{C-10})$$

$$S = \frac{Z_w}{Z} \frac{Z}{H} \sin \alpha \quad (\text{C-11})$$

$$\frac{Z}{H} = 1 - \sqrt{\cot \beta \tan \alpha} \quad (\text{C-12})$$

For a tension crack is in the **slope face**:

$$Q = \left(1 - \frac{Z}{H}\right)^2 \cos \alpha (\cot \alpha \tan \beta - 1) \quad (\text{C-13})$$

$$R = \frac{\gamma_w}{\gamma} \frac{Z_w}{Z} \frac{Z}{H} \quad (\text{C-14})$$

$$S = \frac{Z_w}{Z} \frac{Z}{H} \sin \alpha \quad (\text{C-15})$$

$$\frac{Z}{H} = (1 - \cot \beta \tan \alpha) \quad (\text{C-16})$$

APPENDIX D. MODIFIED CULMANN MODEL INCLUDING HORIZONTAL SEISMIC ACCELERATIONS

The following derivations are used in a modified **Culmann** analysis that includes horizontal seismic accelerations. The force on the failure block resulting from earthquake accelerations is considered as an equivalent static force with magnitude F_e , equal to the product of the seismic coefficient, K , and the weight of the sliding mass due to the gravitational acceleration of the failure block, W . So, $F_e = KW$ where K is expressed as a fraction of the normal gravitational acceleration due to a seismic force, g (e.g., $Kg=0.2g$). Figure 5-1 depicts the gravitational (W), earthquake (F_e), and resultant (F_r) forces acting on the center of mass of the failure block.

The shear force on a failure plane due to the weight of the failure block and force resulting from seismic acceleration is given by:

$$\tau = W \sin \alpha + KW \cos \alpha$$

$$\tau = W(\sin \alpha + K \cos \alpha) \quad (D-1)$$

Shear strength, S , along a failure plane is composed of the cohesion component, cA , plus the difference between the frictional components where $W \cos \alpha$ is the normal force, $KW \sin \alpha$ is the upward directed force resulting from seismic accelerations, c is cohesion, and A is the area of a strip of unit width on the failure plane.

So,

$$S = cA + (W \cos \alpha - KW \sin \alpha) \tan \phi$$

$$S = cA + W(\cos \alpha - K \sin \alpha) \tan \phi \quad (D-2)$$

At limiting equilibrium the shear force equals the shear strength,

$$\tau = S = W(\sin \alpha + K \cos \alpha) = cA + W(\cos \alpha - K \sin \alpha) \tan \phi$$

or,

$$W[(\sin \alpha + K \cos \alpha) - (\cos \alpha - K \sin \alpha) \tan \phi] = cA \quad (D-3)$$

From equation B-S the weight of the block is,
$$W = \frac{1}{2} \left(\frac{H \sin(\beta - \alpha) A \gamma}{\sin \beta} \right)$$

Substituting into D-3,

$$cA = \frac{1}{2} \left(\frac{H \sin(\beta - \alpha) A \gamma}{\sin \beta} \right) [(\sin \alpha + K \cos \alpha) - (\cos \alpha - K \sin \alpha) \tan \phi]$$

Solving for the critical height H_c ,

$$H_c = \frac{2c}{\gamma} \frac{\sin \beta}{\sin(\beta - \alpha) [(\sin \alpha + K \cos \alpha) - (\cos \alpha - K \sin \alpha) \tan \phi]} \quad (D-4)$$

For simplicity, assume that the inclination of the failure plane remains the same for seismic and aseismic conditions. Therefore, equation B-7, $\alpha = \frac{1}{2}(\beta + \phi)$ is still used.

Substituting equation B-7 into D-4,

$$H_c = \frac{2c}{\gamma} \frac{\sin \beta}{\sin\left(\frac{\beta - \phi}{2}\right) \left[\left(\sin\left(\frac{\beta + \phi}{2}\right) + K \cos\left(\frac{\beta + \phi}{2}\right) \right) - \left(\cos\left(\frac{\beta + \phi}{2}\right) - K \sin\left(\frac{\beta + \phi}{2}\right) \right) \tan \phi \right]}$$

and $\tan \frac{\sin \phi}{\cos \phi}$

$$H_c = \frac{2c}{\gamma} \frac{\sin \beta \cos \phi}{\sin\left(\frac{\beta - \phi}{2}\right) \left[\left(\sin\left(\frac{\beta + \phi}{2}\right) + K \cos\left(\frac{\beta + \phi}{2}\right) \right) \cos \phi - \left(\cos\left(\frac{\beta + \phi}{2}\right) - K \sin\left(\frac{\beta + \phi}{2}\right) \right) \sin \phi \right]}$$

$$H_c = \frac{2c}{\gamma} \frac{\sin \beta \cos \phi}{\sin\left(\frac{\beta - \phi}{2}\right) \left[\sin\left(\frac{\beta + \phi}{2}\right) \cos \phi + K \cos\left(\frac{\beta + \phi}{2}\right) \cos \phi - \cos\left(\frac{\beta + \phi}{2}\right) \sin \phi - K \sin\left(\frac{\beta + \phi}{2}\right) \sin \phi \right]}$$

Using the trigonometric identities, $\sin(u - v) = \sin u \cos v - \cos u \sin v$

$$\cos(u - v) = \cos u \cos v + \sin u \sin v$$

where $u = \frac{\beta + \phi}{2}$ and $v = \phi$

$$H_c = \frac{2c}{\gamma} \frac{\sin \beta \cos \phi}{\sin\left(\frac{\beta - \phi}{2}\right) \left[\sin\left(\frac{\beta + \phi}{2} - \phi\right) + K \sin\left(\frac{\beta + \phi}{2} - \phi\right) \right]}$$

$$H_c = \frac{2c}{\gamma} \frac{\sin \beta \cos \phi}{\sin^2\left(\frac{\beta - \phi}{2}\right) + K \cos\left(\frac{\beta - \phi}{2}\right) \sin\left(\frac{\beta - \phi}{2}\right)}$$

where $2 \sin^2\left(\frac{\beta - \phi}{2}\right) = 1 - \cos 2\left(\frac{\beta - \phi}{2}\right)$

$$\text{so, } H_c = \frac{4c}{\gamma} \frac{\sin \beta \cos \phi}{1 - \cos(\beta - \phi) + \frac{1}{2} K \sin(\beta - \phi)} \quad (\text{D-5})$$

However, equation D-5 was derived assuming that the failure plane initiating under seismic conditions will form at the same angle as under aseismic conditions. The following derivation reveals that equation B-7, $\alpha = \frac{1}{2}(\beta + \phi)$, does not apply to seismic conditions.

Instead of substituting equation B-7 into D-4, maximize the function $\frac{dc_d}{d\alpha}$

Since

$$H_c = \frac{2c}{\gamma} \frac{\sin \beta}{\sin(\beta - \alpha) [(\sin \alpha + K \cos \alpha) - (\cos \alpha - K \sin \alpha) \tan \phi]}$$

Let $u = \frac{1}{2} \frac{H\gamma}{\sin 4}$

Solving for c_d ,

$$c_d = u \sin(\beta - \alpha) [(\sin \alpha + K \cos \alpha) - (\cos \alpha - K \sin \alpha) \tan \phi]$$

Expand, where $\sin(\beta - \alpha) = \sin \beta \cos \alpha - \cos \beta \sin \alpha$

$$\frac{dc_d}{d\alpha} = \frac{d}{d\alpha} [u(\sin \beta \cos \alpha - \cos \beta \sin \alpha)(\sin \alpha + K \cos \alpha - \cos \alpha \tan \phi) + K \sin \alpha \tan \phi]$$

$$\frac{dc_d}{d\alpha} = \frac{d}{d\alpha} u(\sin \beta \cos \alpha \sin \alpha + K \sin \beta \cos^2 \alpha - \sin \beta \cos^2 \alpha \tan \phi + K \sin \beta \cos \alpha \sin \alpha \tan \phi - \cos \beta \sin^2 \alpha - K \cos \beta \sin \alpha \cos \alpha + \cos \beta \sin \alpha \cos \alpha \tan \phi - K \cos \beta \sin^2 \alpha \tan \phi)$$

Differentiate,

$$\begin{aligned} \frac{dc_d}{d\alpha} = u & [\sin \beta \cos^2 \alpha - \sin \beta \sin^2 \alpha - 2K \sin \beta \cos \alpha \sin \alpha + \sin \beta \tan \phi 2 \cos \alpha \sin \alpha \\ & + K(\sin \beta \cos^2 \alpha \tan \phi - \sin \beta \sin^2 \alpha \tan \phi) - \cos \beta 2 \sin \alpha \cos \alpha - K(\cos \beta \cos^2 \alpha - \cos \beta \sin^2 \alpha) \\ & + \cos \beta \tan \phi \cos^2 \alpha - \cos \beta \tan \phi \sin^2 \alpha - K \cos \beta 2 \sin \alpha \cos \alpha \tan \phi] \end{aligned}$$

Set $\frac{dc_d}{d\alpha} = 0$

where $\sin 2\alpha = 2 \sin \alpha \cos \alpha$ and $\cos 2\alpha = \cos^2 \alpha - \sin^2 \alpha$

$$\begin{aligned} \text{SO, } 0 = & \cos 2\alpha(\sin \beta + \cos \beta \tan \phi) + \sin 2\alpha(\sin \beta \tan \phi - \cos \beta) \\ & + K[\cos 2\alpha(\sin \beta \tan \phi - \cos \beta) - \sin 2\alpha(\sin \beta + \cos \beta \tan \phi)] \end{aligned}$$

Now,

$$\begin{aligned} & \cos 2\alpha[(\sin \beta + \cos \beta \tan \phi) + K(\sin \beta \tan \phi - \cos \beta)] \\ & = \sin 2\alpha[K(\sin \beta + \cos \beta \tan \phi) - (\sin \beta \tan \phi - \cos \beta)] \end{aligned}$$

$$\frac{\sin 2\alpha}{\cos 2\alpha} = \frac{(\sin \beta + \cos \beta \tan \phi) + K(\sin \beta \tan \phi - \cos \beta)}{K(\sin \beta + \cos \beta \tan \phi) + (\cos \beta - \sin \beta \tan \phi)}$$

Multiply right hand side by $\frac{1}{\cos \beta} / \frac{1}{\cos \beta}$

$$\tan 2\alpha = \frac{\tan \beta + \tan \phi + K(\tan \beta \tan \phi - 1)}{1 - \tan \beta \tan \phi + K(\tan \beta + \tan \phi)}$$

where by trigonometric identities $\tan(\beta + \phi) = \frac{\tan \beta + \tan \phi}{1 - \tan \beta \tan \phi}$

So, the inclination of the failure plane that maximizes cohesion under the conditions of an equivalent static horizontal seismic force is:

$$\alpha = \frac{1}{2} \tan^{-1} \left[\frac{\tan \beta + \tan \phi + K(\tan \beta \tan \phi - 1)}{1 - \tan \beta \tan \phi + K(\tan \beta + \tan \phi)} \right] \quad (\text{D-6})$$

A comparison of equations B-7 and D-6 reveals that the inclination of the failure surface, α , will have a shallower angle under horizontal seismic accelerations given otherwise equal conditions. For example, if $\beta = 60^\circ$, $\phi = 30^\circ$, and $K = 0.2$ equation B-7 produces a failure plane inclined at $\alpha = 45^\circ$. In contrast, equation D-6 predicts a failure plane inclined at $\alpha = 41^\circ$. Therefore, with a seismic acceleration of two-tenths of gravity oriented horizontally, equation D-6 results in a failure plane with approximately a 10% shallower gradient.

Substitution of equation D-6 into D-4 results in an unwieldy expression that is not shown here. Nonetheless, the influence of a seismic force out of the slope serves to increase the magnitude of the denominator in equation D-4, decreasing the relative critical height attainable.

APPENDIX E. MODIFIED CULMANN MODEL INCLUDING VERTICAL SEISMIC ACCELERATIONS

The following derivations are used in a modified **Culmann** analysis that includes vertical seismic accelerations. The force on the failure block resulting from earthquake accelerations is considered as an equivalent static force with magnitude F_e , equal to the product of the seismic coefficient, K , and the weight of the sliding mass due to the gravitational acceleration of the failure block, W . So, $F_e = KW$ where K is expressed as a fraction of the normal gravitational acceleration due to a seismic force, g (e.g., $Kg=0.2g$). Figure 5-3 depicts the gravitational (W), earthquake (F_e), and resultant (Fr) forces acting on the center of mass of the failure block for a vertically upward oriented earthquake force. The force balance for a vertically downward oriented earthquake force is depicted in Figure 5-2.

The shear force on a failure plane due to the weight of the failure block and force resulting from a vertically upward oriented seismic acceleration:

$$\tau = W \sin \alpha - KW \sin \alpha \quad (E-1)$$

So,
$$\tau = W \sin \alpha (1 - K)$$

The shear strength is
$$S = cA + (W \cos \alpha - KW \cos \alpha) \tan \phi \quad (E-2)$$

$$S = cA + W \cos \alpha (1 - K) \tan \phi$$

At limiting equilibrium the shear force equals the shear strength,

$$\tau = S = W \sin \alpha (1 - K) = cA + W \cos \alpha (1 - K) \tan \phi$$

or,
$$W(\sin \alpha (1 - K) - \cos \alpha (1 - K) \tan \phi) = cA \quad (E-3)$$

From equation B-5 the weight of the block is,
$$W = \frac{1}{2} \left(\frac{H \sin(\beta - \alpha) A \gamma}{\sin \theta} \right)$$

Substituting into E-3,

$$cA = \frac{1}{2} \left(\frac{H \sin(\beta - \alpha) A \gamma}{\sin \beta} \right) [\sin \alpha (1 - K) - \cos \alpha (1 - K) \tan \phi]$$

Solving for the critical height H_c ,

$$H_c = \frac{2c}{\gamma} \frac{\sin \beta}{\sin(\beta - \alpha) [\sin \alpha (1 - K) - \cos \alpha (1 - K) \tan \phi]} \quad (\text{E-4})$$

Now, determine the angle of the failure plane that maximizes the function $\frac{dc_d}{d\alpha}$ under an equivalent static force oriented vertically upward.

Let
$$u = \frac{1}{2} \frac{H\gamma}{\sin \beta}$$

Solving for c_d .

$$c_d = u \sin(\beta - \alpha) [\sin \alpha (1 - K) - \cos \alpha (1 - K) \tan \phi]$$

Expand, where
$$\sin(\beta - \alpha) = \sin \beta \cos \alpha - \cos \beta \sin \alpha$$

$$\frac{dc_d}{d\alpha} = \frac{d}{d\alpha} \left[u (\sin \beta \cos \alpha - \cos \beta \sin \alpha) (\sin \alpha (1 - K) - \cos \alpha (1 - K) \tan \phi) \right]$$

$$\frac{dc_d}{d\alpha} = \frac{d}{d\alpha} u \left[\sin \beta \cos \alpha \sin \alpha (1 - K) - \sin \beta \cos^2 \alpha (1 - K) \tan \phi - \cos \beta \sin^2 \alpha (1 - K) + \cos \beta \sin \alpha \cos \alpha (1 - K) \tan \phi \right]$$

Differentiate.

$$\frac{dc_d}{d\alpha} = u(1 - K) (\sin \beta \cos^2 \alpha - \sin \beta \sin^2 \alpha + 2 \sin \beta \cos \alpha \sin \alpha \tan \phi - 2 \cos \beta \sin \alpha \cos \alpha + \cos \beta \cos^2 \alpha \tan \phi - \cos \beta \sin^2 \alpha \tan \phi)$$

$$\frac{dc_d}{d\alpha} = u(1 - K) \left[(\sin \beta + \cos \beta \tan \phi) (\cos^2 \alpha - \sin^2 \alpha) + 2 \cos \alpha \sin \alpha (\sin \beta \tan \phi - \cos \beta) \right]$$

Set
$$\frac{dc_d}{d\alpha} = 0$$

where $\sin 2\alpha = 2 \sin \alpha \cos \alpha$ and $\cos 2\alpha = \cos^2 \alpha - \sin^2 \alpha$

So, $0 = \cos 2\alpha(\sin \beta + \cos \beta \tan \phi) + \sin 2\alpha(\sin \beta \tan \phi - \cos \beta)$

Note, the term with the seismic coefficient, K , has dropped out. Therefore, the derivation is the same as Appendix B for equation B-7. The inclination of the failure plane which maximizes cohesion under the seismic conditions of a vertically oriented equivalent static force is the same as an **aseismic** condition:

$$\alpha = \frac{1}{2}(\beta + \phi) \quad (\text{E-5})$$

An expression for the critical height is determined by substituting E-5 into E-4,

$$H_c = \frac{2c}{\gamma} \frac{\sin \beta}{\sin\left(\beta - \frac{\beta + \phi}{2}\right) \left[\sin\left(\frac{\beta + \phi}{2}\right)(1 - K) - \cos\left(\frac{\beta + \phi}{2}\right)(1 - K) \tan \phi \right]}$$

$$H_c = \frac{2c}{\gamma} \frac{\sin \beta \cos \phi}{\sin\left(\frac{\beta - \phi}{2}\right) \left[\sin\left(\frac{\beta + \phi}{2}\right)(1 - K) \cos \phi - \cos\left(\frac{\beta + \phi}{2}\right)(1 - K) \sin \phi \right]}$$

where $\sin\left[\left(\frac{\beta - \phi}{2}\right) - \phi\right] = \sin\left(\frac{\beta - \phi}{2}\right) \cos \phi - \cos\left(\frac{\beta - \phi}{2}\right) \sin \phi$

$$H_c = \frac{2c}{\gamma} \frac{\sin \beta \cos \phi}{\sin^2\left(\frac{\beta - \phi}{2}\right)(1 - K)} \quad \text{a n d} \quad 2 \sin^2\left(\frac{\beta - \phi}{2}\right) = 1 - \cos 2\left(\frac{\beta - \phi}{2}\right)$$

So,
$$H_c = \frac{4c}{\gamma} \frac{\sin \beta \cos \phi}{[1 - \cos(\beta - \phi)](1 - K)} \quad (\text{E-6})$$

Equation E-6 reveals that a seismic body force oriented vertically upward reduces the influence of gravity and actually increases the relative stability of a slope

In contrast, a vertically downward oriented earthquake force serves to decrease **hillslope** stability. The shear force on a **failure** plane due to the weight of the failure block and force resulting from a vertically downward oriented seismic acceleration:

$$\tau = W \sin \alpha + KW \sin \alpha \quad (\text{E-7})$$

So,
$$\tau = W \sin \alpha(1 + K)$$

The shear strength is
$$S = cA + (W \cos \alpha + KW \cos \alpha) \tan \phi \quad (\text{E-8})$$

$$S = cA + W \cos \alpha(1 + K) \tan \phi$$

Subsequent manipulation is omitted because it is identical to the previous case of a vertically upward oriented earthquake force. Thus; the critical height in terms of material properties, hillslope angle, and the failure plane angle is:

$$H_c = \frac{2c}{\gamma} \frac{\sin \beta}{\sin(\beta - \alpha) [\sin \alpha(1 + K) - \cos \alpha(1 + K) \tan \phi]} \quad (\text{E-9})$$

and the critical height in terms of material properties and **hillslope** angle:

$$H_c = \frac{4c}{\gamma} \frac{\sin \beta \cos \phi}{[1 - \cos(\beta - \phi)](1 + K)} \quad (\text{E-10})$$

So, while vertically upward earthquake forces serve to increase the critical height of hillslopes, vertically downward oriented earthquake forces decrease the critical height.